Title
Lensfree Fluorescent Computational Microscopy on a Chip

Author
Coskun, Ahmet Faruk

Publication Date
2013

Peer reviewed|Thesis/dissertation

UNIVERSITY OF CALIFORNIA

Los Angeles

Lensfree Fluorescent Computational Microscopy on a Chip

A dissertation submitted in partial satisfaction of the

requirements for the degree Doctor of Philosophy

in Electrical Engineering

by

Ahmet Faruk Coskun

2013

ABSTRACT OF THE DISSERTATION

Lensfree Fluorescent Computational Microscopy on a Chip

by

Ahmet Faruk Coskun

Doctor of Philosophy in Electrical Engineering

University of California, Los Angeles, 2013

Professor Aydogan Ozcan, Chair

Optical Microscopy has become an indispensible tool for many scientific disciplines especially in biomedical sciences. Although rapid advancements in modern microscopy techniques allow us to visualize the microscopic structures and processes in unprecedented details, they are still relatively bulky and low-throughput, necessitating a tedious mechanical scanning to image large-area micro-systems. In this dissertation, I demonstrate an on-chip computational microscopy platform as an alternative high-throughput screening tool that can rapidly monitor fluorescently labeled cells or small animal models over an ultra-wide field-of-view (FOV) of e.g., >9-18 cm^2 without the use of any lenses, thin-film filters or mechanical scanners. In this technique, fluorescent excitation is achieved through a prism or hemispherical-glass interface illuminated by an incoherent source such as a light emitting diode (LED). After interacting with the entire object volume, this excitation light is rejected by total-internal-reflection (TIR) process that is occurring at the bottom of the sample micro-fluidic chip. The fluorescent emission from the

excited objects, which does not entirely obey TIR, is then collected by a planar or tapered fiber-optic faceplate and is delivered to an optoelectronic sensor array such as a charge-coupled-device (CCD). By using a compressive sensing/sampling based decoding algorithm, the acquired lensfree raw fluorescent images of the sample can then be rapidly processed to yield e.g., <3-4μm spatial resolution over the entire FOV. Moreover, vertically stacked micro-channels that are separated by e.g., 50-100 μm can also be successfully imaged using the same lensfree on-chip microscopy platform, further increasing the overall throughput of this modality. Such a computational fluorescent microscopy technique, with a rapid compressive decoder behind it, could pave the way toward rapid diagnostic systems for biomedical applications, including on-chip cytometry, rare-cell analysis, as well as small animal research.

The dissertation of Ahmet Faruk Coskun is approved.

Dino Di Carlo

Benjamin Williams

Bahram Jalali

Oscar M. Stafsudd

Aydogan Ozcan, Committee Chair

University of California, Los Angeles

2013

Table of Contents

Acknowledgements

First and foremost, I would like to thank my advisor, Dr. Aydogan Ozcan, for his continuous support throughout my research. He has been a great mentor and I am deeply grateful to him for his role in my education. I appreciate the opportunity that he gave me to pursue my academic interest. In addition, I would like to thank my doctoral committee members, Dr. Dino Di Carlo, Dr. Benjamin Williams, Dr. Bahram Jalali, and Dr. Oscar Stafsudd for their support.

I had the opportunity to work with outstanding colleagues in the lab. I am especially thankful to Hongying Zhu, Euan McLeod, Sungkyu Seo, Derek Tseng, Onur Mudanyali, Serhan O. Isikman, Justin Su, Bahar Khademhosseini, Ikbal Sencan, Isa Navruz, Waheb Bishara, Gabriel Biener, Myungjun Lee, Alon Greenbaum, Wei Luo, Zoltan Gorocs, Sam Mavandadi, Justin Wong, Caglar Arpali, Serap A. Arpali, Liang Xue, Uzair Sikora, Oguzhan Yaglidere, Qingshan Wei, Ertan Salik, Delaram Khodadadi, Richie Nagi and all that I forgot to mention, thank you for your great friendship in the lab.

Interdisciplinary research can never be succeeded alone. I collaborated with remarkable scientists throughout the world. I would like to express my gratitude to Dr. Dino Di Carlo and his lab members Danny R. Gossett, Westbrook Weaver, Albert J. Mach, Patrick Sandoz, Dr. Hatice Altug and her lab member Arif E. Cetin, and Dr. Keisuke Goda.

Overall, I would like to express my sincere thanks and appreciation to the special people that helped me in my Ph.D. journey as well as in my whole past life, without whom I can never have my completion today.

Thank you all!

Vita

2003-2008	Bachelor of Science in Electrical Engineering (Major)
	Koc University, Istanbul, Turkey
2003-2008	Bachelor of Science in Physics (Major)
	Koc University, Istanbul, Turkey
2008-2009	Master of Science in Electrical Engineering (Major)
	University of California, Los Angeles, U.S.
2008-2009	Master of Science in Chemistry and Biochemistry (Minor)
	University of California, Los Angeles, U.S.

Publications

Ahmet F. Coskun, Ting-Wei Su and Aydogan Ozcan, "Wide field-of-view lens-free fluorescent imaging on a chip," Lab on a Chip, 10, 824 (2010)

Bahar Khademhosseini, Ikbal Sencan, Gabriel Biener, Ting-Wei Su, Ahmet F. Coskun, Derek Tseng, and Aydogan Ozcan, "Lensfree On- chip Imaging using Nano-structured Surfaces," Applied Physics Letters, 96, 171106 (2010)

Ahmet F. Coskun, Ikbal Sencan, Ting-Wei Su, and Aydogan Ozcan, "Lensless wide-field fluorescent imaging on a chip using compressive decoding of sparse objects," Opt. Express, 18, 10510-10523 (2010)

Waheb Bishara, Ting-Wei Su, Ahmet F. Coskun, and Aydogan Ozcan, "Lensfree on-chip microscopy over a wide field-of-view using pixel super-resolution," Opt. Express, 18, 11181-11191 (2010)

Ahmet F. Coskun, Ting-Wei Su, Ikbal Sencan, and Aydogan Ozcan, "Lensfree Fluorescent On-Chip Imaging Using Compressive Sampling," Optics & Photonics News, 21(12), 27-27 (2010)

Bahar Khademhosseini, Gabriel Biener, Ikbal Sencan, Ting-Wei Su, Ahmet F. Coskun, and A. Ozcan, "Lensfree Sensing on a Micro-fluidic Chip using Plasmonic Nano-apertures," Appl. Phys. Lett., 97, 221107 (2010)

Ahmet F. Coskun, Ikbal Sencan, Ting-Wei Su, and Aydogan Ozcan, "Lensfree Fluorescent On-Chip Imaging of Transgenic Caenorhabditis elegans Over an Ultra-Wide Field-of-View," PLoS ONE 6, e15955 (2011)

Ahmet F. Coskun, Ikbal Sencan, Ting-Wei Su, and Aydogan Ozcan, "Wide-field Lensless Fluorescent Microscopy Using a Tapered Fiber-optic Faceplate On a Chip," Analyst, 136, 3512-3518 (2011)

Hongying Zhu, Sam Mavandadi, Ahmet F. Coskun, Oguzhan Yaglidere, and Aydogan Ozcan, "Optofluidic Fluorescent Imaging Cytometry on a Cellphone," Analytical Chemistry, 83, 17, 6641–6647 (2011)

Ahmet F. Coskun, Ting-Wei Su, Ikbal Sencan, and Aydogan Ozcan, "Lensless Fluorescent Microscopy On a Chip," Journal of Visualized Experiments, 54, e3181 (2011)

Alon Greenbaum, Wei Luo, Ting-Wei Su, Zoltán Göröcs, Liang Xue, Serhan O Isikman, Ahmet F Coskun, Onur Mudanyali, and Aydogan Ozcan, "Imaging without lenses: achievements and remaining challenges of wide- field on-chip microscopy," Nature Methods, 9, 889–895 (2012)

Serhan O. Isikman, Alon Greenbaum, Wei Luo, Ahmet F. Coskun, and Aydogan Ozcan, "Giga-Pixel Lensfree Holographic Microscopy and Tomography Using Color Image Sensors," PLoS ONE, 7,9, e45044 (2012)

Serap Altay Arpali , Caglar Arpali , Ahmet F. Coskun , Hsin-Hao Chiang, and Aydogan Ozcan, "High- throughput screening of large volumes of scattering media using structured illumination and fluorescent on-chip imaging," Lab on a Chip, 12, 4968-4971 (2012)

Onur Mudanyanli, Euan McLeod, Wei Luo, Alon Greenbaum, Ahmet F. Coskun, Yves Hennequin, Cedric Allier, and Aydogan Ozcan, "Wide-field optical detection of nano-particles using on-chip microscopy and self-assembled nano-lenses," Nature Photonics, 7, 247-254 (2013)

Ahmet F. Coskun, Justin Wong, Delaram Khodadadi, Richie Nagi, Andrew Tey, and Aydogan Ozcan, "A personalized food allergen testing platform on a cellphone," Lab on a Chip, 13, 636-640 (2013)

Alon Greenbaum, Wei Luo, B. Khademhosseini,Ting-Wei Su, Ahmet F. Coskun, and Aydogan Ozcan, "Increased space-bandwidth product in pixel super-resolved lensfree on-chip microscopy," Scientific Reports, 3, 1717 (2013)

Ahmet F. Coskun, Ting-Wei Su, Ikbal Sencan, and Aydogan Ozcan, "Lensless Fluorescent Imaging On a Chip: A new Method Toward High-throughput Screening of Rare Cells," Editors: Keith E. Herold & Avi Rasooly, Book Chapter in Biosensors and Molecular Technologies for Cancer Diagnostics, CRC Press (2012)

Chapter 1 Introduction

Optical imaging has become a powerful tool for biomedical research as well as clinical diagnostics. One of the most important features of optical imaging methods is that they can, in general, provide a decent spatial resolution without exposing the specimen to high-energy radiation. While such useful resolution is limited to small depths within the specimen (typically a few hundreds of microns), optical imaging methods are still widely used in biomedicine as they can also provide molecular specificity based on, e.g., absorption, fluorescence, or scattering processes. Among these contrast mechanisms, fluorescence deserves a special attention since it has been widely utilized not only for microscopy but also for various high-throughput screening applications including antibody microarrays[1] and biochemical assays[2], bringing specificity and sensitivity to the imaging platform within reasonable cost and ease of use.[3,4] In particular, fluorescent-based high-throughput separation and sorting of heterogeneous samples into purified cell populations has been quite valuable to study eukaryotic cells for enhancing the understanding of diseases and cell-based therapies[5].

Along the same lines, an important high-throughput problem of significant interest is rapid detection and quantification of rare cell populations (e.g., circulating tumor cells—CTCs) within large sample volumes.[6] What makes this problem rather challenging is that these CTCs (that are detached from a primary tumor site) circulate within the bloodstream at extremely low densities, i.e., only a few cells per mL of whole blood, which implies less than one cell among, e.g., billion cells.[7] Recently, microfluidics-based lab-on-a-chip technologies have been utilized to efficiently and specifically capture CTCs from whole blood samples.[8–11] To increase the sensitivity of cell isolation, surface chemistry–based large-area microfluidic chips were used such that CTCs were

specifically captured over an active area of ~9cm^2.[10] While such microfluidic technologies offer powerful solutions for isolation and capture of CTCs at extremely low densities, the second challenge, namely, rapid quantification of these captured cells, still remains. The main reason is that conventional fluorescent microscopes that are used to analyze these large-area microfluidic devices do "not" provide sufficient throughput to rapidly image such large field-of-views (FOVs). Typical imaging FOV of a conventional microscope covers a few mm^2, which demands mechanical scanning and the capture of literally thousands of images that should be digitally stitched together to enumerate the captured CTCs. This is not only a slow process, taking hours, but also requires sophisticated and expensive optical hardware that needs to be fairly stable during the entire image acquisition. As an alternative solution to this high-throughput problem, a fiber-optic array based scanning cytometry approach has been successfully demonstrated.[7] Besides the above discussed specific need for rare cell analysis, high-throughput fluorescent imaging is also vital for a variety of other applications such as monitoring of protein or DNA micro-arrays[12,13], screening water-borne parasites in drinking water (e.g. Giardia Muris)[14], as well as imaging a large population of small model animals (e.g., Caenorhabditis Elegans)[15].

In this dissertation, I demonstrate an on-chip computational microscopy platform as an alternative high-throughput screening tool that can rapidly monitor fluorescently monitor fluorescent micro-objects and labeled cells over an ultra-wide FOV (e.g., >9 cm^2) without the use of any lenses, thin-film filters, or mechanical scanners.[16–21] In this lensfree on-chip imaging technique, the microfluidic chip of interest is loaded onto an optoelectronic sensor array (e.g., a CCD) where the fluorescent cells are pumped (i.e., excited) from the side using an incoherent light source. After exciting the captured cells within the chip volume, this excitation light is then rejected using total internal reflection (TIR) process occurring at the bottom facet of the micro-

channel. Most of the fluorescent emission from these excited cells, however, does not obey TIR and can be detected by the optoelectronic sensor array within a detection numerical aperture (NA) of ~1. To filter out the weakly scattered excitation light and hence create a better dark-field background, I also employ an inexpensive absorption filter with a thickness of <100 μm. Based on this lensfree detection principle, only the fluorescent emission of the labeled objects located on the chip can be recorded by an optoelectronic sensor array achieving an ultra-wide FOV of, e.g., >9 cm^2. Acquired raw fluorescent images are then decoded based on a compressive sampling algorithm, yielding higher resolution microscopic images. The presented on-chip imaging approach, being a compact fluorescent encoder, together with a compressive decoder behind it, achieves < 3-4 μm spatial resolution with wide-field and multi-layer imaging capabilities on the same platform. This compact on-chip fluorescent imaging platform, with a rapid compressive decoder behind it, could be rather valuable for high-throughput cytometry, rare-cell research and microarray-analysis.

There are several important characteristics of this novel platform that holds the promise for high-throughput screening applications in biomedical sciences: (1) The excitation light source in this fluorescent imaging system does not need to be a laser such that an incoherent source (e.g., a light emitting diode) can be used to deliver the illumination through a fiber optic cable to the prism etc. interface. This approach reduces the complexity of the on-chip imaging setup, making it highly compact and cost-effective. (2) The alignment requirement of a fluorescent microscopy system are also significantly eliminated, since I directly position the fluorescent specimen on a sensor-array without the use of any lenses or bulky components. In other words, I do not need to adjust the focus of this on-chip microscopy system as I keep the imaging distances constant in this platform, which is highly robust and repeatable from one experiment to another. (3) The

time consuming mechanical scanning over the entire fluorescent specimen is also mitigated because I operate this computational imaging platform under unit magnification without the use of any lenses such that it can achieve an imaging FOV (for a single frame image) equal to the spatial extend of a sensor array (e.g. CCD). Compared to the FOV of a conventional >10-20X magnification lens-based fluorescent microscope, this presented lensfree fluorescent microscope can achieve an order of magnitude larger imaging area that can simultaneously be captured. (4) The compressive decoding enabled reconstruction process rapidly provides the final high-resolution images in ~ 10 minutes (i.e., using a GPU) for the entire FOV, which can still be expedited using CUDA processing.[22,23] Quite importantly, the use of measured point-spread-function (PSF) for the reconstruction of lensfree images also removes the potential artifacts due to the detector array design imperfections, providing a sensor-independent reconstruction performance in this on-chip fluorescent imaging platform. (5) The incorporation of this presented on-chip microscopy platform and the recently developed smart microfluidic devices[24,25] is straightforward, enabling highly automated and integrated diagnostic systems that can perform the sample preparation and the imaging on the same platform without the need for an user intervention. (6) Fluorescent micro-objects located at different vertical layers that are separated by ~ 50-100 microns can also be imaged and reconstructed simultaneously, demonstrating the three-dimensional imaging capability of this on-chip microscopy platform. Combined with the emerging field of three-dimensional microfluidics[26,27], the throughput of this on-chip cell screening platform can be increased by a few folds without the use of any other mechanical scanning over the axial direction. (7) This on-chip computational microscopy platform has a scalable performance in terms of FOV, frame rate, sensitivity, and resolution that could get better with the new coming sensor arrays fabricated by the advanced nano-technology tools.

1. De Wildt, R. M., Mundy, C. R., Gorick, B. D. & Tomlinson, I. M. Antibody arrays for high-throughput screening of antibody-antigen interactions. Nat. Biotechnol. **18**, 989–994 (2000).
2. Sundberg, S. A. High-throughput and ultra-high-throughput screening: solution- and cell-based approaches. Curr. Opin. Biotechnol. **11**, 47–53 (2000).
3. Fu, A. Y., Spence, C., Scherer, A., Arnold, F. H. & Quake, S. R. A microfabricated fluorescence-activated cell sorter. Nature Biotechnology **17**, 1109–1111 (1999).
4. Malo, N., Hanley, J. A., Cerquozzi, S., Pelletier, J. & Nadon, R. Statistical practice in high-throughput screening data analysis. Nat. Biotechnol. **24**, 167–175 (2006).
5. Ibrahim, S. F. & Van den Engh, G. High-speed cell sorting: fundamentals and recent advances. Curr. Opin. Biotechnol. **14**, 5–12 (2003).
6. Hu, X. et al. Marker-specific sorting of rare cells using dielectrophoresis. PNAS **102**, 15757–15761 (2005).
7. Krivacic, R. T. et al. A rare-cell detector for cancer. PNAS **101**, 10501–10504 (2004).
8. Adams, A. A. et al. Highly efficient circulating tumor cell isolation from whole blood and label-free enumeration using polymer-based microfluidics with an integrated conductivity sensor. J. Am. Chem. Soc. **130**, 8633–8641 (2008).
9. Gleghorn, J. P. et al. Capture of circulating tumor cells from whole blood of prostate cancer patients using geometrically enhanced differential immunocapture (GEDI) and a prostate-specific antibody. Lab Chip **10**, 27–29 (2010).
10. Nagrath, S. et al. Isolation of rare circulating tumour cells in cancer patients by microchip technology. Nature **450**, 1235–1239 (2007).

11. Wang, S. et al. Three-dimensional nanostructured substrates toward efficient capture of circulating tumor cells. Angew. Chem. Int. Ed. Engl. **48**, 8970–8973 (2009).

12. Kodadek, T. Protein microarrays: prospects and problems. Chemistry & Biology **8**, 105–115 (2001).

13. Heller, M. J. DNA MICROARRAY TECHNOLOGY: Devices, Systems, and Applications. Annual Review of Biomedical Engineering **4**, 129–153 (2002).

14. Ivnitski, D., Abdel-Hamid, I., Atanasov, P. & Wilkins, E. Biosensors for detection of pathogenic bacteria. Biosensors and Bioelectronics **14**, 599–624 (1999).

15. Rohde, C. B., Zeng, F., Gonzalez-Rubio, R., Angel, M. & Yanik, M. F. Microfluidic system for on-chip high-throughput whole-animal sorting and screening at subcellular resolution. PNAS **104**, 13891–13895 (2007).

16. Coskun, A. F., Su, T.-W. & Ozcan, A. Wide field-of-view lens-free fluorescent imaging on a chip. Lab Chip **10**, 824–827 (2010).

17. Coskun, A. F., Sencan, I., Su, T.-W. & Ozcan, A. Lensless wide-field fluorescent imaging on a chip using compressive decoding of sparse objects. Optics Express **18**, 10510 (2010).

18. Coskun, A. F., Su, T., Sencan, I. & Ozcan, A. Lensfree Fluorescent On-Chip Imaging Using Compressive Sampling. Opt. Photon. News **21**, 27–27 (2010).

19. Coskun, A. F., Sencan, I., Su, T.-W. & Ozcan, A. Lensfree Fluorescent On-Chip Imaging of Transgenic Caenorhabditis elegans Over an Ultra-Wide Field-of-View. PLoS ONE **6**, e15955 (2011).

20. Coskun, A. F., Sencan, I., Su, T.-W. & Ozcan, A. Wide-field lensless fluorescent microscopy using a tapered fiber-optic faceplate on a chip. Analyst **136**, 3512–3518 (2011).

21. Coskun, A. F., Su, T.-W., Sencan, I. & Ozcan, A. Lensless Fluorescent Microscopy on a Chip. Journal of Visualized Experiments, **54**, e3181 (2011).

22. Manavski, S. A. & Valle, G. CUDA compatible GPU cards as efficient hardware accelerators for Smith-Waterman sequence alignment. BMC Bioinformatics **9**, S10 (2008).

23. Pham, H. et al. Off-axis quantitative phase imaging processing using CUDA: toward real-time applications. Biomed. Opt. Express **2**, 1781–1793 (2011).

24. Gossett, D. R., Weaver, W. M., Ahmed, N. S. & Carlo, D. D. Sequential Array Cytometry: Multi-Parameter Imaging with a Single Fluorescent Channel. Ann Biomed Eng **39**, 1328–1334 (2011).

25. Mach, A. J., Kim, J. H., Arshi, A., Hur, S. C. & Carlo, D. D. Automated cellular sample preparation using a Centrifuge-on-a-Chip. Lab Chip **11**, 2827–2834 (2011).

26. Anderson, J. R. et al. Fabrication of topologically complex three-dimensional microfluidic systems in PDMS by rapid prototyping. Anal. Chem. **72**, 3158–3164 (2000).

27. Chiu, D. T. et al. Patterned deposition of cells and proteins onto surfaces by using three-dimensional microfluidic systems. PNAS **97**, 2408–2413 (2000).

Chapter 2 Wide field-of-view lensfree fluorescent imaging on a chip

Parts of this chapter have already been published in Lab on a Chip Vol. 10, 824 (2010) and Opt. Photon. News Vol. 21, 27 (2010).

2.1 Introduction

Biomedical imaging tools have found widespread use in medicine and biology. Specifically, fluorescent microscopy[1,2] has lately experienced a fascinating renaissance, expanding our capabilities to probe various biological processes with much better resolution, field-of-view (FOV), speed, signal-to-noise ratio, etc. While these advanced imaging technologies add to our biophotonic toolset, there is still a mismatch in terms of, for example, throughput, compactness and cost-effectiveness between these sophisticated optical platforms and most high-throughput lab-on-a-chip devices. On the other hand, miniaturized and cost-effective formats of microfluidics and lab-on-a-chip analysis have already found several biomedical applications, particularly in point-of-care and field diagnostics.

To provide a better match to this important need, lensfree on-chip imaging is becoming a powerful alternative to conventional techniques.[3] Today's digital sensor arrays have significantly improved space-bandwidth products, dynamic ranges and signal-to-noise ratios. When combined with new image processing algorithms, they provide an opportunity to create imaging modalities that can make up for the lack of complexity of optical components.

In this chapter, I introduce an ultrahigh throughput on-chip fluorescent imaging platform[4] that can simultaneously record the fluorescent images of labeled cells or other micro-objects over an ultra-wide FOV of 2.5 cm x 3.5 cm without the use of any lenses, thin-film filters and

mechanical scanners. The acquired raw lensfree images are then deconvolved to resolve the overlapping fluorescent patterns at the detector plane, improving the throughput of on-chip imaging platform. Such a wide field-of-view lensfree fluorescent imaging modality, when improved with deconvolution algorithms, might be very important for high-throughput screening applications as well as for detection and counting of rare cells within large-area microfluidic devices.

2.2 Materials and methods

Set-up: In this lensfree imaging platform (Fig. 2-1), fluorescent micro-objects (e.g., within a microfluidic chip) are directly positioned onto a CCD or CMOS sensor array with less than ~ 0.5–1.0 mm distance between the sample and sensor planes. To better control this vertical distance in this work, decapped sensors are used such that the protective coverglass of the chip is removed. The fluorescent cells/particles are then pumped at their proper excitation wavelength using e.g., a simple light emitting diode (LED) or a Xenon lamp (tuned to an appropriate spectrum by a monochromator) through the side facet of a rhomboid prism (base: 25 x 35 mm; height: 17 mm, Edmund Optics) as illustrated in Fig. 2-1. Specifically, for the results presented in this chapter, the excitation is achieved using a blue LED (470 nm peak, 30 nm bandwidth, Luxeon Star) pumped through the side facet of the prism (Fig. 2-1). This incoherent excitation beam, after interacting with the sample volume, is reflected through a total internal reflection (TIR) process occurring at the bottom facet of the sample device. The weakly scattered excitation light, which does not obey TIR, is then rejected using a long pass absorption filter (Kodak Wratten Color Filter 12, <30 dB for <500 nm; <0.1 mm thick, Edmund Optics) located on the surface of the charge coupled device (CCD, KAI-11002, Kodak). Only the fluorescent

emission from the excited cells/particles can then be directly detected without the use of any lenses over the entire FOV of the sensor-array (2.5 cm x 3.5 cm).

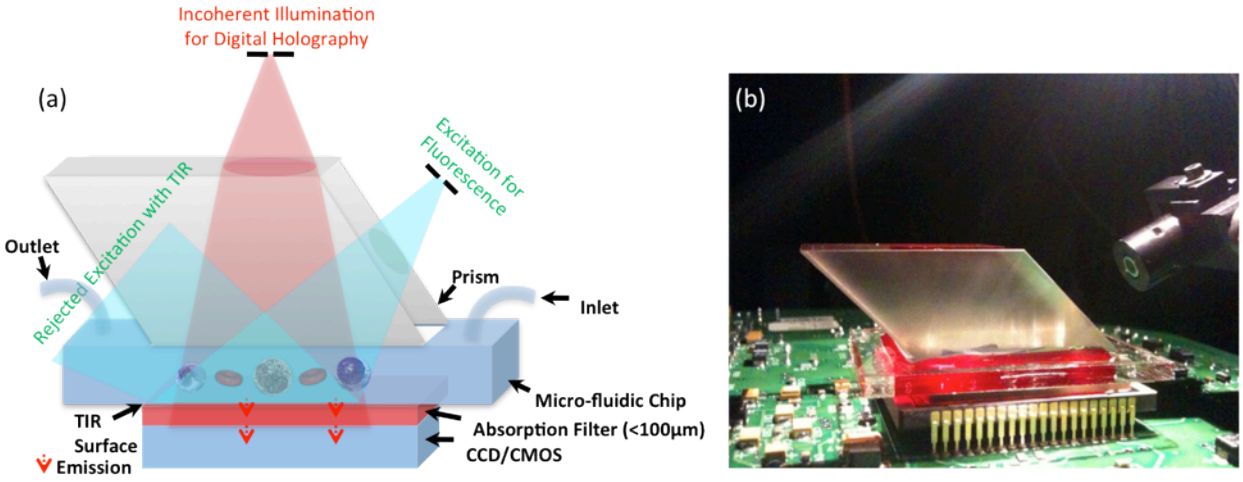

Figure 2-1 | (a) On-chip platform for lensfree fluorescent imaging over a large FOV of 2.5 cm x 3.5 cm. Fluorescent excitation is achieved by using side illumination through a rhomboid prism (conveniently a different prism geometry could also be used). A simple LED or a Xenon lamp tuned by a monochromator is used for excitation. Lens-free holographic imaging of the same FOV is achieved through vertical incoherent illumination (another LED), which uses the flat top part of the prism. Drawing is not to scale. Not shown here, an index matching gel can also be used to avoid TIR and undesired scattering at the bottom facet of the prism. Note also that to better control the vertical distance between the sample micro-channel and the active region of the sensor, we removed the protective coverglass of the chip. The thin absorption filter shown above acts as a protective layer in this case, isolating the active region of the sensor chip from the micro-channels.

The angle of the excitation fiber used in this platform should also be carefully adjusted such that the TIR occurs at the bottom of the glass substrate and air interface. Fig. 2-2 explains the angle conditions that allow various TIR mechanisms for a prism side interface with a right angle of 45°, where the refractive indices of mediums are glass prism (n_1: 1.47), water sample containing fluorescently labeled specimen (n_2: 1.33), and bottom borosilicate glass substrate (n_3: 1.52). Based on Snell's law calculations, Fig. 2-2(a) and (b) demonstrate TIR occurring at the bottom of the prism to water interface which is satisfied for $\theta_2 \geq \theta_{critical,n1\ to\ n2}$ and $45° \geq \theta_1 \geq 33°$; TIR occurring at the bottom of the glass substrate to air interface which is satisfied for $\theta_4 \geq \theta_{critical,n3\ to\ air}$ and $33° \geq \theta_1 \geq 0°$, respectively. As summarized in Fig. 2-3(c), the TIR conditions are

defined based on the normal to the side facet of the prism, where $45° \geq \theta_1 \geq 33°$ ensures the TIR in the prism to water bottom interface and $33° > \theta_1 \geq 0°$ enables the TIR on the bottom of the glass substrate. Therefore, to guarantee the TIR occurring at the interface between the bottom glass substrate and air, one should carefully adjust the angle of a diverging fiber exit (spanning θ_F angles) that should fall within the range of $\theta_A < 33°$ and $\theta_B \geq 0°$.

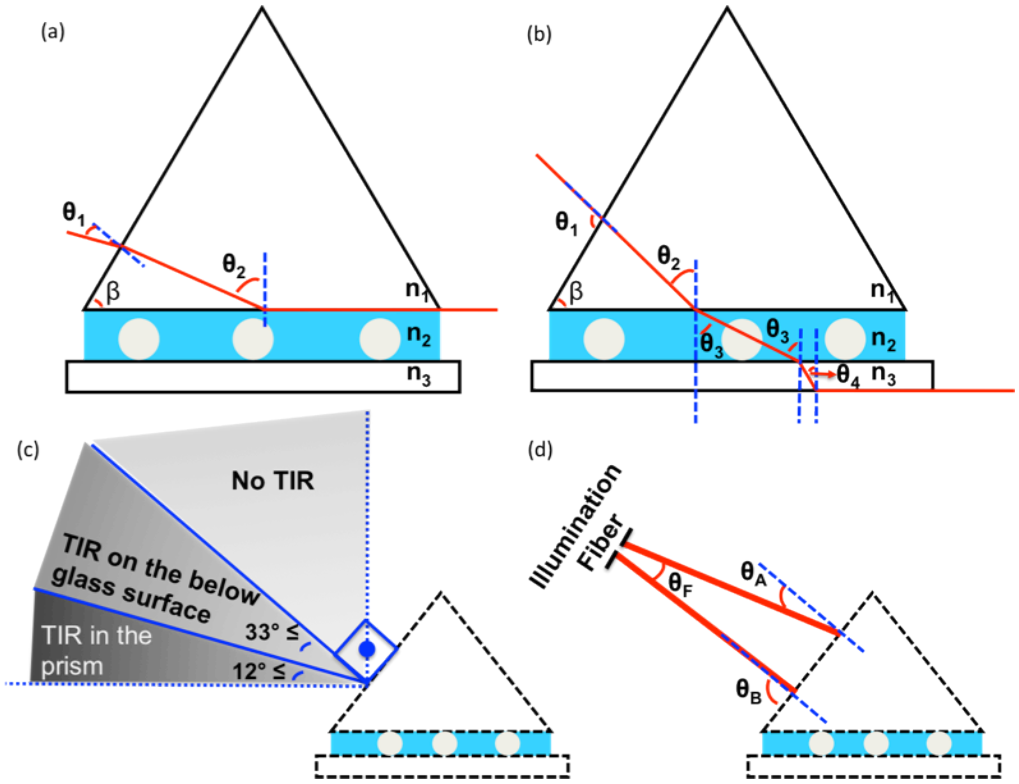

Figure 2-2 | The angle condition analysis to achieve TIR is demonstrated for a prism side interface with β: 45° right angle, where the refractive indices of mediums are glass prism (n_1: 1.47), water sample containing fluorescently labeled specimen (n_2: 1.33), and bottom borosilicate glass substrate (n_3: 1.52). (a) TIR occurring at the bottom of the prism to water interface is satisfied for $\theta_2 \geq \theta_{critical,n1\ to\ n2}$ and $45° \geq \theta_1 \geq 33°$. (b) TIR occurring at the bottom of the glass substrate to air interface is satisfied for $\theta_4 \geq \theta_{critical,n3\ to\ air}$ and $33° \geq \theta_1 \geq 0°$. (c) The TIR conditions are defined based on the normal to the side facet of the prism, where $45° \geq \theta_1 \geq 33°$ ensures the TIR in the prism to water bottom interface and $33° > \theta_1 \geq 0°$ enables the TIR on the bottom of the glass substrate. (d) A diverging fiber exit (spanning θ_F angles) can then be used for excitation within the range of $\theta_A < 33°$ and $\theta_B \geq 0°$.

Deconvolution algorithm: In the configuration of Fig. 2-1, since no lenses are involved in imaging, the fluorescent emission of cells or particles will diverge rapidly, potentially overlapping with each other at the sensor plane. To combat this limitation, the measured

incoherent point-spread function of the fluorescent detection platform is used to deconvolve the acquired lensfree images. In this deconvolution process, the raw lensfree fluorescent image was iteratively refined by an accelerated Lucy–Richardson algorithm.[5–7] By applying Bayes' theorem with the incoherent point-spread function of the on-chip system, the Lucy–Richardson algorithm updated the maximum-likelihood estimation of the fluorescence source distribution in each iteration.[5,6] Prior to this calculation, the incoherent point-spread function of the system is estimated by averaging several measured patterns created by small isolated fluorescent beads. These patterns were aligned with respect to their center of mass coordinates and were individually normalized by their intensities before the averaging process. Since the pixel size of the image sensor is relatively much smaller than the width of the point spread function, the alignment errors due to pixelation or node mislocation within a single pixel can be neglected. Furthermore, since on-chip fluorescent imaging approach does not utilize any lenses, the detection system was spatially invariant which means a single incoherent point spread function can be faithfully used to deconvolve the entire field-of-view.

This iterative deconvolution process was terminated (typically after a hundred cycles) before the emergence of noise amplification to ensure minimal square error between the projected and the measured profiles. The convergence of this algorithm was also accelerated by a vector extrapolation method to shorten the computation time.[7] Coded in MATLAB 2009a, computation of 100 iterations for an image size of 4200 x 2700 pixels with an incoherent point spread function of 70 x 50 pixels takes around 10 min on a dual-core 1.8 GHz Pentium CPU. Since the deconvolution algorithm is highly parallel and iterative, the computation time can be reduced by >40x using a GPU (graphics processing unit – e.g., NVIDIA GeForce GTX 285) with a high performance pipeline structure.[8]

Fluorescent micro-bead sample: The bead containing specimen is prepared by using a micropipette to drop 15–20 μL of this solution on a microscope slide placed under a rhomboid prism for imaging experiments.

White blood cell labeling: First, 2–3 ml of whole blood is mixed with PBS (1:400 ratio) and 20 mm non-fluorescent microspheres (spacer to prevent cell rupture). Then 0.5 ml of 4 mM Calcein AM (excitation 495 nm/emission 515 nm, LIVE Viability Assay, Moleculer Probes) is added to the diluted blood, and incubated at room temperature for <20–30 min. Once green fluorescence in live cells is activated, the white blood cells are ready to be imaged using our on-chip fluorescent imaging platform.

2.3 Results and discussion

To demonstrate the feasibility of this approach, I initially imaged a heterogeneous solution containing 10 μm diameter fluorescent particles (excitation/emission: 495/505 nm), and 20–30 μm diameter non-fluorescent particles as illustrated in Fig. 2-3 and Fig. 2-5. As illustrated in Fig. 2-3, with a vertical distance of ~200 μm between the sample and the sensor planes, the size of each detected spot corresponding to a fluorescent particle was ~200–300 μm, which resulted in significant overlap at the raw lensfree image (see Fig. 2-3(a)). Through digital deconvolution of the raw lensfree fluorescent images, I reconstructed a much higher resolution fluorescent image (Fig. 2-3 (b)), enabling a resolution of ~40–50 μm over the entire sensor FOV i.e., 2.5 cm x 3.5 cm. This ~5 fold spatial resolution improvement resulted in separation of significantly overlapping fluorescent particles from each other as highlighted in Fig. 2-3 (c,d) and 2-3(f,h). For rare cell applications, spatial resolution is less of a concern since the statistical overlap of cells is unlikely. Therefore the limited spatial resolution of the lensfree fluorescent imaging platform should still be sufficient for use in rare cell analysis when combined with microfluidic

chips. The lensfree on-chip operation of this approach also provides compactness that can complement the miniaturized platform of microfluidics, while significantly improving the overall throughput of imaging.

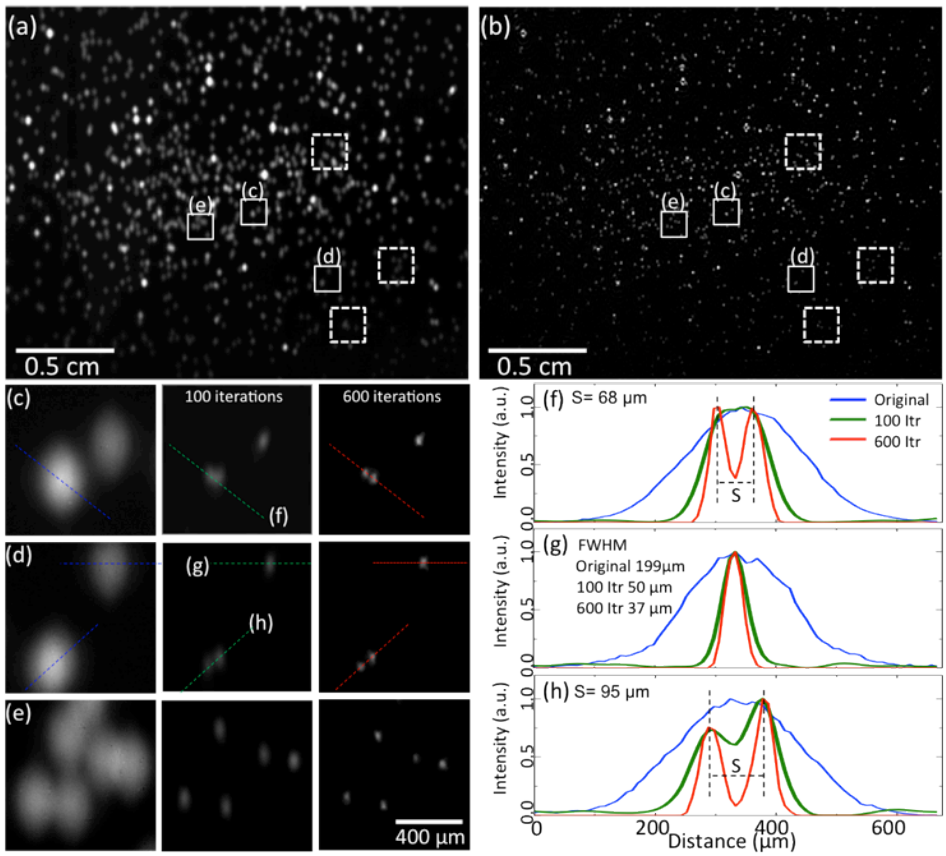

Figure 2-3 | (a) Lensfree fluorescent imaging is illustrated over a FOV of >8 cm^2 for 10µm fluorescent beads (excitation/emission: 495 nm/505 nm). The raw lensfree image (a) was pumped through an LED (see Fig. 2-1) and was acquired with an integration time of 1 s, (b) illustrates the digitally deconvolved fluorescent image of the same FOV. The zoomed images (c–e) are cropped from the raw fluorescent image (a), and next to each zoomed image, the result of the deconvolution process is illustrated as a function of the number of iterations (100 vs. 600). In (c) and (d), the letters and the dashed lines within the frames refer to (f) and (h), which illustrate different cross-sections of the raw and the deconvolved fluorescent images, demonstrating ~5x improvement in fluorescent spot size. Through the iterative deconvolution process two particles that almost completely overlap at the raw lensfree image, see for instance (c–d), can now be separated from each other as shown to the right of (c–d) and in (f, h). Note that the pixel size of the CCD in this experiment is 9 µm, and the resolution of the deconvolved lensfree fluorescent image could be further improved with a smaller pixel.

Next I imaged fluorescently labeled WBCs in diluted whole blood samples. My results (see Fig. 2-4) indicate that the contrast of lensfree fluorescent imaging is sufficiently high even with labeled WBCs in whole blood samples. Note that in this experiment, platelets were also labeled

which contributed to increased background fluorescence. Despite this increased noise, this deconvolution algorithm still performed very well yielding a similar reconstruction performance as also quantified in Fig. 2-4(f–g). In a rare cell experiment, however, such an increase in the background fluorescence would not be present since surface chemistry steps followed by washing of the micro-channel would normally eliminate most of the undesired background fluorescence within the imaging FOV. Non- specific binding in such an experiment still remains an issue to be addressed by appropriate surface chemistry protocols,[9] which are not the focus of this manuscript.

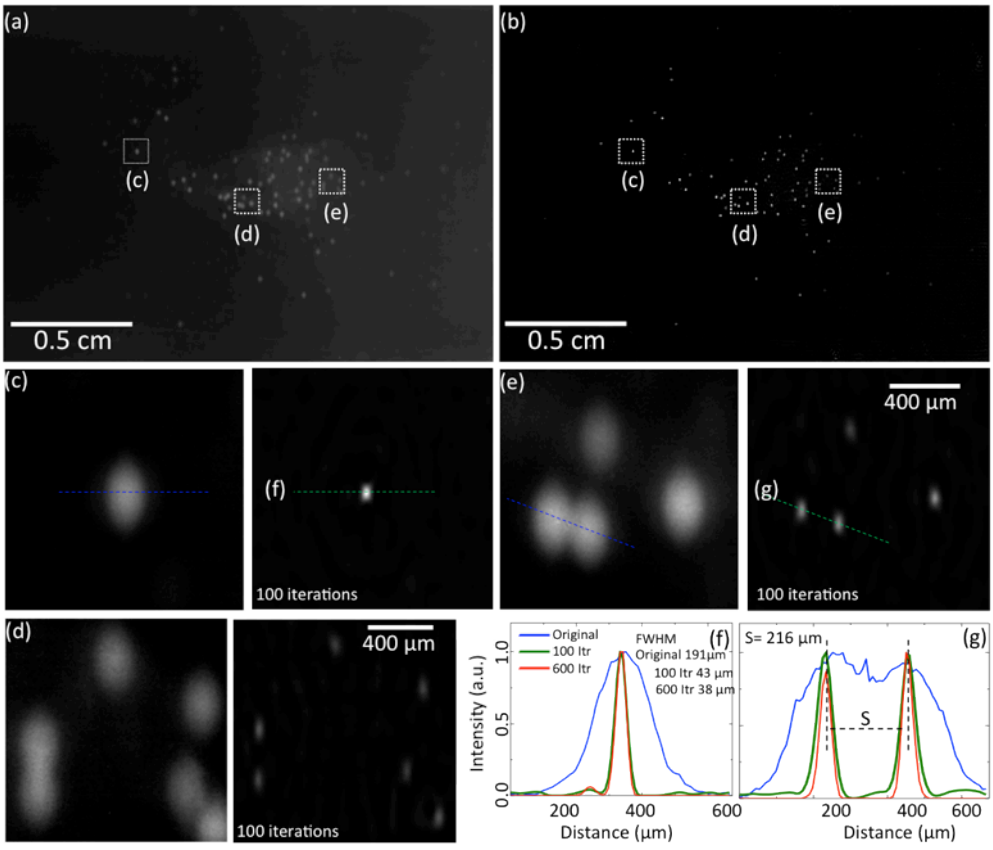

Figure 2-4 | Lensfree fluorescent imaging (a) and the results of the iterative deconvolution algorithm (b) are demonstrated for Calcein Labeled WBCs. The zoomed images at the bottom are cropped from (a) and (b) to illustrate the success of the deconvolution. (f) and (g) illustrate the cross- sections of fluorescent signatures for the raw lensfree image (blue curve) as well as for 100 (green curve) and 600 (red curve) iterations of deconvolution. The FWHM of the deconvolved fluorescent signature in (f) improved by ~5x from 191µm to 38µm. (g) illustrates a similar situation for two overlapping fluorescent signatures.

Note that the same TIR prism interface of Fig. 2-1 also permits lens- free holography[10,11] to be performed for transmission imaging of the same sample volume. By using an incoherent source (such as an LED) that illuminates the sample from the top (Fig. 1), lensfree holographic shadows[11] of the cells/particles can also be imaged on the same chip to create a dual imaging platform. Fig. 2-5 illustrates the performance of this dual imaging capability, where the raw lensfree fluorescent images and their deconvolution results are compared against the vertical transmission images of the same sample volume using lensfree holographic imaging as shown in Fig. 2-1. This imaged sample contained (on purpose) some fluorescent particles as well as some non-fluorescent ones.

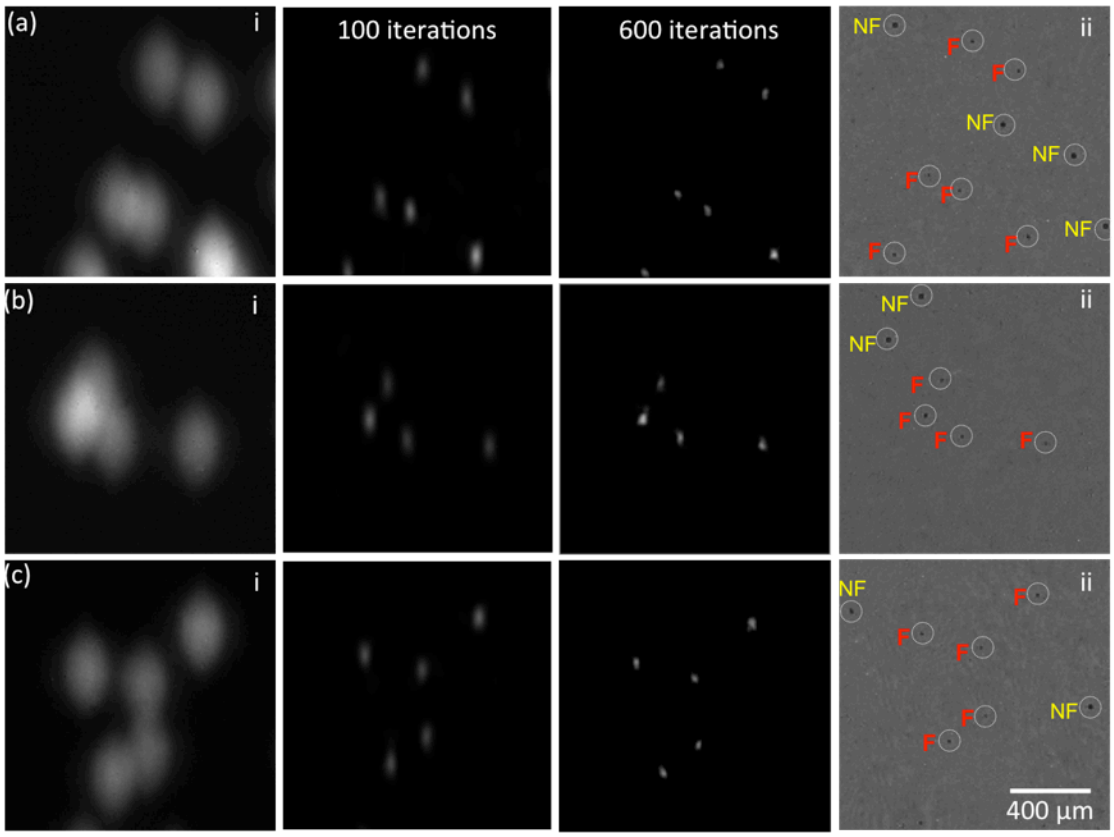

Figure 2-5 | Lensfree holography and on-chip fluorescent imaging is demonstrated within regions shown with the dashed squares of Fig. 2(a–b). In (a–c) left column, the raw lensfree fluorescent images are shown. To the right of these images, the results of digital deconvolution are presented. In (ii) on the far right, lensfree holographic imaging results of the same field of view are presented, which show the shadow signatures of all the particles, both fluorescent (F) and non-fluorescent (NF), whereas the other images on the left only show the fluorescent signatures.

Therefore, the transmission holographic images contained the shadow signatures of all the particles, whereas only the fluorescent ones appeared in the lensfree fluorescent images as illustrated in Fig. 2-5, validating the concept dual imaging on the same lensfree platform. Such a dual-imaging capability would be quite useful especially to increase the specificity and the functionality of lensfree on-chip imaging.

Quite importantly, the detection numerical aperture (NA) of this on-chip system is close to 1.0 since the large-area detector is placed very close to the fluorescent micro-objects, making it highly efficient for photon detection. In other words, only the oblique fluorescent rays that make up the numerical aperture between ~ 1 and ~1.3 (refractive index of the medium inside the channel) are lost without reaching the detector-array. Meanwhile, unlike a lens-based microscope, this large detection numerical aperture does not directly contribute to spatial resolution in this scheme due to its lensfree operation.

Another important feature of this platform is that since the TIR process is very powerful in rejection of the excitation source, a high-end thin-film interference based fluorescent filter is not needed in this case, and an inexpensive plastic-based absorption filter (with a cost of ~0.6 USD per cm^2) can be used, eliminating the need for expensive customized filters for each sensor size. This inexpensive absorption filter (placed between the sample and the sensor planes, with a thickness of e.g., <100 μm) is useful to reject the scattered pump photons that violate the TIR condition, and thus provides a better dark-field background.

In my technique, the use of TIR to block the excitation beam is quite efficient for rejection of high pump powers and it works independent of the excitation and emission wavelengths. This TIR interface is also quite useful since it avoids the use of thin-film based fluorescent filters,

which are wavelength and illumination direction dependent making them inconvenient and costly to customize for lensfree operation. Note that in the reported results (Fig. 2-3 to 2-5), besides TIR, an inexpensive plastic-based absorption filter (less than 5 USD for >8 cm^2 area) is also used to filter out the weakly scattered excitation light that does not obey TIR. The requirements on this filter's performance are greatly reduced due to TIR's efficiency in rejecting the excitation beam.

I would like to point out that the lensfree fluorescent imaging configuration illustrated in Fig. 2-1 should not be confused with existing TIR fluorescence (TIRF) microscopes.[12–14] There are several important differences between the two. Conventional TIRF systems are not lensfree as they often utilize high NA objective lenses as part of a conventional microscope. More importantly, in TIRF configuration, the excitation is achieved through evanescent waves that can only cover a very thin sample volume (<100 nm deep). However, in my technique, the sample excitation occurs through travelling waves, i.e., the entire sample volume (with depths ranging from a few microns to hundreds of microns) can be easily excited. In this sense, my platform is a microscopic imager that is targeted towards lensfree fluorescent imaging of particles and cells on a chip, whereas TIRF microscopy is suited for imaging molecular level interactions over very thin volumes.

2.4 References

1. Shaner, N. C., Steinbach, P. A. & Tsien, R. Y. A guide to choosing fluorescent proteins. Nature Methods **2,** 905–909 (2005).
2. Lichtman, J. W. & Conchello, J.-A. Fluorescence microscopy. Nature Methods **2,** 910–919 (2005).
3. Greenbaum, A. et al. Imaging without lenses: achievements and remaining challenges of wide-field on-chip microscopy. Nature Methods **9,** 889–895 (2012).
4. Coskun, A. F., Su, T.-W. & Ozcan, A. Wide field-of-view lens-free fluorescent imaging on a chip. Lab Chip **10,** 824–827 (2010).
5. RICHARDSON, W. H. Bayesian-Based Iterative Method of Image Restoration. J. Opt. Soc. Am. **62,** 55–59 (1972).
6. Lucy, L. B. An iterative technique for the rectification of observed distributions. The Astronomical Journal **79,** 745 (1974).
7. Biggs, D. S. C. & Andrews, M. Acceleration of iterative image restoration algorithms. Appl. Opt. **36,** 1766–1775 (1997).
8. Manavski, S. A. & Valle, G. CUDA compatible GPU cards as efficient hardware accelerators for Smith-Waterman sequence alignment. BMC Bioinformatics **9,** S10 (2008).
9. Murthy, S. K., Sin, A., Tompkins, R. G. & Toner, M. Effect of Flow and Surface Conditions on Human Lymphocyte Isolation Using Microfluidic Chambers. Langmuir **20,** 11649–11655 (2004).

10. Su, T.-W., Seo, S., Erlinger, A. & Ozcan, A. High-throughput lensfree imaging and characterization of a heterogeneous cell solution on a chip. Biotechnology and Bioengineering **102,** 856–868 (2009).

11. Seo, S., Su, T.-W., Tseng, D. K., Erlinger, A. & Ozcan, A. Lensfree holographic imaging for on-chip cytometry and diagnostics. Lab Chip **9,** 777–787 (2009).

12. Axelrod, D. Total Internal Reflection Fluorescence Microscopy in Cell Biology. Traffic **2,** 764–774 (2001).

13. Schneckenburger, H. Total internal reflection fluorescence microscopy: technical innovations and novel applications. Current Opinion in Biotechnology **16,** 13–18 (2005).

14. Roy, R., Hohng, S. & Ha, T. A practical guide to single-molecule FRET. Nature Methods **5,** 507–516 (2008).

Chapter 3 Reconstruction of lensfree fluorescent images

Parts of this chapter have already been published in Optics Express Vol. 18, 10510 (2010) and PLoS ONE Vol. 6, e15955 (2011).

3.1 Introduction

Compressive sampling (also known as compressive sensing)[1–3] is a recently emerging field that in general aims to recover a function (i.e., a signal) from many fewer measurements/samples than normally required according to the Shannon's sampling theorem. This emerging theory has been recently applied to various fields to bring new insights to measurement and imaging science.[4–14] As an example, it has been used to create a single pixel camera that is especially valuable for imaging at different parts of the electro-magnetic spectrum where high-density-pixel imagers are not readily available or are highly costly[4]. Among many others, another recent achievement of this theory in photonics was the use of compressive decoding in holographic reconstruction of a 3D object volume.[10,11]

In this chapter, I introduce a reconstruction method for on-chip fluorescent imaging modality that utilizes a compressive sampling based algorithm to achieve ~10 μm spatial resolution for imaging of sparse objects over an ultra-large field of view of >8cm^2 without the use of any lenses or mechanical scanning. In this approach, fluorescent samples, positioned e.g., within a micro-channel, are imaged on the on-chip fluorescent microscopy platform presented in Chapter 2. In this platform, the detected lensfree fluorescent image does not have any physical magnification and therefore has a field-of-view (FOV) that is equivalent to the detector active area, covering >8 cm^2. On the other hand, because of its lensfree operation, the detected fluorescent spots are significantly enlarged and distorted due to free pace propagation and large pixel size of the

sensor arrays. I demonstrate that these distortions can be significantly eliminated by using a digital reconstruction/decoding algorithm that is based on compressive sampling theory to achieve ~10μm spatial resolution across the entire detector active area. When compared to my earlier lensfree fluorescent imaging results[15] presented in chapter 2, these compressive decoding based reconstruction results present an improvement in the spatial resolution of this platform without a trade-off in FOV.[16] Furthermore, with this new digital processing approach[16], I also demonstrate lensfree fluorescent imaging with compressive decoding of vertically stacked micro-channels, all in parallel, further increasing the throughput of fluorescent on-chip imaging.

3.2 Theoretical analysis

To briefly go over the relationship between lensfree fluorescent imaging on a chip and compressive sampling theory, let me denote the fluorescent particle/cell distribution within the sample volume with $\bar{c} = [c_1, c_2 \dots c_N]$ where N denotes the number of voxels. To better relate my model to a real imaging experiment, let me also assume that the physical grid size in $\bar{c}$ is d. For visualization purposes, one can think of a simple microfluidic channel such that $\bar{c}$ would represent the points on the active surface of the channel, where the captured cells reside within an imaging area of N x d^2. For multi-layered micro-channels, however, $\bar{c}$ would represent a 3D discrete volume.

For the applications that are of interest to this work, such as wide-field fluorescent cytometry, rare cell analysis and high-throughput micro-array imaging, one can in general assume that $\bar{c}$ is sparse to start with, such that only S coefficients of $\bar{c}$ are non-zero, where S<<N. This assumption is further justified with the unit magnification lensfree geometry since most cells of interest would not be over-sampled due to limited spatial resolution, restricting the value of S for

a practical $\bar{c}$. Therefore, the sparsity of $\bar{c}$ is the first connection to compressive sampling, as it is an important requirement of its underlying theory.[1–3]

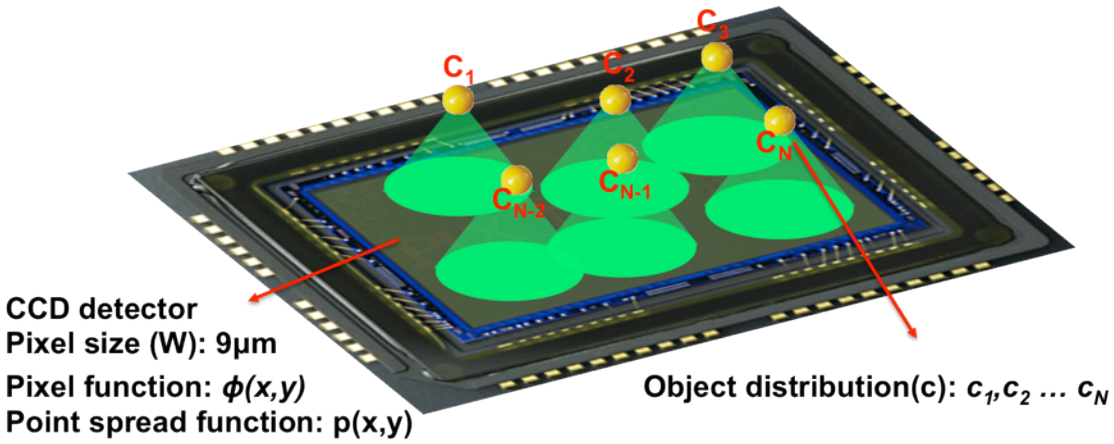

Figure 3-1 | The on-chip fluorescent encoding process is illustrated, where the signal emitted from an object distribution of $\bar{\boldsymbol{c}} = [\boldsymbol{c_1}, \boldsymbol{c_2} \ldots \boldsymbol{c_N}]$ is detected on a sensor array under unit magnification. The emitted fluorescent signal undergoes a diffraction process, which is governed by the point spread function of $\boldsymbol{p(x,y)}$and also the object to detector distance. Upon the diffraction is applied to the signal, the resultant fluorescent pattern is sampled by a CCD sensor that has a pixel function of $\boldsymbol{\phi(x,y)}$ and detector pixel size of W=9 μm. The final acquired image can then be decoded based on a compressive sampling algorithm, which can undo the effect of diffraction, creating high-resolution microscopic images.

In lensfree fluorescent raw images, acquired by the platform presented in Chapter 2, as shown in Fig. 3-1(c), $\bar{c}$ uniquely determines the intensity distribution that is impinging on the detector-array. For each non-zero element of $\bar{c}$, a wave is transmitted, and after passing through different layers on the chip it incoherently adds up with the waves created by the other fluorescent points within the sample volume. Therefore, one can write the intensity distribution right above the detector plane (before being measured/sampled) as:

$$f(x,y) = \sum_{i=1}^{N} c_i \, \psi_i(x,y) \tag{3.1}$$

where $\psi_i(x,y)$ represents the 2D wave intensity right before the detector plane that originated from the physical location of c_i . The analytical form of ψ_i can be derived for any particular lensfree imaging geometry such as the one presented in Fig. 3-1. However, from a practical point

of view, it can easily be measured for each object plane by using e.g., small fluorescent particles, which is the approach taken in this work.

Furthermore, it is straightforward to see that the functional form of ψ_i for a given object plane is space invariant, which means that $\psi_i(x,y) = p(x-x_i, y-y_i)$, where $p(x,y)$ is the incoherent point spread function (PSF) of the system for a given object layer, and (x_i, y_i) denotes the physical location of c_i. Note that in this definition, $p(x,y)$ has no relationship to the pixel size at the detector since Eq. (3.1) describes the intensity right before the sampling plane. Therefore, for the lensfree fluorescent imaging geometry of Fig. 3-1, one can in general write:

$$f(x,y) = \sum_{i=1}^{N} c_i \, p(x-x_i, y-y_i) \tag{3.2}$$

For multiple layers of fluorescent objects, a similar equation could also be written where the incoherent point-spread functions of different layers are also included in the summation. Equation (3.2) relates the "already" sparse fluorescent object distribution ($\bar{c}$) to an optical intensity distribution that is yet to be sampled by the detector array. The representation basis provided by $\psi_i(x,y)$ is surely not an orthogonal one since it is based on lensfree diffraction. This is not limiting the applicability of compressive decoding to this work since $\bar{c}$ is assumed to be already sparse, independent of the representation basis. On the other hand, the fact that $\psi_i(x,y)$ does not form an orthogonal basis limits the spatial resolution that can be compressively decoded, since for closely spaced c_i values, the corresponding $\psi_i(x,y)$ would be quite similar to each other for a given detection signal to noise ratio (SNR). This is related to the restricted isometry property[1,2] of my system as will be discussed later on; however its physical implication is nothing new since it is already known that I trade off spatial resolution to achieve wide-field lensfree fluorescent imaging with unit magnification.

Next, sampling of $f(x,y)$ at the detector-array can be formulated as:

$$I_m = \iint f(x,y) \cdot \phi\,(x - x_m, y - y_m) \cdot dx \cdot dy \tag{3.3}$$

where $\Phi = \phi(x - x_m, y - y_m)$ represents the sampling/measurement basis; m=1:M denotes the m^{th} pixel of the detector-array with center coordinates of (x_m, y_m); and $\phi(x,y)$ represents the pixel function, which can be approximated to be a detection constant, K, for |x|,|y|≤W/2 (assuming a square pixel size of W) and 0 elsewhere, |x|,|y|>W/2. In this notation, the fill-factor of the detector-array together with the quantum efficiency etc are all lumped into K. Note that in this work, I have used W=9 μm and W=18 μm (through pixel binning).

With these definitions, the lensfree fluorescent imaging problem of this manuscript can be summarized as such: based on M independent measurements of I_m, I would like to estimate the sparse fluorescent source distribution, $\bar{c}$, at the sample.

To give more insight, Eq. (3.3) models a hypothetical near-field sampling experiment, where each pixel of the CCD measures part of $f(x,y)$. For an arbitrary intensity distribution $f(x,y)$ impinging on the detector array, a few pixel values (I_m) can surely not represent the entire function. However, if the sampled intensity profile at the detector plane is created by a sparse distribution of incoherent point sources located in the far - field, then much fewer pixels can potentially be used to recover the source distribution based on compressive decoding. For this decoding to work efficiently, each pixel should ideally detect "some" contribution from all the c_i values, which implies the need for a relatively wide point spread function. However since spreading of the fluorescence also decreases the signal strength at the detector plane, the optimum extent of the point spread function is practically determined by the detection SNR. On one extreme, if the same sparse source distribution ($\bar{c}$) was hypothetically placed in direct contact with the CCD pixels, this would not permit any compressive decoding since each

incoherent point source can now only contribute to a single pixel value. For instance two sub-pixel point sources that are located on the same pixel would only contribute to that particular pixel, which would make their separation physically impossible regardless of the measurement SNR. However, the same two sub-pixel point sources could be separated from each other through compressive decoding if they were placed some distance above the detector plane, such that more pixels could detect weighted contributions of their emission.

Considering non-adaptive imaging here (i.e., no a priori information about the possible x-y locations of the fluorescent particles/cells), I have not used a sub-set of the pixel values (I_m) to reconstruct $\bar{c}$. Therefore, for a single layer of object, using a unit magnification as in Fig. 3-1, I have N x d^2 = M x W^2. In this work, to claim a spatial resolution of ~10μm at the object plane, I used d = 2-3 μm, which implies N ≥ 9M for W=9 μm. **For some experiments, I have also used a pixel size of W=18μm with d=2μm, implying N=81M. Furthermore, for multi-layer experiments (to be reported in the next section) where two different fluorescent channels were vertically stacked and simultaneously imaged in a single snap-shot, I had N=18M, which all indicate compressive imaging since the number of measurements (M) are significantly smaller than the number of reconstructed points (N).**

As already known in compressive sampling literature, the effectiveness of the decoding process to estimate $\bar{c}$ in this technique should also depend on the maximum spatial correlation between Φ_m and ψ_i for all possible m=1:M and i=1:N pairs. Accordingly, this maximum spatial correlation coefficient defines the measure of incoherence between sampling and representation bases, which can then be related to the probability of accurately reconstructing $\bar{c}$ from M measurements[1–3]. For a given object plane, because of the shift invariant nature of both Φ_m and ψ_i, this coherence calculation is equivalent to calculation of the correlation between the pixel

function $\phi(x,y)$and the incoherent point-spread function $p(x,y)$. The smaller the correlation between these two spatial functions is, the more accurate and efficient the compressive decoding process gets. Based on this, a smaller pixel size would further help in this lensfree on-chip scheme by reducing this maximum correlation coefficient, i.e., increasing incoherence between ϕ_m and ψ_i.

Thus, I can conclude that the primary function of compressive sampling in this work is to digitally undo the effect of diffraction induced spreading formulated in Equations (3.1)–(3.2) through decoding of lensfree image pixels indicated in Eq. (3.3).

Finally, I would like mention that the above analysis could be also done using a different set of measurement and representation bases without changing the end conclusions. In the above analysis, I did not include the diffraction process as part of the measurement, and therefore the measurement basis only involved the pixel sampling at the detector-array. As an alternative notation, I could have also used $\psi_i(x,y) = \delta\,(x - x_i, y - y_i)$ for the representation basis, which implies that Ψ is an identity matrix. This is not a surprising choice since the object, $\bar{c}$ is already sparse and therefore the sparsifying matrix can be seen as an identity matrix. Based on this definition of the representation basis, the measurement basis Φ_m will now need to include both the diffraction and the pixel sampling processes. Following a similar derivation as in Equation (3.3), the measurement basis now becomes:

$$\Phi_m = \iint p(x - x_i, y - y_i) \cdot \phi\,(x - x_m, y - y_m) \cdot dx \cdot dy \tag{3.4}$$

As expected, the correlation behavior between Φ_m and ψ_i for all possible m and i pairs remains the same as before, yielding the same set of conclusions that I arrived using the previously discussed choice of bases. While it is just a matter of notation, with this new pair of bases, it is also easier to qualitatively relate the spatial resolution to restricted isometry property

(RIP) of the system. RIP is a measure of the robustness of sparse signal reconstruction for N>M and S<<N[1–3]. For this new choice of bases, RIP holds if all the possible subsets of S columns taken from $\Phi\Psi = \Phi$ are nearly orthogonal to each other. Assuming that the pixel size is much narrower than the incoherent psf of the object layer of interest, I can then approximate:

$$\Phi_m \approx p(x_m - x_i, y_m - y_i) \iint \cdot \phi\,(x - x_m, y - y_m) \cdot dx \cdot dy$$

$$= K \cdot W^2 \cdot p(x_m - x_i, y_m - y_i) \tag{3.5}$$

Therefore for RIP to hold in this lensfree system, for any arbitrary S choices of i = 1:N, the sub-set of functions $\Phi_m \approx K \cdot W^2 \cdot p(x_m - x_i, y_m - y_i)$ should be nearly orthogonal in (x_m, y_m). If one purely relies on diffraction, this condition can be harder to satisfy for densely spaced (x_i, y_i) which practically limits the achievable spatial resolution for a given detection SNR. Once again, physically this is not surprising since it is already known that I trade off resolution to achieve wide-field lensfree fluorescent imaging on a chip. Structured surfaces could potentially help achieving a better resolution by randomly breaking the space invariance of the incoherent psf, which is not going to be covered within the context of this manuscript.

3.3 Methods

The main function of the compressive sampling theory in this work is to recover the distribution of the fluorescent points that created the 2D lensfree image sampled at the detector array. Knowing the incoherent psf of this system for each object layer, for an arbitrary distribution of fluorescent sources (within e.g., a single micro-channel or a stack of vertical channels), one can easily calculate the expected lensfree image at the detector-array. Using this fact, through a compressive sampling algorithm[17] I optimize the distribution of the fluorescent sources at the object volume based on a given 2D lensfree fluorescent measurement. The choice

of this compressive decoder[17] is highly suitable for the presented wide FOV fluorescent imaging platform since it is especially designed for sparse signal recovery from large data sets.

To be more specific, the reconstruction/decoding process can be formulized as an l1-regularized least squares problem (LSP)[17], such that:

$$\hat{c} = argmin\|I_{det} - M_{conv} \cdot \bar{c}\|_2 + \beta \cdot \|\bar{c}\|_1 \quad (3.6)$$

where $\beta > 0$ is a regularization parameter (typically between 1 and 10); I_{det} is the detected raw fluorescent image at the sensor-array (in a vector form); M_{conv} represents the 2D convolution matrix based on the incoherent point spread function of the system; c is the fluorescent source distribution that creates the lensfree image at the detector plane; and $\|\bar{x}\|_p = (\sum_{i=1}^{n}|x_i|^p)^{1/p}$ represents the l_p norm of vector $\bar{x}$. For multiple micro-channels that are vertically stacked (see e.g., Fig. 3-6), there is a separate M_{conv} for each source layer. The compressive decoder used in this work[17] is based on truncated Newton interior-point method and rapidly provides a sparse solution ($\hat{c}$) for Eq. (3.6) especially for large-scale data sets using a non-negativity constraint, which is surely satisfied for fluorescent imaging in general.

Once physical parameters (i.e., dimensions and distances) are fixed in this imaging geometry, the resulting psf for a given object plane is easily measured using e.g., small diameter fluorescent particles that are imaged at a low concentration. Fig. 3-2 illustrates simplified schematics of this concept, where a compressive decoding algorithm processes the raw lensfree fluorescent image together with the measured point-spread function of the platform to create a sparse image of the fluorescent source distribution located at the object plane.

3.4 Results and discussion

In this lensfree fluorescent imaging modality, because the fluorescent detection occurs at extremely oblique angles on the sensor chip, depending on the opto-electronic design of the

pixels and the underlying circuitry of a given chip, the fluorescent point-spread function (PSF) of this platform would exhibit a noticeable variance in its 2D pattern from one sensor-chip to

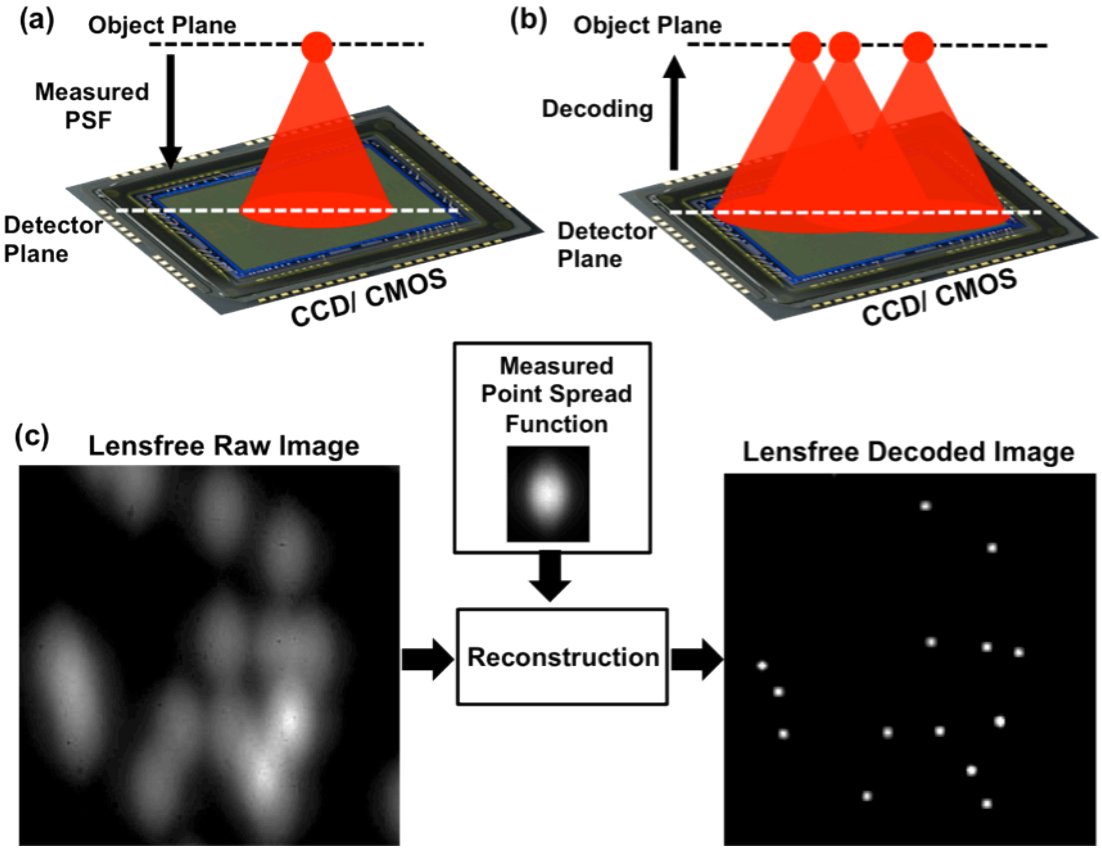

Figure 3-2 | (a) Using isolated fluorescent particles the lensfree point-spread function of a given object layer is physically measured. (b) Based the knowledge of this measured point-spread function, any arbitrary fluorescent object distribution at the chip plane can be decoded using a compressive sampling based optimization algorithm. The procedure is also summarized in (c) where the raw lensfree fluorescent image is compressively decoded using the measured point-spread function of the platform to increase the spatial resolution of the fluorescent image.

another as illustrated in Fig. 3-3, which requires calibration of each chip by measuring its unique PSF. Therefore, I imaged and reconstructed fluorescent micro-objects using different sensor chips in this work[18] to demonstrate sensor independent performance of the lensfree imaging modality.

Initially, to evaluate the effect of PSF on the reconstruction performance of the lensfree on-chip imaging platform, I imaged small fluorescent micro-beads (4 μm diameter, Excitation:

505nm, Emission: 515nm) to measure the PSF functions by using two different CCD sensor chips namely, KODAK KAF-8300 (5.4 μm pixel size, ~2.4 cm^2 active imaging area) and KODAK KAF-39000 (6.8 μm pixel size, ~18 cm^2 active imaging area). Figs. 3-4 and 3-5 illustrate these measured point-spread-functions for these CCD chips, respectively.

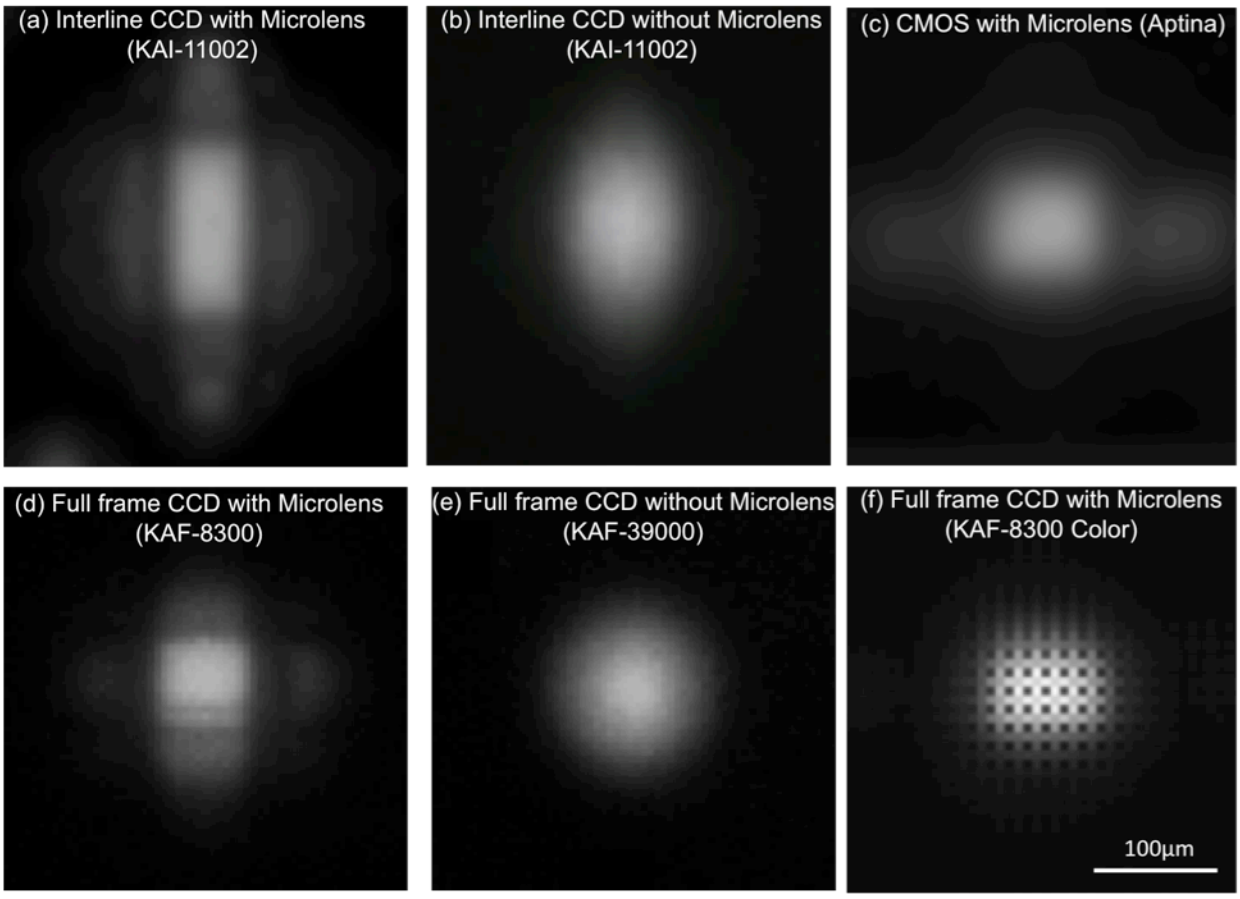

Figure 3-3 | The PSFs imaged by an interline CCD (KAI-11002) with Microlens and without Microlens are illustrated in (a) and (b), respectively. Note that Microlenses are designed for plane wave illumination; thus the oblique rays emerging from fluorescent objects are not uniformly sampled at the detector plane. Furthermore, the circuitry of an interline sensor distorted the fluorescent detection, creating ellipsoid PSF for a small fluorescent micro-object. The PSFs imaged by a Full frame CCD (KAF-8300 and KAF-39000) with Microlens and without Microlens are illustrated in (d) and (e), respectively. Note that Microlens based detection still distorts the fluorescent pattern, however, PSF acquired by the full frame sensor without Microlens provides perfectly circular Gaussian distribution. (c) PSF acquired by a CMOS sensor with Microlens is also shown. All of the PSFs presented above (a-e) were acquired with monochrome sensors; however, the use of an RGB (Color) sensor chip could also enable color imaging on the lensfree imaging platform. Such a PSF acquired by a color CCD sensor (KAF-8300) is illustrated in (f), exhibiting a Bayer pattern due to the color filters on the active pixels on the sensor.

As demonstrated in these figures, the PSF of each sensor, under similar imaging conditions, is quite different from the other, which is mostly dictated by the opto-electronic design of each CCD chip. For instance, the full-width-half-maximum (FWHM) of KAF-8300 PSF is ~ 80µm,

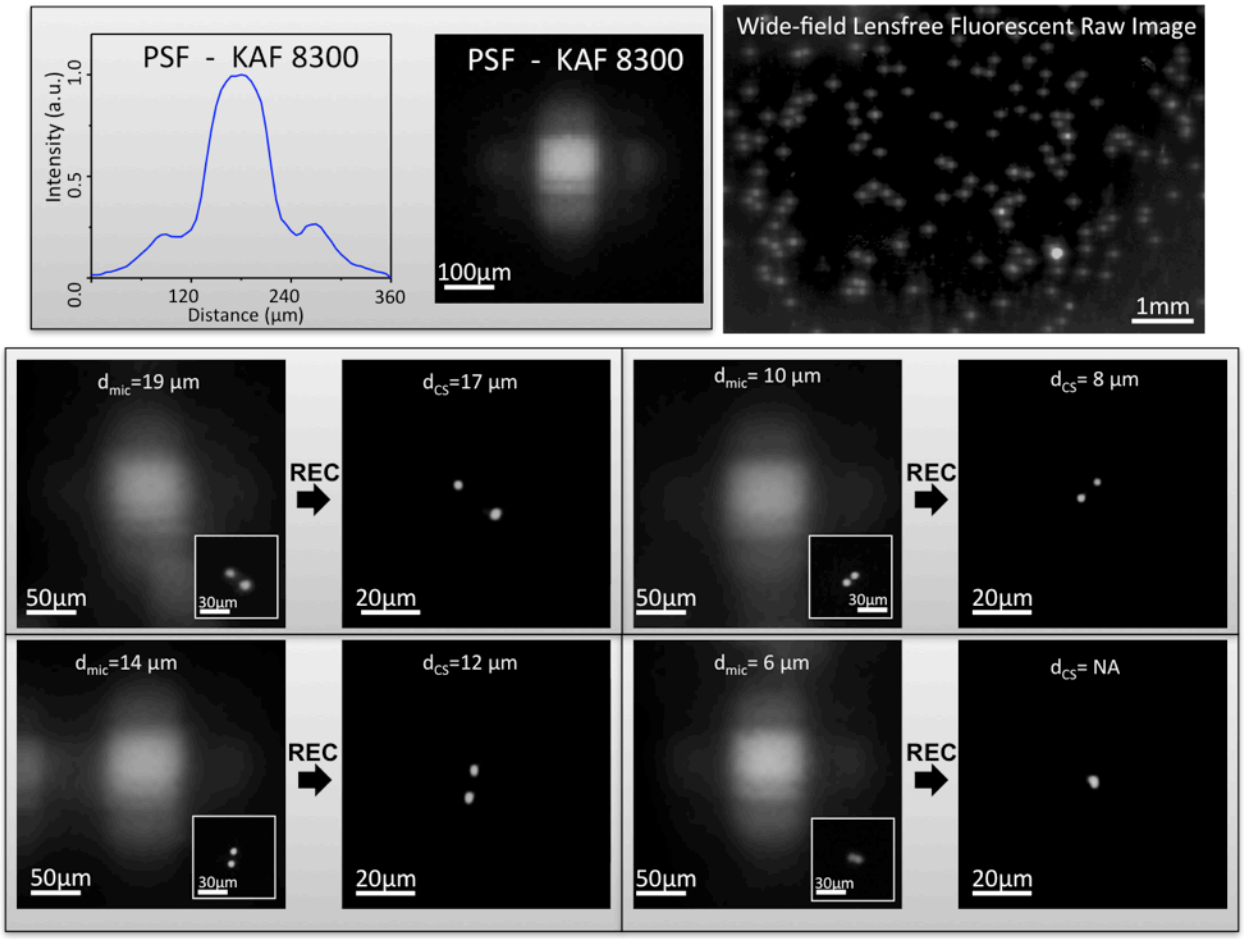

Figure 3-4 | (Top Row) illustrates wide-field lensfree fluorescent imaging results for 4 µm fluorescent beads recorded using KAF-8300 sensor. The measured point-spread-function (PSF) of the same system (corresponding to 4 µm diameter fluorescent beads) is also shown at the top left. The 2D pattern of this PSF presents a unique signature, which is mostly dictated by the opto-electronic design of the CCD chip. (Middle and Bottom Rows) Lensfree fluorescent images of various 4 µm bead-pairs are shown. For comparison purposes, the inset images in each frame also show conventional fluorescent microscope images of the same closely-packed beads. Based on these microscope images, the center-to-center distances ($\mathbf{d_{mic}}$) between the fluorescent particles are calculated. Using compressive sampling (CS - as indicated with the solid black arrows), lensfree fluorescent raw images are decoded to resolve the individual fluorescent particles from each other. These decoding results nicely match to the corresponding microscope comparison images for $\mathbf{d_{mic}} \geq 10\mu m$, indicating a resolution of ~10µm. $\mathbf{d_{CS}}$ refers to the center-to-center distances of these resolved fluorescent particles in the decoded lensfree images. For $\mathbf{d_{mic}} = 6\mu m$ case, however, compressive decoding does not succeed in resolving the particles.

which implies a fairly limited resolving power for raw fluorescent images as illustrated in Fig. 3-4. The same conclusion also applies to KAF-39000 PSF with an FWHM of ~120μm, as a result of which, closely packed 4μm fluorescent particles cannot be resolved from each other in raw lensfree images (see Fig. 3-5).

On the other hand, compressive decoding of these raw lensfree images (using the measured PSFs) permits close to an order-of-magnitude increase in the resolving power by rapid digital reconstruction of the fluorescent distribution at the object plane (for further details refer to the Experimental Methods Section). The performance of this compressive decoding approach is quantified in Figs. 3-4 and 3-5 (for KAF-8300 and KAF-39000 chips, respectively), which both indicate a resolution of ~10 μm that is independently confirmed using conventional fluorescent microscope images of the same 4μm particle pairs (refer to the inset images in Figs. 3-4 and 3-5). These experimental results successfully demonstrate the sensor-chip independent decoding performance of the lensfree fluorescent imaging platform.

The resolution limit in the lensfree imaging results is mainly dictated by the detection signal-to-noise-ratio (SNR), since the tails of the measured PSF, after certain signal strength, falls below the noise floor of the sensor. In these reported experiments (Figs. 3-4 and 3-5) the CCD chips were kept in room temperature, and therefore further improvement in resolution (beyond ~10μm) can potentially be achieved by active cooling of the opto-electronic sensors without a trade-off in the imaging FOV, which spans the entire active area of the CCD, i.e., ~2.4 cm^2 for KAF-8300 and ~18 cm^2 for KAF-39000. I should also note that, with larger area sensors, the imaging FOV of this platform could be even further increased while maintaining a similar resolution level. On a related note, it is important to emphasize that the pixel size in lensfree compressive imaging is “not” a fundamental limitation for spatial resolution if the detection SNR

is sufficiently high. Consider for instance lensfree imaging of two fluorescent points that are directly located on a single pixel. Under this condition, it is theoretically and practically impossible to resolve these two fluorescent points that fall within a single dummy pixel. However, the same two sub-pixel fluorescent points can be resolved from each other using lensfree compressive imaging if several pixels could detect weighted averages of their

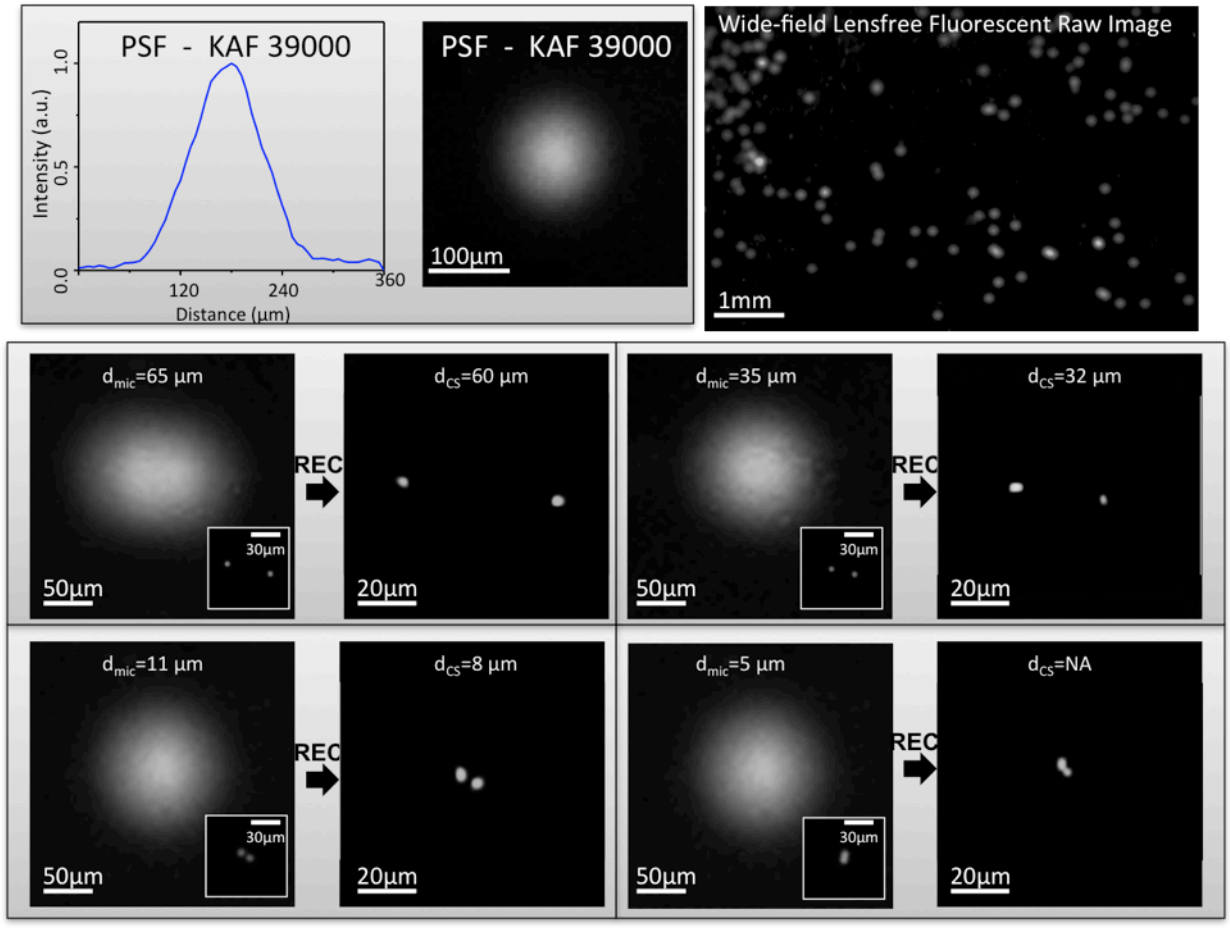

Figure 3-5 | Same as in Fig. 3-4, except for KAF-39000 sensor-chip is used. Similar to Fig. 3-4, compressive decoding enables a lensfree spatial resolution of ~10 μm on a chip. Because of its different sensor design, the measured PSF of KAF-39000 is quite different than the PSF of KAF-8300 shown in Fig. 3-4. This, however, does not pose a limitation for achieving a similar spatial resolution. These experimental results, together with Fig. 3-4, successfully demonstrate the sensor-chip independent decoding performance of the lensfree fluorescent imaging platform.

fluorescent emission. Therefore, under an appropriate detection SNR, if the physical gap between the fluorescent objects and the sensor plane can be increased to perform efficient spatial

encoding of the fluorescent objects, resolving of arbitrarily sub-pixel point sources would be feasible. The fundamental limitation to this resolving power is therefore the detection SNR, which determines how many pixels can independently and accurately measure the lensfree fluorescent contributions of the particles. Therefore, for a practical SNR level, there is always an optimum gap range between the object and sensor planes, which were found to be ~50–200 μm for the CCD chips used in this platform at room temperature.

Furthermore, I also demonstrate lensfree imaging and compressive decoding of vertically stacked micro-channels, where micro-particles in a suspension were stacked together using thin glass slides creating a vertical separation of 50 μm (between each layer) as illustrated in Fig. 3-6, respectively. Using this multilayer imaging configuration, the throughput of the lensfree fluorescent imaging platform can be increased by another factor of, e.g., 2–3. This requires compressive decoding of a three-dimensional fluorescent object distribution based on two-dimensional lensfree fluorescent images, as illustrated in Fig. 3-6. In these decoding results, the lensfree point-spread functions corresponding to each vertical layer are separately measured, which are then used to compute the hypothetical lensfree fluorescent image at the detector plane for an initial estimate of the three-dimensional object distribution. This computed image is then compared with the measured lensfree fluorescent image for iterative modification of the three-dimensional fluorescent object estimation until convergence is achieved.[16]

Finally, I would like to also point out the possibility that the compressive fluorescence decoding approach used in this work may also be extended to lens-based fluorescent microscopy, and in particular to recent fluorescent super-resolution approaches including PALM and STORM[19,20] to potentially reduce the number of frames that is required for 2D or 3D fluorescent imaging. Such a compressive decoding approach, however, would need to be carefully tested in

terms of achievable localization accuracy and potential artifacts for multiple fluorescent points located within a diffraction limited spot.

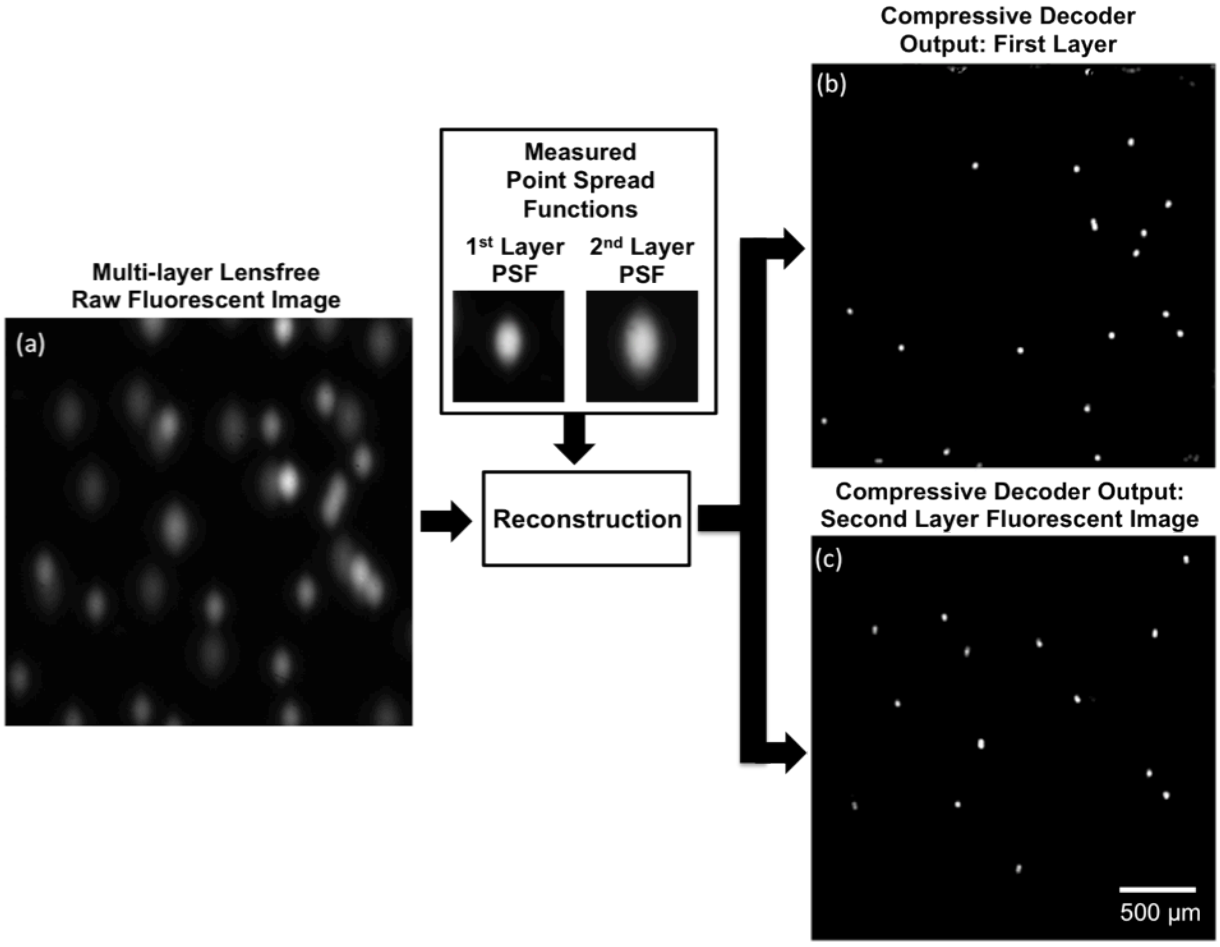

Figure 3-6 | (a) Lensfree fluorescent imaging of 2 layers that are vertically separated by ~50µm is illustrated. The compressive decoding results of these 2 raw lensfree images for each vertical channel are illustrated in (b-c). Based the knowledge of this measured PSFs for each layer (both 1st layer and 2nd layer), any arbitrary fluorescent object distribution acquired from multiple vertical layers at the chip plane can be simultaneously decoded using a compressive sampling based optimization algorithm.

3.5 References

1. Candes, E. J. & Tao, T. Near-Optimal Signal Recovery From Random Projections: Universal Encoding Strategies? IEEE Transactions on Information Theory **52,** 5406 –5425 (2006).
2. Candès, E. J., Romberg, J. K. & Tao, T. Stable signal recovery from incomplete and inaccurate measurements. Communications on Pure and Applied Mathematics **59,** 1207–1223 (2006).
3. Donoho, D. L. Compressed sensing. IEEE Transactions on Information Theory **52,** 1289 – 1306 (2006).
4. Duarte, M. F. et al. Single-Pixel Imaging via Compressive Sampling. IEEE Signal Processing Magazine **25,** 83 –91 (2008).
5. Gehm, M. E., John, R., Brady, D. J., Willett, R. M. & Schulz, T. J. Single-shot compressive spectral imaging with a dual-disperser architecture. Opt. Express **15,** 14013–14027 (2007).
6. Wagadarikar, A., John, R., Willett, R. & Brady, D. Single disperser design for coded aperture snapshot spectral imaging. Appl. Opt. **47,** B44–B51 (2008).
7. Chan, W. L., Moravec, M. L., Baraniuk, R. G. & Mittleman, D. M. Terahertz imaging with compressed sensing and phase retrieval. Opt. Lett. **33,** 974–976 (2008).
8. Romberg, J. Imaging via Compressive Sampling. IEEE Signal Processing Magazine **25,** 14 –20 (2008).
9. Lustig, M., Donoho, D. & Pauly, J. M. Sparse MRI: The application of compressed sensing for rapid MR imaging. Magnetic Resonance in Medicine **58,** 1182–1195 (2007).
10. Brady, D. J., Choi, K., Marks, D. L., Horisaki, R. & Lim, S. Compressive Holography. Opt. Express **17,** 13040–13049 (2009).

11. Denis, L., Lorenz, D., Thiébaut, E., Fournier, C. & Trede, D. Inline hologram reconstruction with sparsity constraints. Opt. Lett. **34,** 3475–3477 (2009).

12. Yu, H. & Wang, G. Compressed sensing based interior tomography. Physics in Medicine and Biology **54,** 2791–2805 (2009).

13. Lu, Y. et al. Source Reconstruction for Spectrally-resolved Bioluminescence Tomography with Sparse A priori Information. Opt. Express **17,** 8062–8080 (2009).

14. Gao, H. & Zhao, H. Multilevel bioluminescence tomography based on radiative transfer equation Part 1: l1 regularization. Opt. Express **18,** 1854–1871 (2010).

15. Coskun, A. F., Su, T.-W. & Ozcan, A. Wide field-of-view lens-free fluorescent imaging on a chip. Lab Chip **10,** 824–827 (2010).

16. Coskun, A. F., Sencan, I., Su, T.-W. & Ozcan, A. Lensless wide-field fluorescent imaging on a chip using compressive decoding of sparse objects. Optics Express **18,** 10510 (2010).

17. Kim, S.-J., Koh, K., Lustig, M., Boyd, S. & Gorinevsky, D. An Interior-Point Method for Large-Scale l1-Regularized Least Squares. IEEE Journal of Selected Topics in Signal Processing **1,** 606 –617 (2007).

18. Coskun, A. F., Sencan, I., Su, T.-W. & Ozcan, A. Lensfree Fluorescent On-Chip Imaging of Transgenic Caenorhabditis elegans Over an Ultra-Wide Field-of-View. PLoS ONE **6,** e15955 (2011).

19. Betzig, E. et al. Imaging Intracellular Fluorescent Proteins at Nanometer Resolution. Science **313,** 1642–1645 (2006).

20. Rust, M. J., Bates, M. & Zhuang, X. Sub-diffraction-limit imaging by stochastic optical reconstruction microscopy (STORM). Nature Methods **3,** 793–796 (2006).

Chapter 4 Lensfree fluorescent microscopy using planar fiber-optic arrays

Parts of this chapter have already been published in Optics Express Vol. 18, 10510 (2010) and Journal of Visualized Experiments Vol. 54, 3181 (2011).

4.1 Introduction

Fiber-optic arrays have been widely deployed for imaging and sensing applications[1–3] in biomedical sciences. Such fiber-optic bundles are composed of highly densely packed thousands of single core fibers (e.g., 3-10 micron diameters) that can transmit optical fields from one side to another, allowing rapid, high-throughput and multiplexed analysis of chemical and biological compounds, as well as cell-based assays. The use of fluorescence based signal transduction methods, combined with the fiber-optic arrays, could also bring specificity and sensitivity to the high-throughput fiber-based imaging and sensing platforms, enabling extremely versatile and miniaturized screening technologies. There have been efforts employing fluorescence based fiber optic systems for high-resolution microscopy[4], micro-well array development[5], as well as microsphere-based arrays[6]. These methods have achieved satisfactory performances for their specific uses operating based on the image relay property of fiber-optic arrays; however, fiber-optic cables can be employed for more practical functions such as PSF engineering[7], especially for an on-chip imaging geometry[8,9] presented in chapters 1-3.

Along the same lines, I demonstrate the use a passive optical components such as fiber-optic arrays (i.e., also known as faceplate) illustrated in Fig. 4-1, to control the extend of this spatial spreading and to engineer the PSF of the lensfree fluorescent imaging platform. Placing such a fiber-optic faceplate between the fluorescent objects and the detector-array, a better control over

the spatial spreading of lensfree fluorescent signatures can be achieved without affecting the imaging FOV (see e.g., Fig. 4-2), providing also a higher resolution lensfree raw images. Another important advantage of using a faceplate for on-chip lensfree fluorescent imaging is that it provides thermal isolation of the micro-fluidic chip and the cells from the sensor-array.

In this lensfree fluorescent imaging platform, the functions of the fiber-optic arrays can be summarized as follows: (1) This passive fiber component can engineer the PSF of the on-chip imaging platform by converting the free space propagation modes of the fluorescent emission from the objects into guided modes of a two-dimensional fiber-optic waveguide array such that the spatial spreading of fluorescent intensity can be tuned to narrow the point-spread function and increase the digital SNR of the lensfree fluorescent image (see e.g., Fig. 4-2). (2) Another physical function of the faceplate used in my experiments is to collect the fluorescent emission from the specimen with an effective numerical aperture of ~0.3 (i.e., smaller than 1.0) and to guide it to the detector array. However, since the fluorescent emission from the objects spreads with an effective numerical aperture of 1 over the air gap above the faceplate, several oblique fluorescent rays (corresponding to higher angles than the acceptance NA of each fiber) remain unguided. These unguided rays (which undergo various partial reflections over multiple fiber cross-sections) are also detected at the sensor plane and are incoherently superimposed onto the fluorescent signal that is guided through the core of each fiber. However, since the thickness of the faceplate is relatively large (~ e.g., 3 mm to 10 mm), the contribution of these unguided fluorescent waves is weaker than the guided fluorescent signal, creating another degree of freedom for engineering the spatial width and the SNR of the lensfree point-spread function of this platform.

4.2 Materials and methods

Set-up: In this lens-free on-chip imaging technique (Fig. 4-1), the microfluidic chip of interest is loaded onto an optoelectronic sensor array (e.g., a CCD) where the fluorescent cells/particles are pumped at their proper excitation wavelength using e.g., a simple light emitting diode (LED) through the side facet of a rhomboid prism (base: 25 x 35 mm; height: 17 mm, Edmund Optics) as illustrated in Fig. 4-1. This incoherent excitation beam, after interacting with the sample volume, is reflected through a total internal reflection (TIR) process occurring at the bottom facet of the sample device. Upon the removal of the weakly scattered excitation light using a long pass absorption filter (Kodak Wratten Color Filter 12, <30 dB for <500 nm; <0.1 mm thick, Edmund Optics), only the fluorescent emission from the excited cells/particles is collected via a fiber-optic faceplate (e.g., Edmund Optics, NT55-142) and delivered to a large-format charge coupled device (CCD, KAI-11002, Kodak) without the use of any lenses over the entire FOV of the sensor-array (~2.5 cm x 3.5 cm).

Digital processing: The faceplate in this on-chip imaging geometry, even though significantly reduces the signal spreading at the detector plane as shown in 4-2, also brings its own distortion to the recorded images by creating a unique PSF at the detector plane. The exact spatial form of this 2D incoherent point-spread function is determined by the faceplate periodicity and lattice, numerical aperture of the individual fibers, the distance between the sample plane and the upper surface of the faceplate, as well as the distance between the exit plane of the faceplate and the detector array. Once all these parameters are fixed in this imaging geometry (see 4-1 for details), the resulting psf for a given object plane is measured using e.g., small diameter fluorescent particles that are imaged at a low concentration. Quite importantly, the physical gap (~50-100 μm) between the sample and the faceplate planes, together with the gap between the faceplate and the detector planes (~75-100 μm) ensure that this incoherent point spread function is space

invariant all across the imaging FOV, which enables the use of a single point spread function for decoding of each object plane. This unique measured psf is then used to reconstruct the raw images acquired in this platform based on the compressive decoding enabled reconstruction method described in chapter 3.

Fluorescent micro-beads: Raw fluorescent bead solutions are combined with DI water to optimize the concentration of the samples. 10 μL of fluorescent bead solution is mixed with 40 μL, 5 mL, and 20 mL of DI water for 10 μm, 4μm and 2 μm diameter beads, respectively. Heterogeneous solutions of various beads (e.g., non-fluorescent and fluorescent) are prepared as needed by mixing different bead solutions with each other. The final sample solution is then sandwiched between prism and glass slide.

White blood cell labeling: A volume of ~100 μL whole blood is mixed with ~1 mL of red blood cell lysing buffer (eBioscience). After incubation for ~3 min, the lysed blood solution is centrifuged and the pellet layer is resuspended in ~200 μL of PBS (Phosphate buffered saline). To label the nucleic acid of the cells with fluorescence dyes, 5 μL of 1mM SYTO®16 is added to the 200 μL of resuspension, after which the sample is incubated for ~30 min in dark at room temperature. Second centrifuging is applied to this labeled sample, where the supernatant is removed to decrease the background noise due to fluorescent emission from unbound dyes. White blood cell pellet layer is resuspended in PBS that can then be transferred to a micro-fluidic chip for lensfree on-chip fluorescent imaging (see e.g., Fig. 4-10).

4.3 Results and discussions

To validate and quantify the performance of the on-chip imaging technique employing fiber-optic arrays, I imaged fluorescent micro-particles using the lensfree set-up of Fig. 4-1. Together with the lensfree fluorescent image enhancements coming from the use of a faceplate in this

imaging geometry, I also applied the previously discussed (in chapter 3) compressive sampling based reconstruction algorithm to the improved PSFs, yielding even higher resolution final

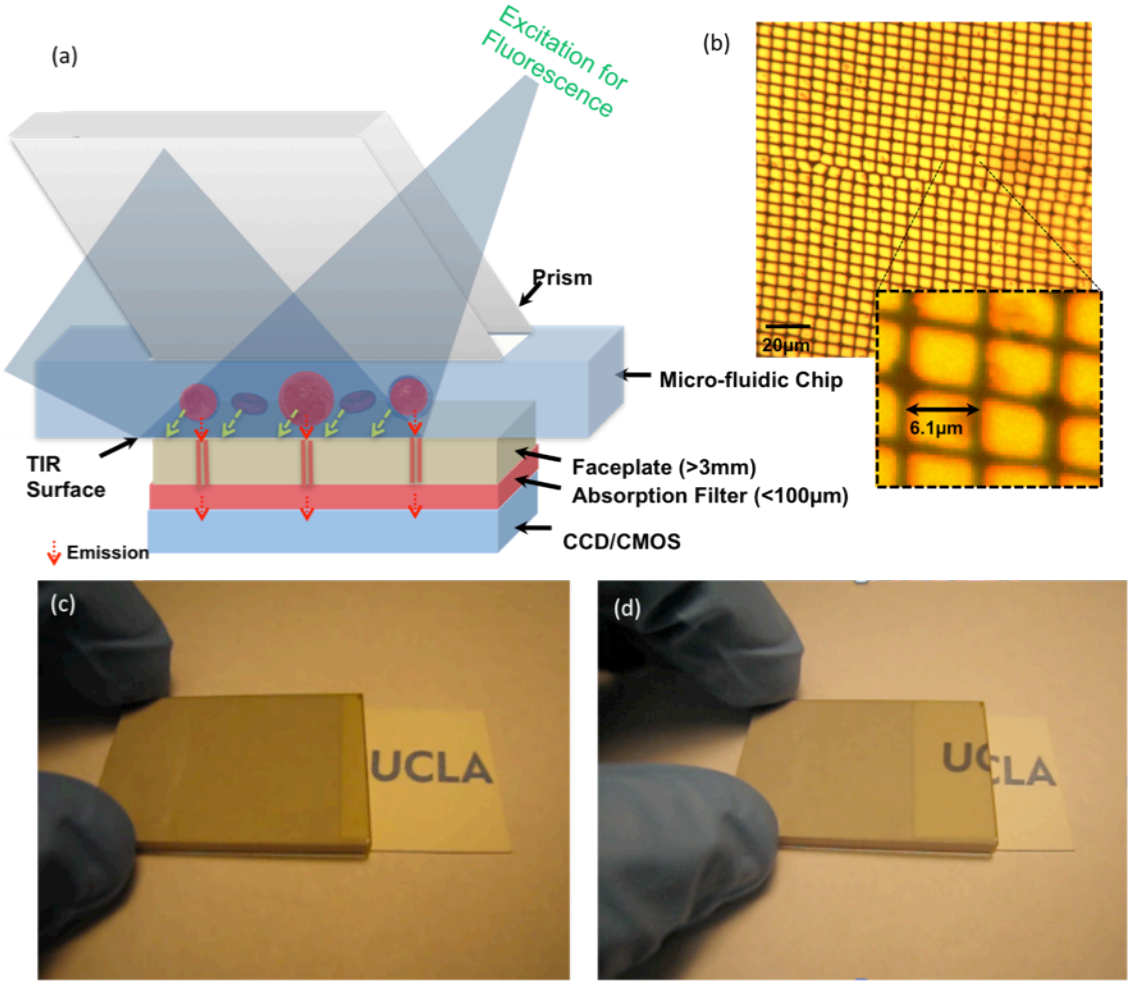

Figure 4-1 | (a) An alternative lensfree on-chip fluorescent imaging geometry is illustrated. In this configuration, when compared to the setup shown in Fig. 2-1, an additional planar optical component, i.e., a fiber optic faceplate, is used to collect the fluorescent emission and then to deliver it to a CCD, engineering the PSF of the on-chip imaging platform. (b) 10× microscope image of the faceplate that was used in my experiments is shown. The pitch size of the faceplate is 6.1 μm. (c)-(d) The UCLA image is shown without and with the faceplate, demonstrating the image relay function of the fiber-optic arrays, respectively.

lensfree images as a result of combined improvements coming from faceplate and digital processing. The results of these on-chip fluorescent imaging experiments are summarized Figs. 4-2 to 4-11, which point to several important features of this platform.

First, the comparison provided in Fig. 4-2(a) and (b) indicates that the fiber-optic faceplate in this imaging geometry (Fig. 4-1) significantly reduces the diffraction induced spreading of the fluorescent signatures of the objects. Specifically, based on Fig. 4-2 I conclude that the FWHM

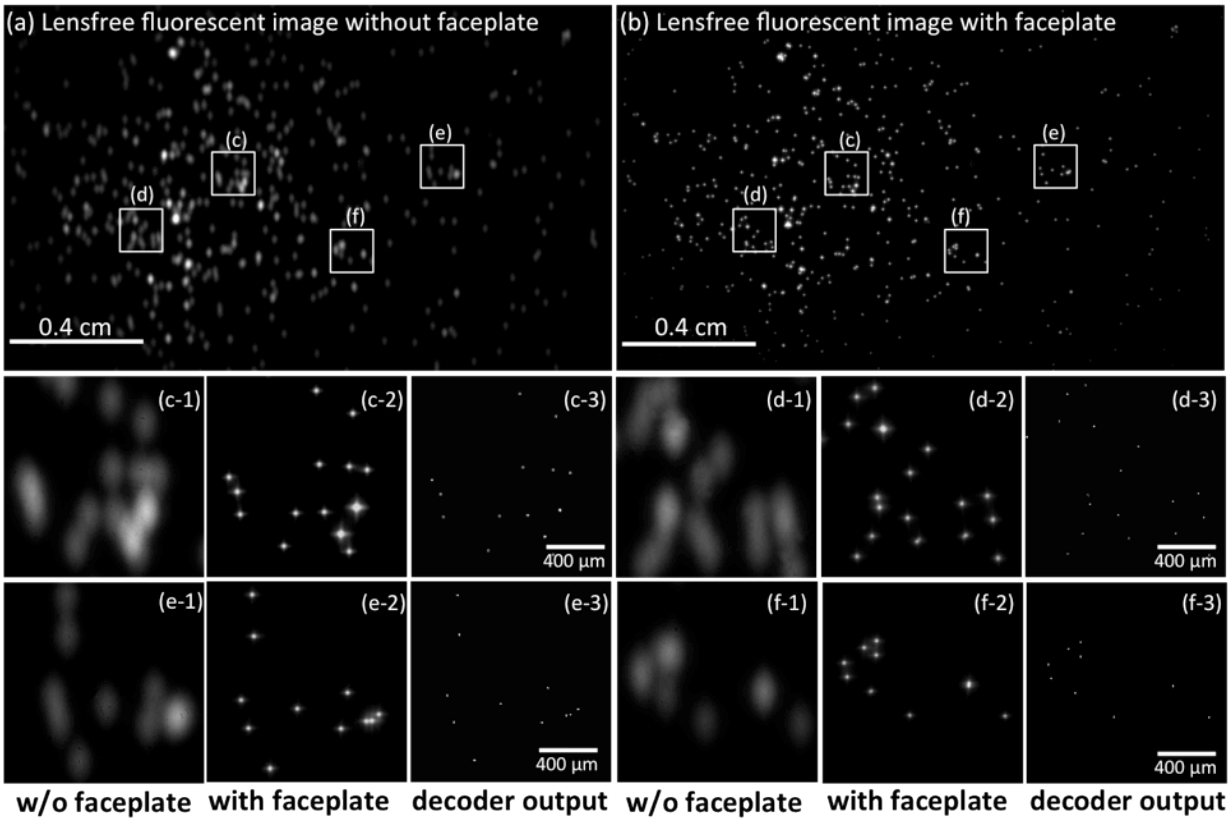

Figure 4-2 | (a-b) Lensfree fluorescent images of 10 µm particles are compared with and without the faceplate. To make this comparison fair, except the faceplate, all the other dimensions in Fig. 4-1, are kept the same in both of these experiments. With the use of the faceplate, the spatial spreading of the fluorescent signatures at the CCD plane is reduced from ~180 µm down to ~36 µm (FWHM). This improvement is also evident in the comparison that is provided by the digitally zoomed regions shown in (c1-f1) and (c2-f2), which correspond to experiments "without the faceplate" and "with the faceplate", respectively. The same zoomed images of (c2-f2) are also decoded using a compressive sampling algorithm to yield (c3-f3). As further quantified in Figs. 4-4, 4-5 and 4-6 this compressive decoding process improves the spatial resolution down to ~10 µm all across the field of view of the sensor.

of the fluorescent signatures at the detector plane is now reduced by ~5 fold, from ~180 µm down to ~36 µm using the faceplate (note that except the faceplate thickness, all the other vertical distances are kept the same in both configurations - with and without the faceplate - to provide a fair comparison). This improvement is quite important as it permits a better detection

SNR and a higher spatial resolution to be achieved, which will be further quantified in the next figures.

Figs. 4-2(c3), (d3), (e3) and (f3) demonstrate the compressive decoding results of the raw lensfree images acquired with a faceplate based configuration. Note that the same compressive sampling algorithm also performs very well even without the use of a faceplate to resolve rather closely spaced fluorescent particles from each other as highlighted in Fig. 4-3.

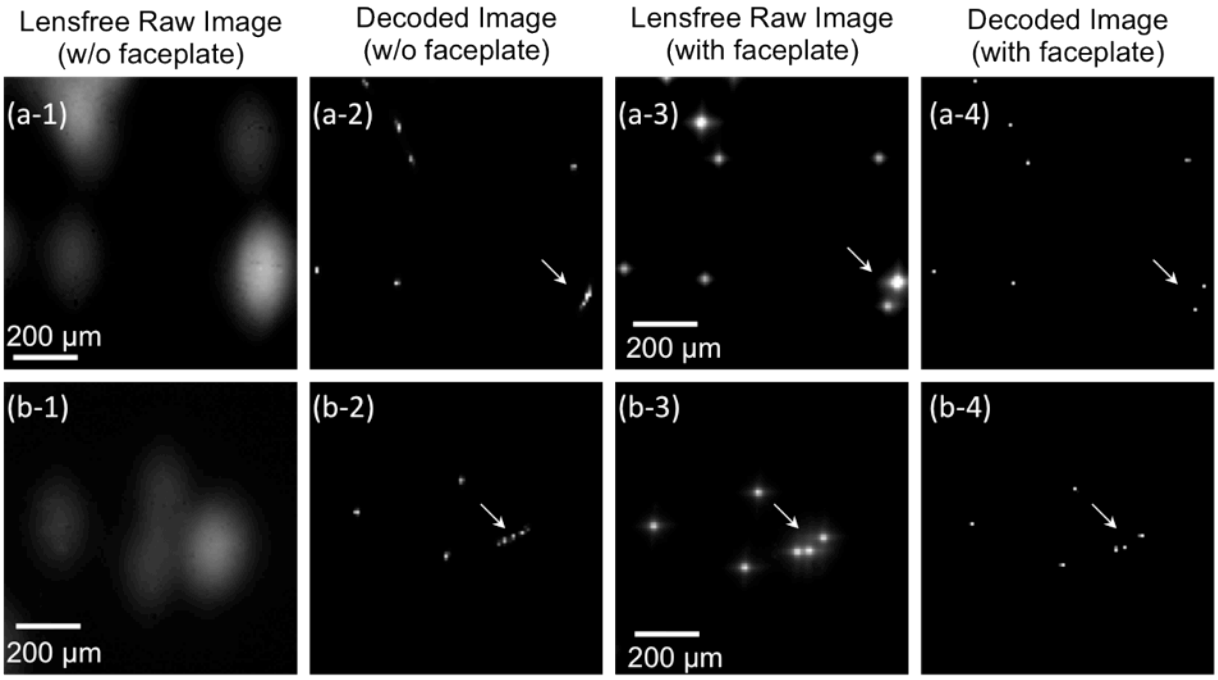

Figure 4-3 | (a1) shows a digitally zoomed lensfree fluorescent image of 10µm particles that is obtained without the use of a faceplate. (a2) illustrates the output of the compressive decoder for the same image in (a1). (a3) shows the same region of interest imaged this time using a faceplate as shown in Fig. 4-1(a). The compressive decoder output of image (a3) is shown in (a4). The same story is repeated in (b1) through (b4) for a different region of interest. The arrows in these images specifically point to regions where the improvement due to the faceplate becomes apparent to better resolve closely spaced fluorescent particles.

However, Fig. 4-3 also compares the performance of the faceplate for decoding of the same field-of-view, which clearly illustrates the superior performance of faceplate based decoded images in terms of resolving closely spaced fluorescent particles without any reconstruction artifacts or ambiguities (e.g., refer to the arrows in Fig. 4-3).

I further quantified the spatial resolution of this compressive decoding process on the faceplate based lensfree images by resolving several closely packed fluorescent micro-particles from each other. Figs. 4-4, 4-5 and 4-6 summarize my experimental results which clearly demonstrate resolving two fluorescent particles that are separated by g~10μm (center to center). Figs. 4-4 and Fig. 4-5 are obtained using 10μm and 2μm diameter fluorescent particles, respectively; and the pixel size in the decoded images is 3μm and 2μm, which implies N = 9M and N~20M for Fig. 4-4 and Fig. 4-5 (see chapter 3 for details), respectively. In Fig. 4-6, I further reduced M (see chapter 3 for details) by pixel binning at the detector-array such that the pixel size became W = 18μm. This implies N = 81M (see chapter 3 for details), which still permitted reconstruction of 2μm particles that were separated by g~12μm (center to center) as shown in Fig. 4-6. The computation times of these decoded images are fairly small ranging between 0.1min to 0.5min using an Intel Centrino Duo Core, 1GHz PC.

I would like to also provide a quantitative comparison of the presented compressive sampling based reconstruction approach[9] over some of the existing deconvolution methods that could potentially be used for the same purpose. One such numerical recipe is the Lucy-Richardson algorithm[10–12] which relies on the knowledge of the incoherent point spread function to iteratively converge to the maximum-likelihood estimation of the fluorescence source distribution based on the detected image. This algorithm is not restricted to sparse objects only and has been shown to be quite effective converging within typically a few hundred iterations to the source distribution[8]. A comparison of the performance of this algorithm against compressive sampling based reconstruction is demonstrated in Fig. 4-4 (bottom row), which clearly indicates the advantages of the compressive decoding approach especially in terms of spatial resolution. Fig. 4-4 demonstrates that, for the same set of lensfree fluorescent measurements, the

compressive decoder achieves ~10μm resolution, while the Lucy-Richardson deconvolution algorithm achieves ~20μm. This behavior is intuitively expected since the Lucy-Richardson algorithm does not use the sparsity of the object as an optimization constraint. Besides resolution, another important difference between the two approaches is that unlike compressive sampling which can easily perform multi-layer reconstruction for sparse objects as illustrated in Figs. 4-7 and 4-8, the Lucy Richardson algorithm would need to be significantly modified to handle 3D reconstruction. On the other hand, conventional deconvolution algorithms that do not rely on a sparsity constraint (such as the Lucy Richardson algorithm) could potentially better handle highly dense fluorescent samples, where the sparsity condition of the object is no longer satisfied.

Another important dimension of the presented lensfree approach is its ability to reconstruct the distribution of fluorescent micro-objects located at multiple micro-channels that are stacked vertically. This enables to decode the 2D lensfree fluorescent image at the detector-array into a 3D distribution through compressive sampling, which is especially important to further increase the throughput of fluorescent on-chip imaging. A proof of concept demonstration of this capability is presented in Figs. 4-7 and 4-8 where the fluorescent micro-particles (10μm diameter) located at two and three different micro-channels, respectively, were imaged and decoded all in parallel. In these two experiments the fluorescent channels were vertically separated by 50 and 100 μm, respectively. In Fig. 4-7 the comparison of the decoding results with and without the faceplate is also provided for the same sample volume, which illustrates the superior performance of the faceplate case for resolving overlapping fluorescent signatures from each other. In Fig. 4-8 the decoding results with the faceplate is also provided for 3 different layers that are vertically separated by 100 μm. Two different regions are imaged using a faceplate, and

the raw lensfree images are then decoded to reveal the distribution of the fluorescent particles at each layer. In the raw lensfree images, the fluorescent signatures from the 3rd layer are rather

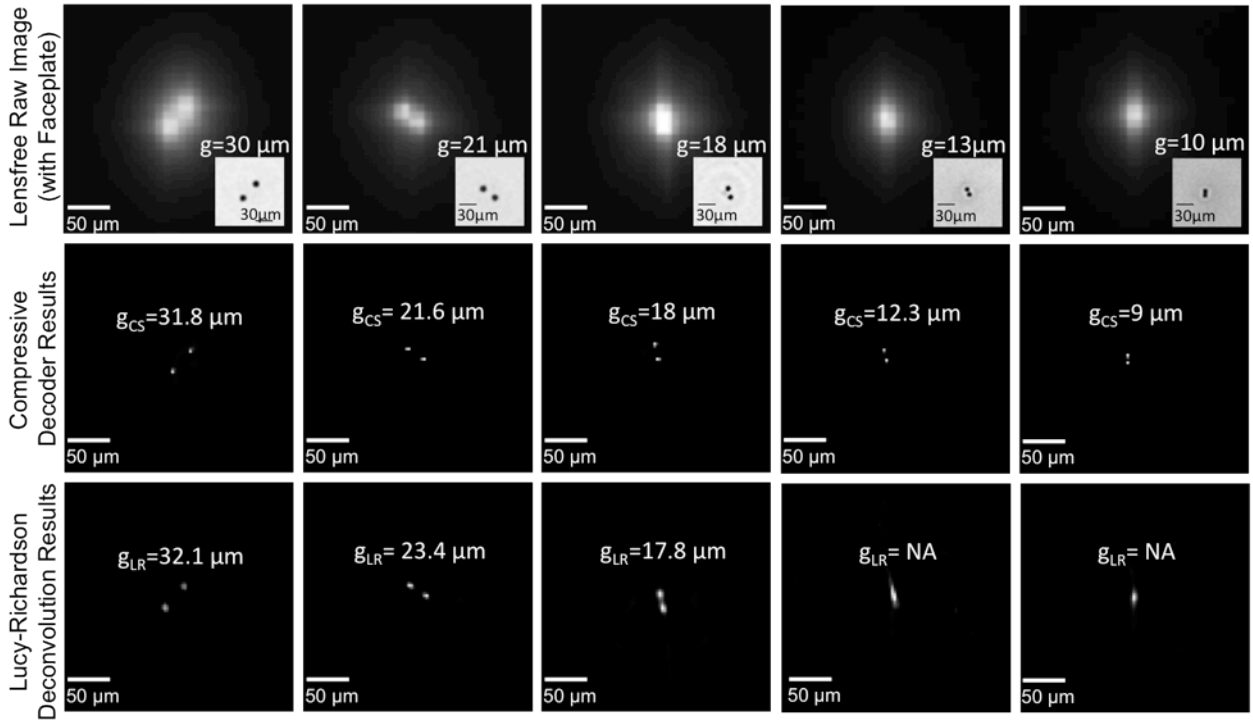

Figure 4-4 | (Top Row) shows raw lensfree fluorescent images of different pairs of 10 µm diameter particles imaged using the set-up of Fig. 4-1. As the particles get closer to each other, their signatures in the raw lensfree image become indistinguishable to the bare eye. The inset images in the top row (bottom right corner of each image) illustrate transmission microscope images of the same particles from which the center-to-center distance (g) in each case is calculated only for comparison purposes. (Middle Row) illustrates the results of the compressive decoding process for each lensfree image of the top row. gCS refers to the center-to-center distance of the resolved fluorescent particles in each image, where CS denotes "compressive sampling". Even for g = 10µm case (far right column), I can clearly resolve the fluorescent particles from each other with g_{CS} = 9µm. The pixel size in the decoded image is 3µm, whereas the raw lensfree image has been sampled with a pixel size of W = 9µm at the detector array, i.e., **N = 9M**. The reason that the reconstructed points for g_{CS} = 9µm case do not touch each other (unlike the microscope image shown in the inset) is that the incoherent point-spread function of the system has been estimated using 10µm diameter fluorescent particles. Refer to Figs. 4-5, 4-6 for imaging of 2µm diameter fluorescent particles. The computation times of these decoded images vary between 0.1 min to 0.5 min on an Intel Centrino Duo Core, 1GHz PC. (Bottom Row) illustrates the deconvolution results of the Lucy-Richardson algorithm for the same set of lensfree images shown in the top row. g_{LR} refers to the center-to-center distance of the resolved fluorescent particles in each image, where LR denotes "Lucy-Richardson". The number of iterations [19] in these deconvolution results ranged between 200 and 400, matching with the overall computation time of the CS results for each image. These results indicate that the LR algorithm can resolve particles with g~18 µm, whereas the CS decoder can clearly resolve particles with g~10 µm.

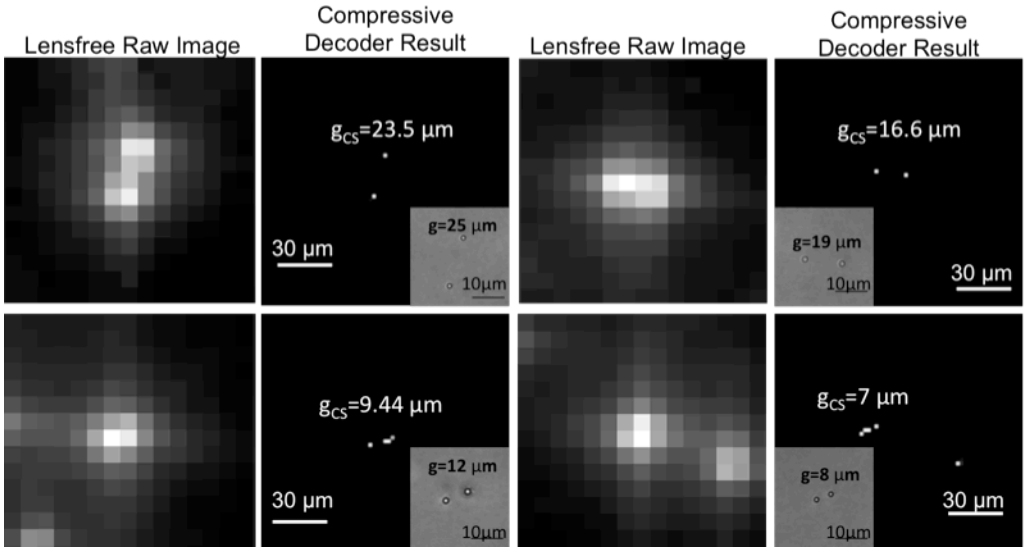

Figure 4-5 | Same as Fig. 4-4 except for 2µm diameter fluorescent particles. The raw lensfree images are decoded to resolve closely spaced particles from each other. The inset images (bottom right corner of each decoded image) illustrate regular transmission microscope images of the same particles from which the center-to-center distance (g) in each case is calculated for comparison purposes. The bottom row illustrates resolving 2µm particles that are separated by g ~12µm and 8µm. The pixel size in the raw lensfree fluorescent images is W = 9µm, whereas the pixel size of the decoded images is 2µm, i.e., **N~20M**. The point-spread function of the system has been estimated using 2 µm diameter fluorescent particles imaged at a low concentration.

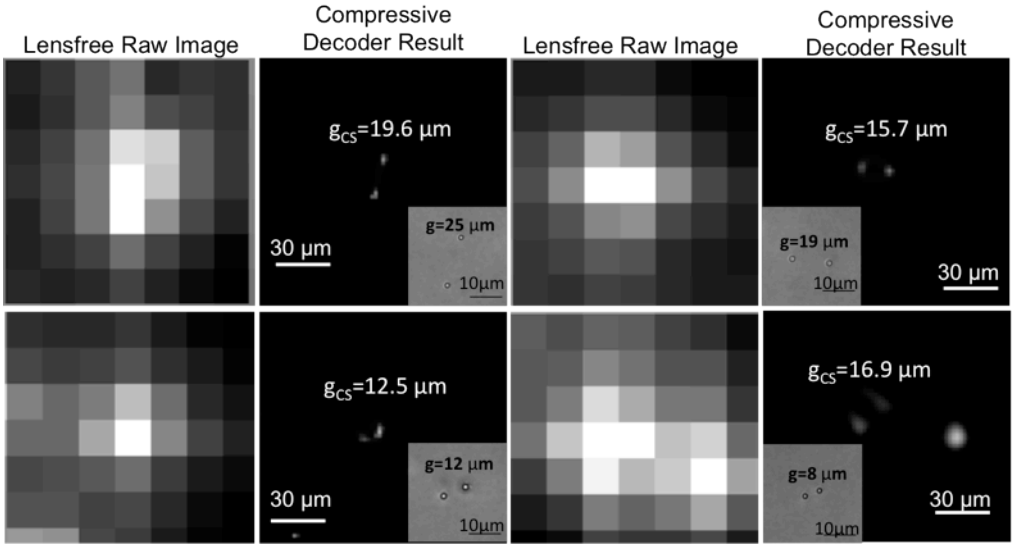

Figure 4-6 | Same as Fig. 4-5 (2µm fluorescent particles) except with a pixel size of W = 18µm at the detector-array, such that 4 pixels of the CCD are now binned together. Similar to Fig. 4-5, the raw lensfree images are decoded to resolve closely spaced fluorescent particles from each other. The pixel size of the decoded images is still 2µm, same as in Fig. 4-5, which this time implies **N = 81M**. Because of a significant reduction in M when compared to Fig. 4-5, the performance of the compressive decoding is relatively degraded, which is especially visible for reconstruction of g = 8µm case (bottom right corner). Regardless, even with N = 81M, I have achieved decoding of sub-pixel objects as shown in e.g., g = 12 µm case.

faint and need careful examination to see them with the bare eye, whereas the decoder output for the 3rd layer faithfully resolves their location. Such a computational strength would be quite significant to further increase the throughput in e.g., imaging cytometry experiments.

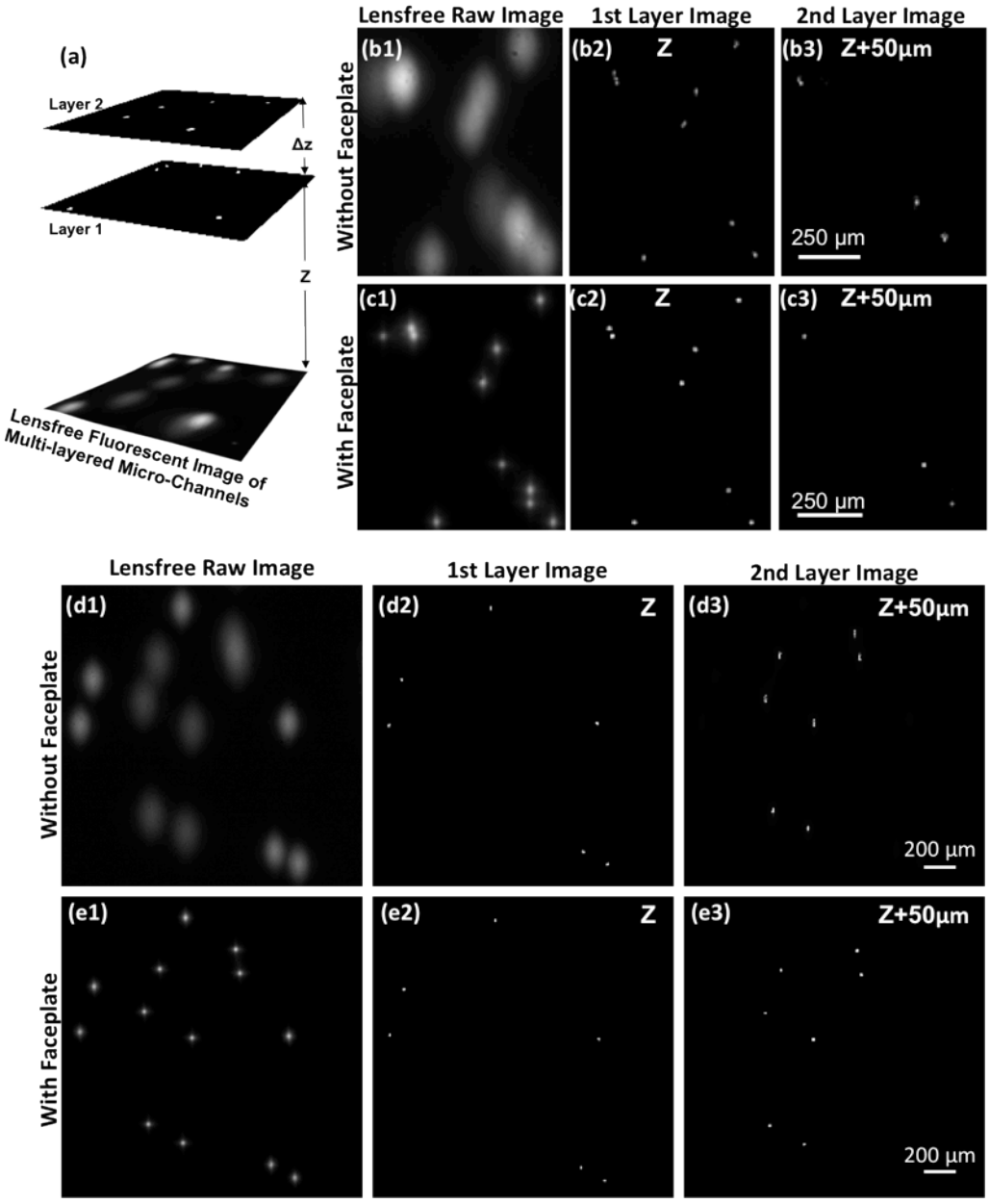

Figure 4-7 | (a) Lensfree fluorescent imaging of 2 layers that are vertically separated by ~50μm is illustrated. (b1) and (d1) show two different digitally cropped regions of the large FOV that are imaged without the use of a faceplate (see Fig. 4-1). The compressive decoding results of these 2 raw lensfree images for each vertical channel are illustrated in (b2-b3) and (d2-d3), respectively. The same regions are also imaged using the faceplate as shown in (c1) and (e1). The compressive decoding results of these 2 raw lensfree images for each vertical channel are also illustrated in (c2-c3) and (e2-e3), respectively.

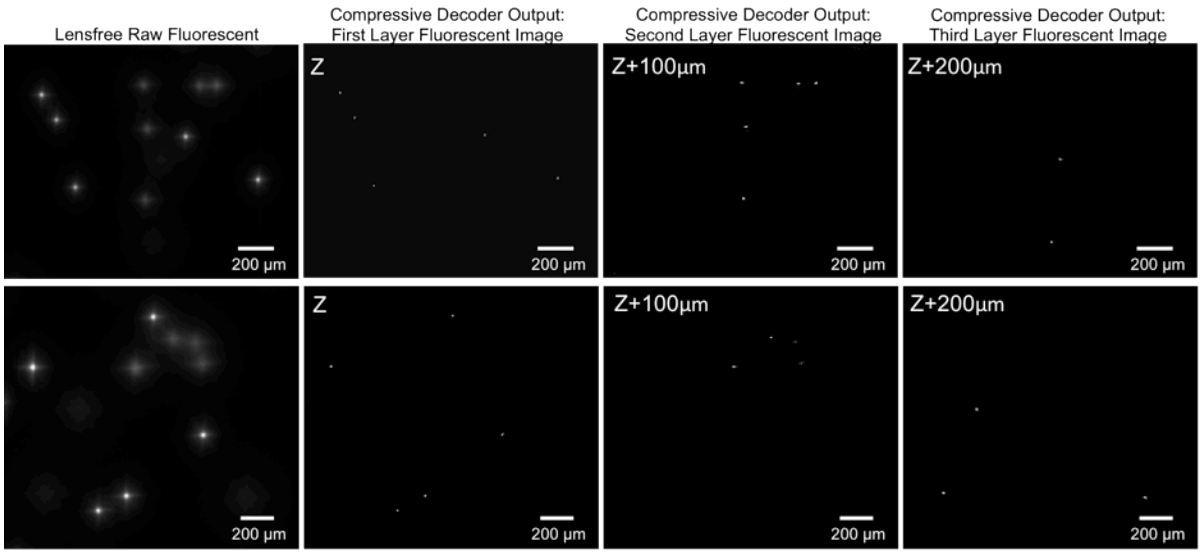

Figure 4-8 | Same as in Fig. 4-7, except for 3 fluorescent layers that are vertically separated by ~100 µm from each other. Two different regions are imaged using a faceplate, and the raw lensfree images are then decoded to reveal the distribution of the fluorescent particles at each layer. In the raw lensfree images, the fluorescent signatures from the 3rd layer are rather faint and need careful examination to see them with the bare eye, whereas the decoder output for the 3rd layer faithfully resolves their location. Such a computational strength would be quite significant to further increase the throughput in e.g., imaging cytometry experiments.

Having characterized the performance of the compressive decoding enabled on-chip fluorescent microscopy system; I would like to further demonstrate the wide-field imaging of a heterogeneous sample[13] containing 4 µm and 10 µm green fluorescent particles as shown in Fig. 4-9. For comparison purposes, 10X microscope objective images are also provided, which agree well with my lensfree fluorescent images. The significance of this figure is that the compressive sampling based reconstruction algorithm can also decode different signal levels (i.e., brighter for 10 µm object and dimmer for 4 µm object) without an issue and then create the higher resolution microscopic images as illustrated in previous figures (e.g., 4-2 to 4.9). I should note that the regularization parameter (β) should be fine tuned depending the on the lensfree raw images, especially the dynamic range and signal to noise ratio of the images should be carefully evaluated before compressive decoding process.

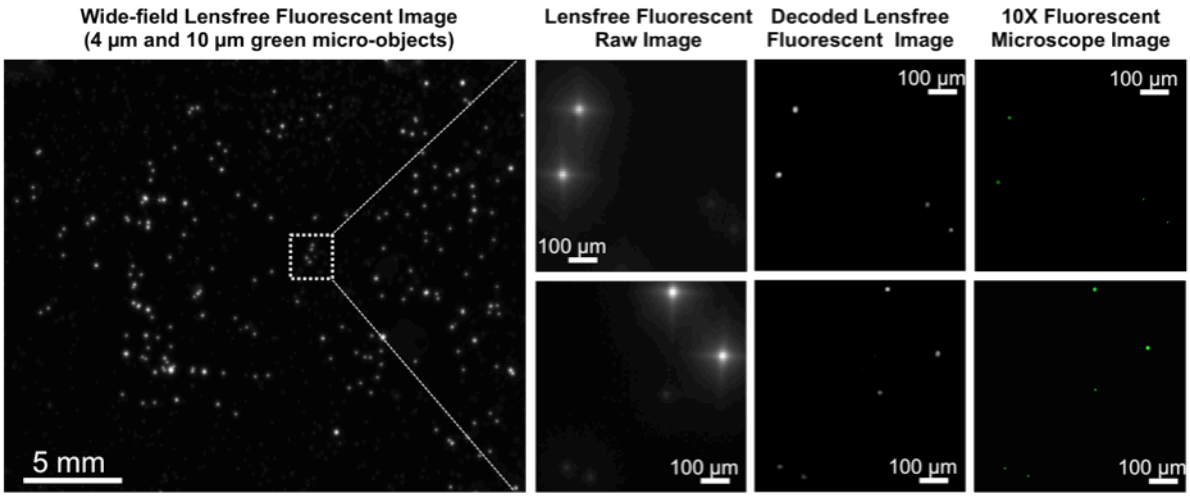

Figure 4-9 | Wide-field lensfree fluorescent on-chip imaging of a mixture containing 4 μm and 10 μm green fluorescent particles is shown. For comparison purposes, 10X microscope objective images are also provided, which agree well with my lensfree fluorescent images.

Finally, with the optimized compressive decoding and fiber-optic faceplate based imaging system, I demonstrate wide field on-chip imaging of fluorescently labeled white blood cells[13] over the entire FOV of 8 cm^2. Fig. 4-10 shows that the raw lensfree images are rapidly decoded using a CS based decoder, which agrees very well with a conventional microscope image of the same sample that is acquired with a 10X objective lens.

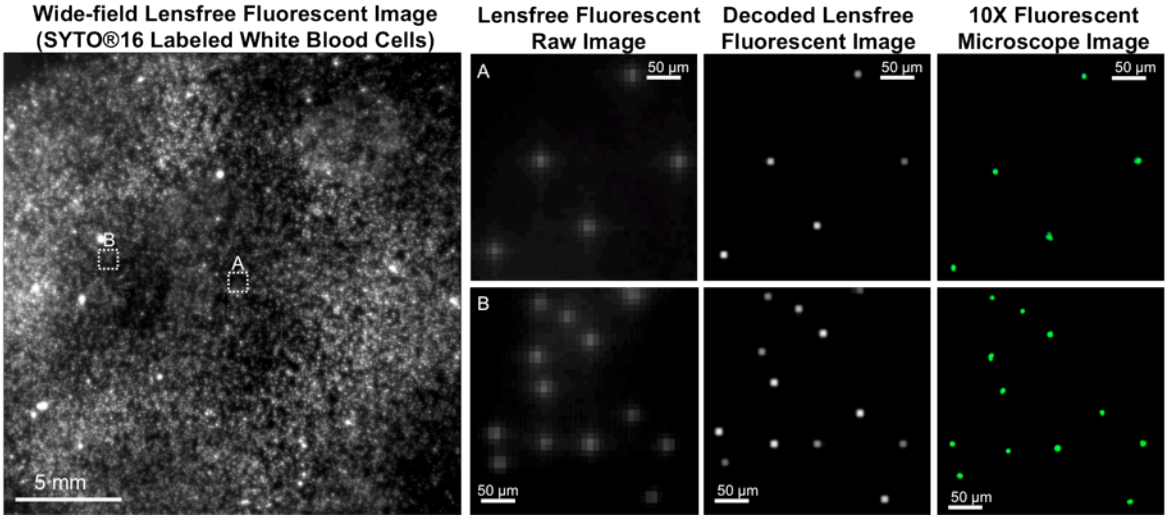

Figure 4-10 | Lensfree imaging of fluorescently (SYTO®16) labeled white blood cells is illustrated. The raw lensfree images are rapidly decoded using a CS based decoder, which agrees very well with a conventional microscope image of the same sample that is acquired with a 10X objective lens.

4.4 References

1. Epstein, J. R. & Walt, D. R. Fluorescence-based fibre optic arrays: a universal platform for sensing. Chemical Society Reviews **32,** 203 (2003).
2. Kong, D. & Wang, L. Ultrahigh-resolution fiber-optic image guides derived from microstructured polymer optical fiber preforms. Opt. Lett. **34,** 2435–2437 (2009).
3. Zhang, H., Nie, S., Etson, C. M., Wang, R. M. & Walt, D. R. Oil-sealed femtoliter fiber-optic arrays for single molecule analysis. Lab Chip **12,** 2229–2239 (2012).
4. Gmitro, A. F. & Aziz, D. Confocal microscopy through a fiber-optic imaging bundle. Opt. Lett. **18,** 565–567 (1993).
5. Ahn, S., Kulis, D. M., Erdner, D. L., Anderson, D. M. & Walt, D. R. Fiber-Optic Microarray for Simultaneous Detection of Multiple Harmful Algal Bloom Species. Appl. Environ. Microbiol. **72,** 5742–5749 (2006).
6. Ferguson, J. A., Steemers, F. J. & Walt, D. R. High-Density Fiber-Optic DNA Random Microsphere Array. Anal. Chem. **72,** 5618–5624 (2000).
7. Yuan, S. & Preza, C. Point-spread function engineering to reduce the impact of spherical aberration on 3D computational fluorescence microscopy imaging. Optics Express **19,** 23298 (2011).
8. Coskun, A. F., Su, T.-W. & Ozcan, A. Wide field-of-view lens-free fluorescent imaging on a chip. Lab Chip **10,** 824–827 (2010).
9. Coskun, A. F., Sencan, I., Su, T.-W. & Ozcan, A. Lensless wide-field fluorescent imaging on a chip using compressive decoding of sparse objects. Optics Express **18,** 10510 (2010).
10. Lucy, L. B. An iterative technique for the rectification of observed distributions. The Astronomical Journal **79,** 745 (1974).

11. RICHARDSON, W. H. Bayesian-Based Iterative Method of Image Restoration. J. Opt. Soc. Am. **62,** 55–59 (1972).

12. Biggs, D. S. C. & Andrews, M. Acceleration of iterative image restoration algorithms. Appl. Opt. **36,** 1766–1775 (1997).

13. Coskun, A. F., Su, T.-W., Sencan, I. & Ozcan, A. Lensless Fluorescent Microscopy on a Chip. Journal of Visualized Experiments, **54**, e3181 (2011).

Chapter 5 Lensfree fluorescent microscopy using tapered fiber-optic arrays

Parts of this chapter have already been published in Analyst Vol. 136, 3512–3518 (2011).

5.1 Introduction

Lensfree imaging[1–11] in general aims to replace bulky and expensive optical components with much more compact and cost-effective alternatives, and could provide a useful platform especially for microscopic analysis of microfluidic systems. In addition to the simplicity and compactness of its architecture,[7,8] lensfree imaging also provides a throughput advantage such that it permits a significantly larger imaging field-of-view (FOV). Along the same lines, in chapters 3-4, I demonstrated a lensfree fluorescent imaging platform, utilizing planar fiber-optic arrays and compressive decoding approaches, that can achieve ~10 μm resolution over >8 cm^2 FOV without the use of any lenses and mechanical scanners.[10] While its resolution is modest, such a large imaging FOV is rather valuable for high-throughput cytometry and rare cell detection applications that demand imaging of large area microfluidic channels.[12–14]

In this chapter, I discuss an improved lensfree fluorescent imaging platform[15] that can achieve <3-4 μm resolution over an FOV of ~60 mm^2 without affecting the compactness and the simplicity of the on-chip imager. In this lensfree fluorescent imaging modality, the sample chip is placed onto a tapered fiber-optic arrays (also known as fiber-optic taper or tapered fiber-optic faceplate) that has ~5 fold higher density of fiber-optic waveguides on its top facet compared to the bottom one (see Fig. 5-1). This compact taper geometry samples the fluorescent emission from the objects with a period of ~2.2 μm and achieves ~2.4 fold magnification of the lensfree fluorescent patterns over ~60 mm^2 FOV without introducing any spatial aberrations into the

lensfree imaging system. To excite the fluorescent samples located on the tapered faceplate, an incoherent source is coupled to this system through a glass hemisphere as illustrated in Fig. 5-1. After interacting with the fluorescent objects that are placed within a microfluidic channel, the pump is rejected through total internal reflection occurring at the bottom facet of the microfluidic chip (see Fig. 5-1).

With further removal of the weakly scattered excitation light by using an inexpensive absorption filter (Fig. 5-1), a sufficiently strong dark-field background is created such that the fluorescent emission from the objects can be sampled using an opto-electronic sensor-array (e.g., a charge-coupled-device—CCD). After acquisition of these raw lensfree fluorescent images, a compressive sampling based decoding algorithm[10,16–18] is then used to partially undo the effect of diffraction such that a lensfree spatial resolution of <4 μm can be achieved over the entire faceplate taper area (~60 mm^2). I should emphasize that, without a trade-off in spatial resolution, this FOV can further be increased by using larger area CCD chips within the same lensfree imaging architecture shown in Fig. 5-1.

The main function of the fiber-optic faceplate in lensfree fluorescent on-chip imaging can also be understood from the perspective of PSF engineering (see chapter 4 for details), i.e., for a given pixel size at the sensor chip, through the use of a faceplate, an optimum PSF can be created. Together with this PSF engineering, tapering of the faceplate as shown in Fig. 5-1 adds another advantage to the presented on-chip platform through image magnification such that more pixels can now detect the lensfree emission of the objects without sacrificing the detection SNR or without introducing spatial aberrations within the large imaging FOV. In this tapered faceplate based imaging geometry, the fluorescent emission of the objects is sampled with a dense grid of optical waveguides (~2.2 μm period) and is delivered to the CCD sensor with a larger grid (~5

μm period) such that the relative distances in the object plane are roughly magnified by ~2.4x. In principle, a larger magnification fiber-optic taper (up to 6-10x) could potentially be used for getting a better spatial resolution with the lensfree on-chip imaging platform (assuming that a decent SNR could also be achieved). However, as the diameter of the fiber-cores gets smaller and smaller the cross-talk among individual fiber-optic waveguides within the tapered faceplate structure would start to increase which could degrade the imaging quality of this platform, unless the refractive index of the core regions is increased to reduce this modal cross-talk. In addition to these, another valuable function of the tapered fiber-optic faceplate in lensfree on-chip fluorescent imaging is thermal isolation of the objects from the sensor chip and the reader circuit such that operating temperatures within the sample micro-channel can be better controlled.

This compact lensfree fluorescent on-chip imager, utilizing tapered fiber-optic arrays and compressive decoding, with a decent spatial resolution and an ultra-wide FOV could especially be valuable for high-throughput cytometry and rare cell analysis involving large area microfluidic systems, as well as for small animal imaging applications.

5.2 Materials and methods

Design of the wide-field lensfree fluorescent microscopy platform using a tapered fiber-optic faceplate: The lensfree on-chip fluorescent microscopy platform is built on an 11 MPixel CCD sensor chip (KODAK, KAI-11002, 9 μm pixel size), which was operated at room temperature. A thin absorption filter with dyes is fabricated by coating 30 μm thick glass substrates. This fabrication process starts with dissolving Orasol dyes in cyclopentanone solvent and adding KMPR 1005 Photoresist (~0.4 g mL^{-1} dye concentration), after which the excess dye material in the mixture is removed using a 0.45 μm diameter porous filter. The raw solution is then processed by spin coating for 20 s at 2000 rpm, baking for 300 s at 100 °C, flood exposure

at 13 mW cm^{-2} for 35 s, and finally baking for another 120 s at 100 °C. One of these fabricated filters is gently placed on the sensor array with a vacuum pen. Then the tapered fiber-optic faceplate (Edmund Optics, NT55-134, numerical aperture: 1.0, size ratio: 18:8 mm) is placed onto this absorption filter, with the large facet facing the sensor chip as shown in Fig. 5-1. A 3D printer is used to create a customized housing to cover the optical components, except the top facet of the taper (see Fig. 5-1b). Blocking unwanted light is important to decrease the leakage from excitation or ambient light, which can decrease the image contrast otherwise. As for the excitation, the illumination was provided by a xenon lamp coupled to a monochromator such that the center wavelength was chosen as 580 nm with ~15 nm bandwidth. The illumination angle was adjusted by using a multi-mode fiber-optic cable attached to a mechanical holder, so that total-internal reflection can be satisfied over the entire imaging area (~60 mm^2). The fluorescent samples are then placed onto the smaller facet of the tapered faceplate. And finally, a glass hemisphere is assembled to couple the excitation light to the samples using an index-matching gel (see Fig. 5-1). The lensfree fluorescent images are then recorded using a custom developed Labview interface, typically within 2–3 seconds of exposure time.

Fluorescent bead sample preparation: Fluorescent beads with 4 μm and 2 μm diameters (red beads: excitation 580 nm/emission 605 nm) were purchased from Invitrogen (Carlsbad, CA). The stock solution is diluted 4000 times with DI water in small aliquots. Then using a micropipette, the bead solution (~10 μL) is transferred onto a disposable glass substrate (thickness: ~30 to 100 μm) and is sandwiched using another glass substrate before being imaged using this lensfree on-chip microscope.

Waterborne Cyst labeling: Giardia muris cysts were purchased from Waterborne Inc. (New Orleans, LA, USA). The stock solution of these cysts has a concentration of ~5×10^6 parasites

mL^{-1}. To avoid the dynamic motion of the parasites, they were fixed in 5% formalin/PBS at pH 7.4/0.01% Tween-20. A small amount of this solution (e.g. 100–200 µL) was centrifuged and

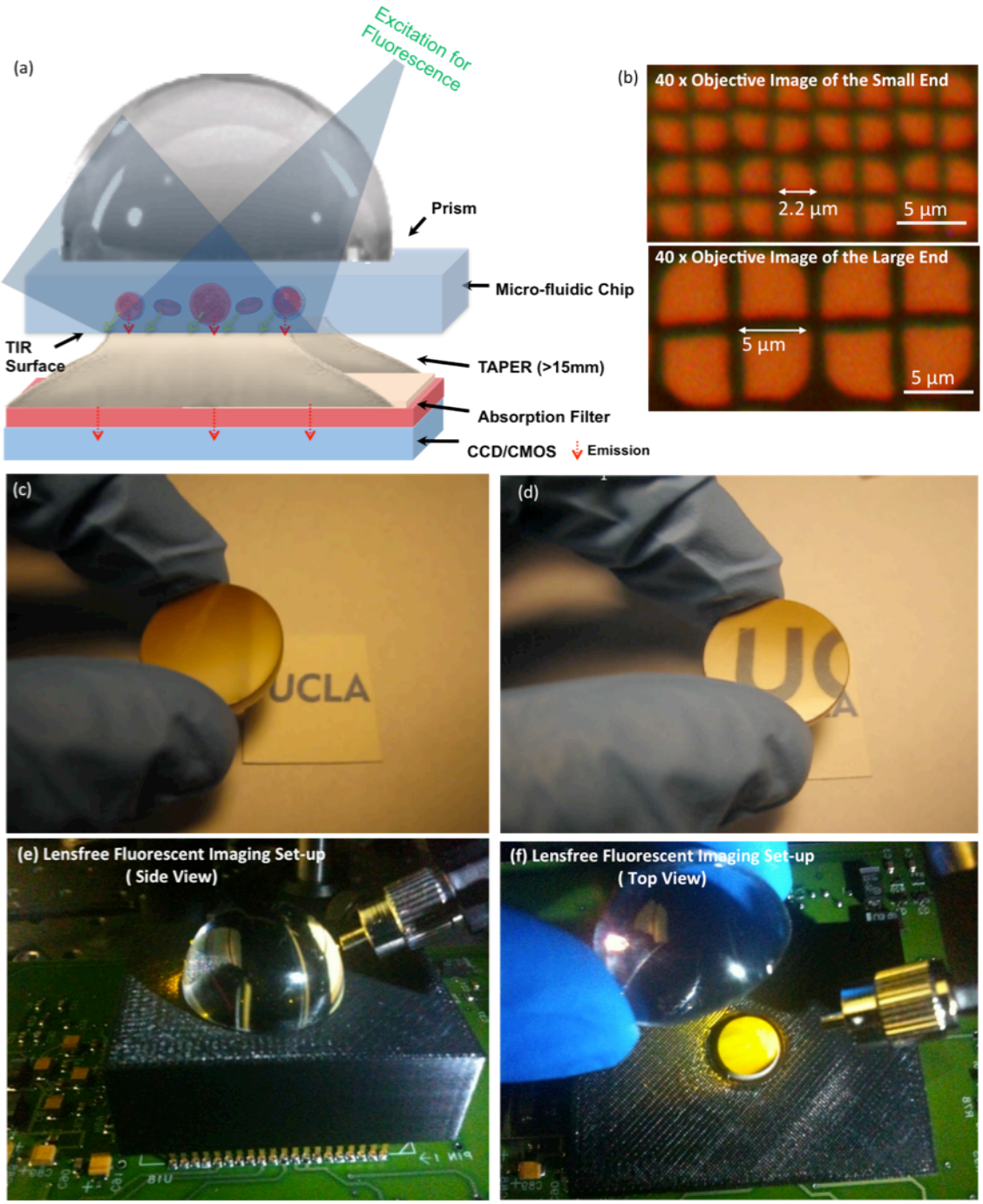

Figure 5-1 | (a) The schematic diagram of the lensfree fluorescent on-chip imaging platform is illustrated. (b) Microscopic images of the top and bottom facets of the fiber-optic taper are shown. (c and d) The UCLA image is shown without and with the tapered fiber-optic faceplate, demonstrating the image magnification function of the fiber-optic taper, respectively. (e and f) Pictures of the experimental set-up are shown.

re-suspended in the form of PBS suspension. As for the labeling dye , 1 mM SYTO®64 nucleic acid dye was used with the mixing ratio of 5 μL of dye and 100 μL parasite-consisting suspensions. Once prepared, this mixture was incubated in dark environment for ~30 min. Just after activation of dye labeling within the parasite body (emission peak wavelength: 619 nm), the unbound dyes (which might potentially introduce unwanted background) were removed by another centrifuging and re-suspension in PBS. The final sample solution was then placed between two glass slides for wide-field lensfree imaging on a chip.

Compressive sampling based decoding of raw lensfree fluorescent images: I made use of compressive sampling based decoding to partially undo the effect of diffraction, which is an inherent result of lensfree on-chip operation. In this method, I first measure the point-spread-function of the lensfreee imaging system using small fluorescent particles (e.g., ~2 μm diameter). For this end, several lensfree fluorescent spots of isolated particles are aligned with respect to each other and are then averaged to yield the lensfree fluorescent point-spread-function of the platform. Based on this, for any arbitrary distribution of fluorescent point sources at the object plane, one can calculate the expected lensfree fluorescent pattern that is to be sampled at the detector plane. I should note that I can also measure the individual point-spread functions corresponding to different vertical layers, and use this information to calculate the expected lensfree fluorescent pattern at the detector array for e.g., a 3D stack of fluorescent objects.

To decode a given lensfree fluorescent image (whether from a single layer or multiple vertical layers), I iteratively minimize (using truncated Newton interior-point method[19]) a cost function that is defined by l_1-regularized least square error between the calculated (i.e., expected) lensfree fluorescent pattern and the measured one at the detector array.[10] This entire optimization process is based on sparsity of the fluorescent distribution at the object plane and it typically

converges after ~40 to 60 iterations taking ~0.5 to 2 minutes for e.g., the regions of interest shown in Fig 5-3 using a 3.2 GHz processor (Intel Core(™) i5 CPU 650). As a result of this compressive decoding process, the resolving power of the lensfree imaging platform significantly increases achieving <4 μm resolution over a wide field-of-view of ~60 mm^2.

Pseudocoloring of reconstructed images: While not a fundamental limitation, the presented on-chip imaging platform mostly employs monochrome opto-electronic sensor arrays which in general provide better signal-to-noise ratio for biological sample imaging. Therefore, the raw fluorescent images are acquired in grayscale format, which does not contain the real color information of the samples. This could be mitigated by using color CCD/CMOS chips in this lensfree imaging architecture such that 3 color channels (red, green and blue) are acquired in each lensfree fluorescent measurement. On the other hand, if the labeling dye emission characteristics are already known, raw format grayscale fluorescent images of a monochrome sensor-chip and their decoded versions can also be artificially converted to color images using a pseudocoloring algorithm implemented in e.g., MATLAB. For this purpose, the acquired grayscale images can be expanded into 3- dimensional data-cubes, where any color of interest can be synthesized by using appropriate weighing factors at each pseudo channel of the data cube. As a result of this processing, monochrome lensfree fluorescent images can be converted to multi-channel images that provide known color information of a given fluorescent object.

5.3 Results and discussion

The presented lensfree on-chip microscopy platform is composed of a CCD sensor chip, a thin absorption filter, a tapered fiber-optic faceplate and a glass hemisphere (see Fig. 5-1). I tested the performance of this on-chip microscopy platform by imaging 4 and 2 μm diameter fluorescent particles as well as Giardia muris cysts. In Fig. 5-2, an imaging FOV of ~60 mm^2 is

illustrated, with three digitally zoomed sections showing the raw lensfree signatures of the fluorescent particles. These raw fluorescent images reflect the lensfree signal detected at the CCD chip, and are then decoded using a compressive sampling (CS) algorithm[10] to yield images of the object plane with improved spatial resolution as demonstrated in Fig. 5-2 (refer to the Experimental Methods Section for further details). The same figure also shows 10X microscope - objective (0.25 Numerical Aperture—NA) images of the same objects for comparison purposes, which very well agree with my lensfree imaging results.

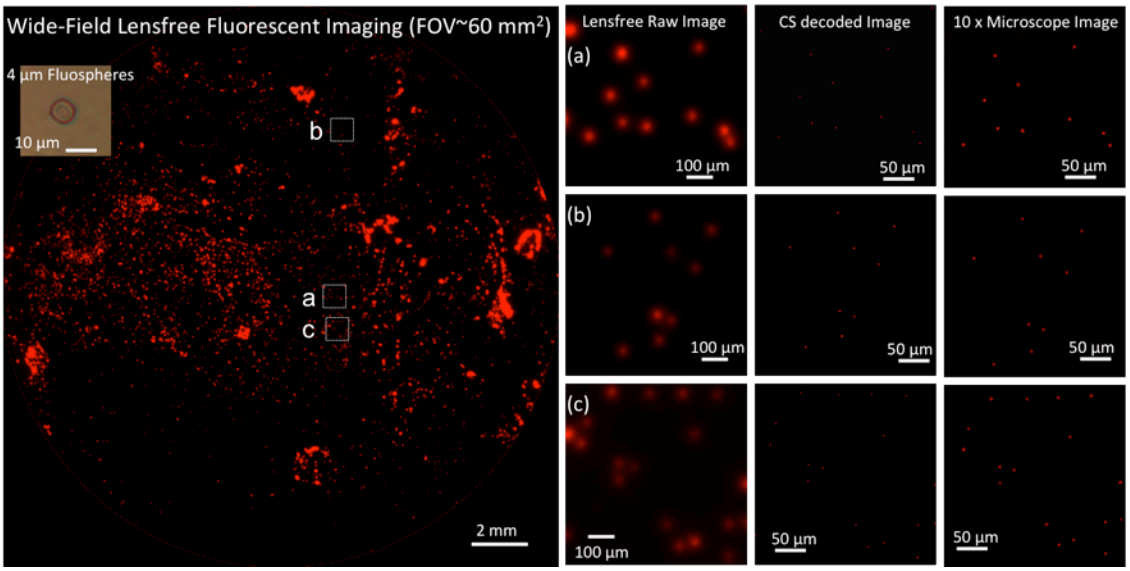

Figure 5-2 | (Left) the entire imaging FOV (~60 mm^2) of the lensfree fluorescent microscope shown in Fig. 5-1 is illustrated. (a–c) Three different zoomed sections of the lensfree fluorescent image are shown. The middle column in (a–c) illustrates the compressive sampling (CS) decoder results, whereas the right column shows (for comparison purposes) images of the same microparticles (4 µm diameter) using a conventional lens-based fluorescent microscope (10× objective lens, NA = 0.25). The CS decoder uses the raw lensfree fluorescent images which are shown in the left column of (a–c). The images are pseudo-colored in red.

To quantify the spatial resolution, in Figs. 5-3 and 5-4 I focus on smaller regions of interest where the fluorescent particles (4 and 2 µm diameter) were close to each other. Figs. 5-3 and Fig. 5-4 also illustrate bright-field microscope images of these fluorescent particles which act as my references in terms of the distances (d) between particles. I also show in these figures the raw lensfree fluorescent images (which are pixelated) for the same particles as well as their CS

decoded versions to validate the spatial resolution. Note that unlike conventional lens-based microscopy , objects separated by <15 µm partially overlap with each other at the detector plane due to unavoidable diffraction occurring in this lensfree platform. My CS decoding results shown in Figs. 5-3 and 5-4 demonstrate that I can resolve closely spaced fluorescent particles from each other, achieving a lensfree spatial resolution of <4 µm. Considering that the pixel size at the CCD chip of this lensfree on-chip imager is 9 µm, a resolution of <4 µm is quite significant.

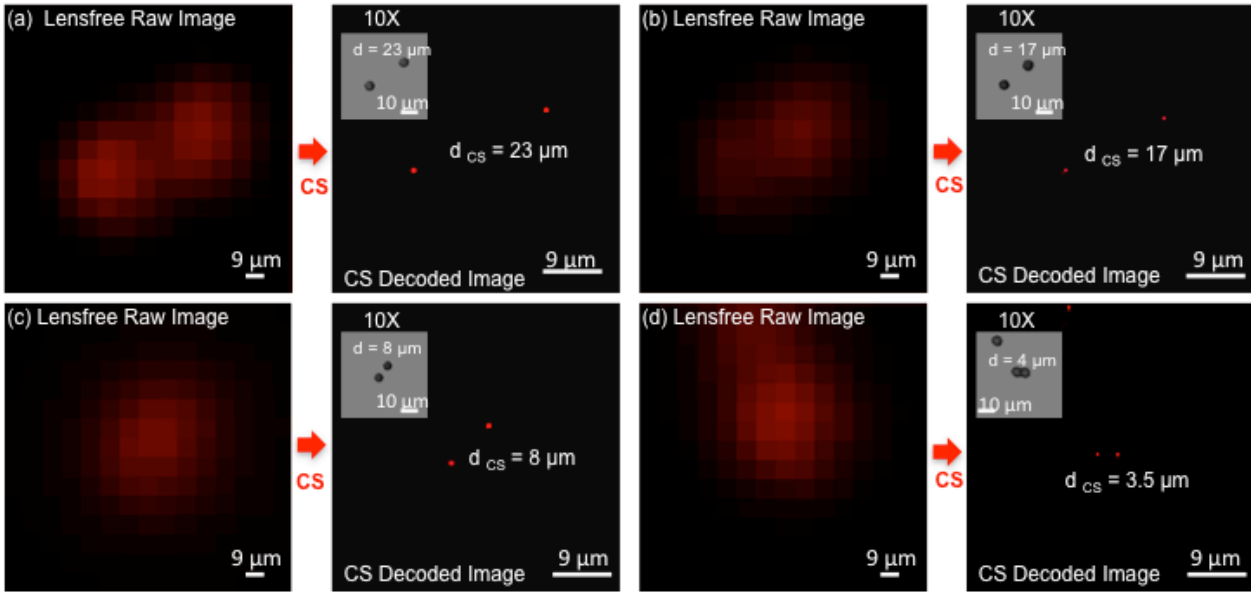

Figure 5-3 | Resolution of the lensfree fluorescent on-chip microscope is quantified using 4 µm diameter particles. The pixelated raw lensfree fluorescent images are decoded using a compressive sampling (CS) algorithm to resolve the overlapping lensfree fluorescent emission patterns arising from the particles. The inset images in each decoded image illustrate (for comparison purposes) bright-field microscope images of the same microparticles. Note that because the samples were sequentially imaged using the microscope after their lensfree images were acquired, their relative orientations might be slightly rotated/shifted between the two imaging modalities. The lensfree images are pseudo-colored in red.

I have also validated the performance of this lensfree fluorescent microscopy platform by imaging labeled Giardia muris cysts as illustrated in Fig. 5-5. When combined with its large FOV within a compact on-chip platform, these results could be especially important for rapid screening of water-borne parasites in field settings.

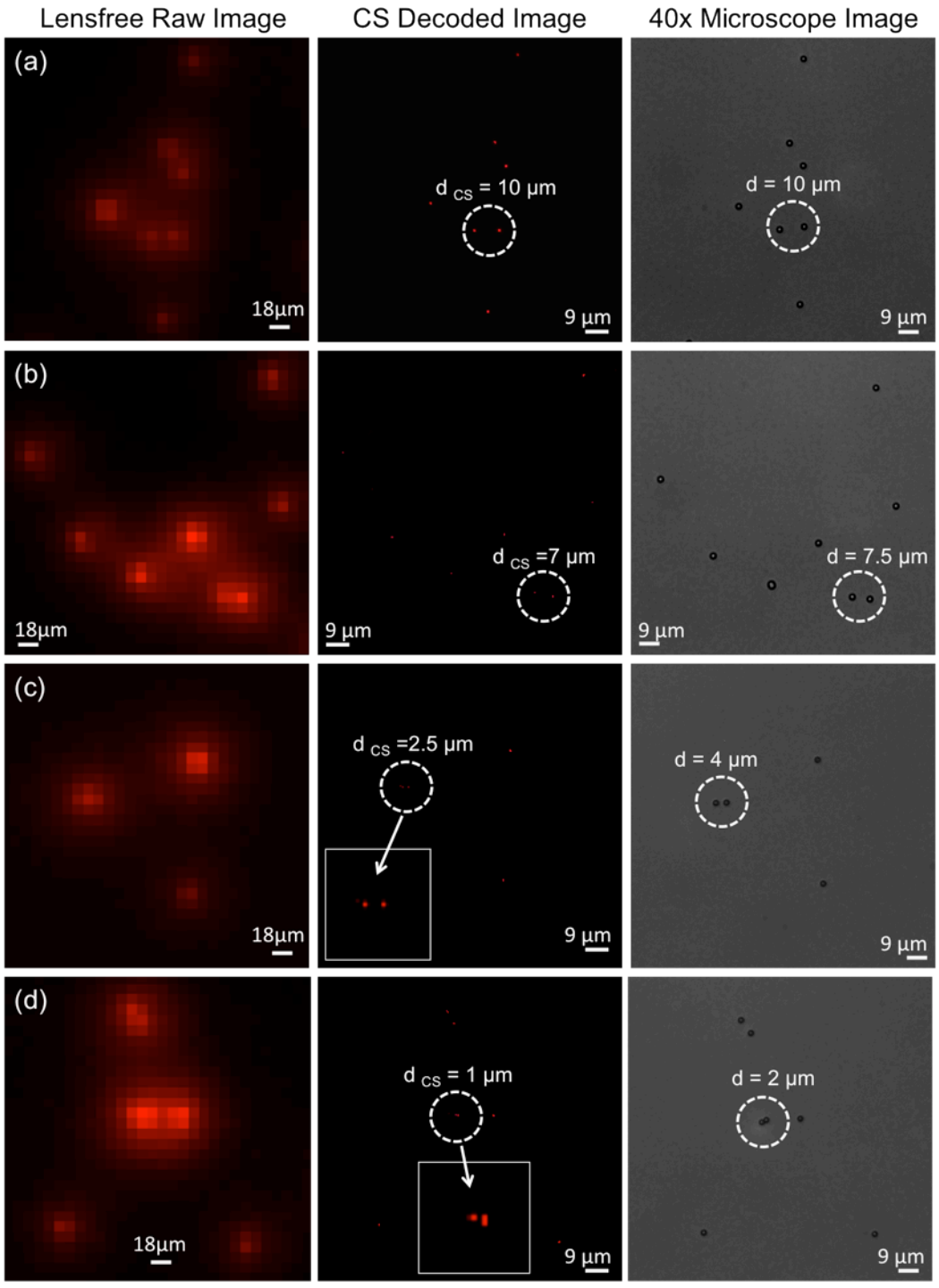

Figure 5-4 | Resolution of the lensfree fluorescent on-chip microscope is quantified using 2 µm diameter particles. The pixelated raw lensfree fluorescent images are decoded using a CS algorithm to resolve the overlapping lensfree fluorescent emission patterns arising from the particles. For comparison purposes conventional bright-field microscope images of the same 2 µm diameter particles are also shown on the right column. Note that because the samples were sequentially imaged using the microscope after their lensfree images were acquired, their relative orientations might be slightly rotated/shifted between the two imaging modalities. The lensfree images are pseudo-colored in red.

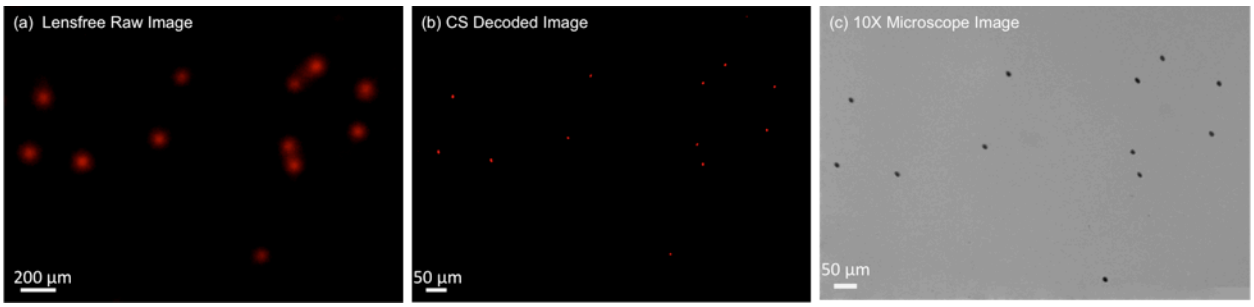

Figure 5-5 | Lensfree fluorescent imaging results for Giardia muris cysts are shown. A conventional microscope image of the same FOV is also illustrated in (c). Note that because the samples were sequentially imaged using the microscope after their lensfree images were acquired, their relative orientations might be slightly rotated/shifted between the two imaging modalities. The lensfree images are pseudo-colored in red.

In this platform, while the magnification created through the use of a tapered fiber-optic faceplate is an important parameter for spatial resolution, there are other factors that significantly affect the achievable resolution in this platform:

Detection signal-to-noise ratio (SNR): This parameter is governed by several factors, ranging from noise floor of the sensor, faceplate-to-sensor and object-to-faceplate distances, the numerical aperture of the faceplate, as well as the emission intensity of the objects and the strength of the dark-field background. In principle, if the SNR of the raw fluorescent images is very high, the resolution of the compressively decoded images can become independent of the magnification of the faceplate taper, and can in theory approach sub-micron levels. Therefore, active cooling of the opto-electronic sensor array is an important route that I can utilize to further improve the lensfree resolution without a trade-off in this imaging FOV. The fact that the thickness of the faceplate is >1–2 cm can also thermally isolate the samples from the sensor chip, helping to implement active cooling of the sensor without a damage to the samples. Such an increased digital SNR would also increase the detection numerical aperture of this platform, such that more of the oblique fluorescent rays can now be detected above the noise floor of the sensor. Therefore under improved SNR levels, the detection numerical aperture will be ultimately

limited by the numerical aperture of the fiber-optic faceplate, which in my experimental set-up was ~1.

Other key parameters that set the detection SNR are the faceplate-to-sensor and object-to-faceplate distances. The object-to-faceplate vertical distance can be reduced to ~10 to 20 μm. However, the faceplate-to-sensor vertical distance will have to be limited with the thickness of the absorption filter which can get as small as ~20 to 30 μm (see Fig. 5-1). One other key parameter that will directly determine the detection SNR in this lensfree imaging geometry is the fluorescent emission intensity of the samples (compared to the background) which is mostly determined by the quantum efficiency of labeling dyes, excitation power and wavelength, as well as the labeling efficiency of the sample.

Therefore, governed by the above discussed parameters, the digital SNR of the lensfree images is one of the most important factors that influence the spatial resolution of the fluorescent on-chip imager, which can potentially achieve sub-micron resolution by additional systematic improvements in this optical set-up.

Lensfree point-spread function (PSF): I define the lensfree PSF of this on-chip imaging system as the 2D spatial function that represents the fluorescent emission pattern of a point source located at the object plane, before being sampled by the sensor chip at the detector plane. As for the discussion of the system PSF and its effect on spatial resolution one has to be careful. Under a strong detection SNR and a large pixel size at the sensor chip (as I typically employ, e.g., ~9 μm), the narrowest lensfree PSF is not necessarily the best route for improving CS decoded resolution. To better understand this argument, assume that the spatial width of the lensfree PSF is hypothetically made smaller than the large pixel size at the sensor chip. In this case, two fluorescent points that are close to each other at the sub-pixel level would both contribute to a

single pixel, which makes it impossible to resolve them no matter what type of digital decoder is used. Simply put, infinitely many different combinations of these two point sources within the same pixel would yield the same signal, making decoding at the sub-pixel level physically impossible.

However, for the same pixel size and digital SNR at the sensor chip, if this time the width of the lensfree PSF is increased (which could be achieved by e.g., slightly increasing the vertical distance of the object plane from the sensor surface), then decoding of these sub-pixel separated objects would be feasible since several different pixels (dictated by the practical width of the PSF) can now detect weighted sums of these two closely spaced point sources. This conclusion is true as long as the detection SNR does not degrade significantly (getting close to the noise floor of the sensor) due to spatial broadening.

In other words, for a given large pixel size at the sensor chip, after a certain PSF width is reached, a further increase in its width might start to practically reduce the detection SNR due to signal spreading, and this would set the boundary for the optimum PSF, which is entirely dictated by the pixel size at the sensor chip and the noise performance of lensfree platform. Note also that since I am employing a compressive decoder, defining an optimum PSF width for a given pixel size based on the classical Nyquist sampling theorem would also be misleading, especially for spatially sparse fluorescent objects. More formal treatment of this topic is provided in ref. 10, through mathematical analysis of compressive sampling and its relationship to lensfree on-chip fluorescent imaging.

I believe that such a compact and light-weight lensfree fluorescent microscopy platform (Fig. 5-1), with rapid compressive decoding algorithms behind it, could be quite useful for high-throughput screening applications, rare cell analysis and for microarray imaging applications.

5.4 References

1. Haddad, W. S. et al. Fourier-transform holographic microscope. Appl. Opt. **31,** 4973–4978 (1992).
2. Xu, W., Jericho, M. H., Meinertzhagen, I. A. & Kreuzer, H. J. Digital in-line holography for biological applications. PNAS **98,** 11301–11305 (2001).
3. Pedrini, G. & Tiziani, H. J. Short-Coherence Digital Microscopy by Use of a Lensless Holographic Imaging System. Appl. Opt. **41,** 4489–4496 (2002).
4. Repetto, L., Piano, E. & Pontiggia, C. Lensless digital holographic microscope with light-emitting diode illumination. Opt. Lett. **29,** 1132–1134 (2004).
5. Greenbaum, A. et al. Imaging without lenses: achievements and remaining challenges of wide-field on-chip microscopy. Nature Methods **9,** 889–895 (2012).
6. Mudanyali, O. et al. Wide-field optical detection of nanoparticles using on-chip microscopy and self-assembled nanolenses. Nature Photonics (2013). doi:10.1038/nphoton.2012.337
7. Mudanyali, O. et al. Compact, light-weight and cost-effective microscope based on lensless incoherent holography for telemedicine applications. Lab Chip **10,** 1417–1428 (2010).
8. Tseng, D. et al. Lensfree microscopy on a cellphone. Lab Chip **10,** 1787–1792 (2010).
9. Coskun, A. F., Su, T.-W. & Ozcan, A. Wide field-of-view lens-free fluorescent imaging on a chip. Lab Chip **10,** 824–827 (2010).
10. Coskun, A. F., Sencan, I., Su, T.-W. & Ozcan, A. Lensless wide-field fluorescent imaging on a chip using compressive decoding of sparse objects. Optics Express **18,** 10510 (2010).
11. Coskun, A. F., Su, T.-W., Sencan, I. & Ozcan, A. Lensless Fluorescent Microscopy on a Chip. Journal of Visualized Experiments, **54**, e3181 (2011).

12. Nagrath, S. et al. Isolation of rare circulating tumour cells in cancer patients by microchip technology. Nature **450,** 1235–1239 (2007).

13. Stott, S. L. et al. Isolation of circulating tumor cells using a microvortex-generating herringbone-chip. PNAS **107,** 18392–18397 (2010).

14. Murthy, S. K., Sin, A., Tompkins, R. G. & Toner, M. Effect of Flow and Surface Conditions on Human Lymphocyte Isolation Using Microfluidic Chambers. Langmuir **20,** 11649–11655 (2004).

15. Coskun, A. F., Sencan, I., Su, T.-W. & Ozcan, A. Wide-field lensless fluorescent microscopy using a tapered fiber-optic faceplate on a chip. Analyst **136,** 3512–3518 (2011).

16. Candes, E. J. & Tao, T. Near-Optimal Signal Recovery From Random Projections: Universal Encoding Strategies? IEEE Transactions on Information Theory **52,** 5406 –5425 (2006).

17. Candes, E. J., Romberg, J. & Tao, T. Robust uncertainty principles: exact signal reconstruction from highly incomplete frequency information. IEEE Transactions on Information Theory **52,** 489 – 509 (2006).

18. Candès, E. J., Romberg, J. K. & Tao, T. Stable signal recovery from incomplete and inaccurate measurements. Communications on Pure and Applied Mathematics **59,** 1207–1223 (2006).

19. Kim, S.-J., Koh, K., Lustig, M., Boyd, S. & Gorinevsky, D. An Interior-Point Method for Large-Scale l1-Regularized Least Squares. IEEE Journal of Selected Topics in Signal Processing **1,** 606 –617 (2007).

Chapter 6 On-chip fluorescent microscopy of transgenic Caenorhabditis Elegans

Parts of this chapter have already been published in PLoS ONE Vol. 6, e15955 (2011).

6.1 Introduction

C. elegans is an important model organism that has been widely studied in various fields such as genetics[1], oncology[2] and neurobiology[3]. Wide-field optical imaging of C. elegans is an essential need for all these fields to enable high-throughput screening of this model organism. While several high-throughput imaging platforms have been successfully demonstrated so far[4–13],the main stream for this application involves the use of lens-based conventional optical microscopes which can only provide a limited field-of-view (FOV) of e.g., $\leq$1mm^2, and therefore require mechanical scanning to provide a larger imaging FOV. In addition to this, such conventional optical microscopy platforms are rather bulky, and do not provide a decent match in terms of compactness to micro-fluidic technologies that are becoming widely used today in high-throughput screening of C. elegans.

To provide an alternative solution to this imaging need, here I demonstrate ultra-wide field fluorescent imaging of transgenic C. elegans over an FOV of >2–8 cm^2 with a spatial resolution of ~10 μm. This platform relies on lensfree on-chip imaging which, broadly defined, is becoming an important substitute for conventional microscopes especially for high-throughput imaging applications[14–21]. In the on-chip fluorescent imaging platform (see Fig. 6-1), transgenic C. elegans samples are excited through a prism interface where the excitation light is rejected based on total internal reflection (TIR) that is occurring at the bottom facet of the glass substrate. The emitted fluorescent signal from the body of the worm does not entirely obey TIR and therefore

can be detected by a wide-field opto-electronic sensor-array e.g., a charge-coupled-device (CCD) without the use of any lenses. This detection process occurs through a wide angular range (corresponding to numerical aperture of ~1.0) and because the fluorescent emission from the sample is not directional, the point-spread-function of such a lensfree fluorescent imaging platform will be rather broad, which will significantly limit the achievable raw spatial resolution. To combat this problem of lensfree imaging, I demonstrated the use of a deconvolution approach (namely the Lucy-Richardson algorithm[22–24]) to achieve ~40–50μm resolution as described in chapter 2 and a compressive sensing based reconstruction approach to achieve down to < 4 μm spatial resolution as discussed in chapters 3-5.

For this end, in this manuscript I demonstrate the use of the compressive sampling[25–27] based reconstruction algorithm for lensfree on-chip imaging of transgenic C. elegans samples with a spatial resolution of ~10 μm over the entire FOV of >2–8 cm^2. In this approach, transgenic C. elegans samples by definition satisfy the sparsity constraint of compressive sampling, and therefore can be efficiently decoded by using various compressive decoders that have been developed recently.[28–30] **Our results constitute the first time that a lensfree on-chip platform has successfully imaged fluorescent C. elegans samples.**

In addition to wide-field fluorescent imaging, I also demonstrate that the same lensfree on-chip platform can also conduct bright-field transmission imaging of C. elegans samples using partially coherent digital in-line holography[18,19], which is coupled to the same platform through the top facet of the prism as illustrated in Fig. 6-1. I believe that such ultra-wide field dual-mode imaging of C. elegans on a chip might provide a useful high-throughput tool for biomedical research in various fields including genetics, oncology and neurobiology.

6.2 Materials and methods

Design of the fluorescent and holographic lensfree on-chip imaging system: The lensfree imaging system utilizes a rhomboid prism to achieve fluorescence excitation through its side facet as shown in Fig. 6-1. After interacting with the entire body of the worm, pump photons are rejected by TIR occurring at the bottom glass substrate. To create a sufficient dark-field background, the weakly scattered pump photons that do not obey TIR are also rejected by an additional absorption filter (see Fig. 6-1), as a result of which only the fluorescent emission from the objects is detected by the opto-electronic sensor-array.

Note that unlike conventional lens-based fluorescent microscopy, the use of thin-film interference filters in this platform is not trivial since rejection of pump photons in a lensfree imaging configuration would require deposition of much thicker interference films to block a large angular range of pump photons. This not only increases the cost but also requires the use of considerably thick substrates due to higher stress in the thicker film, which significantly weakens the SNR of the fluorescent PSF, also degrading the achievable resolution. Therefore, I avoided using such interference based fluorescent filters, and instead, fabricated absorption based filters that have dyes coated on ultra-thin glass substrates (~30 μm).

The fabrication recipe of these thin absorption filters includes dissolving Orasol dyes in a small volume of cyclopentanone and then adding KMPR 1005 Photoresist (~0.4 g ml^{-1} dye concentration), after which excess dye material was removed using a 0.45μm diameter mechanical filter[31]. This step is followed by spin coating for 20 s at 2000 rpm, baking for 300 s at 100°C, flood exposure at 13 mW/cm^2 for 35 s, and finally baking for another 120 s at 100°C. Based on this recipe, I fabricated different long pass absorption filters with cut-off wavelengths of 510nm, 540 nm and 600 nm by using various types of Orasol dyes, including Yellow 2RLN, Orange G, and Red BL, respectively. The rejection ratio (~30–40 dB) of these fabricated

absorption filters is sufficiently large to create the necessary dark-field background (together with TIR), making them rather useful in lensfree fluorescent on-chip imaging applications.

Once fabricated, these absorption filters (total thickness ~40 μm; 10 μm filter+30 μm glass substrate) were placed directly on the top of the active region of the CCD sensor, acting also as a protector layer for the bare sensor surface. An additional disposable ultra-thin glass substrate (~30 μm thick) was also used between the sample and the absorption filter.

As for the excitation, an incoherent light source was used, which was coupled from a Xenon lamp spectrally tuned to ~580 nm (with 15 nm bandwidth) through a monochromator (MS260i, Newport). During my experiments, the total power of excitation was kept at ~1.0–1.5 mW for an FOV of >2 cm^2.

In addition to lensfree fluorescent imaging, the same on-chip platform shown in Fig. 6-1 also permits lensfree holographic imaging[18,19] of the same samples through the top facet of the same prism that is used in fluorescent excitation. This vertical illumination is achieved by an incoherent source (i.e. an LED, 632 nm peak, and ~20 nm bandwidth) that is spatially filtered with a pinhole (~0.05–0.1 mm) to achieve holographic transmission imaging within the same on-chip platform.

Finally, I would like to also mention that all the sensors that I used in this work were monochrome. To show color images of fluorescent objects, a custom developed pseudocoloring algorithm was used in Matlab to edit the presented images.

C. elegans sample preparation: Transgenic C. elegans used in this work is widely studied to better understand the connections between muscle cells and related motor neurons[32]. For this end, UNC 122 gene is co-injected into the worms with a phenotypic marker (mCherry; emission wavelength: 610 nm).

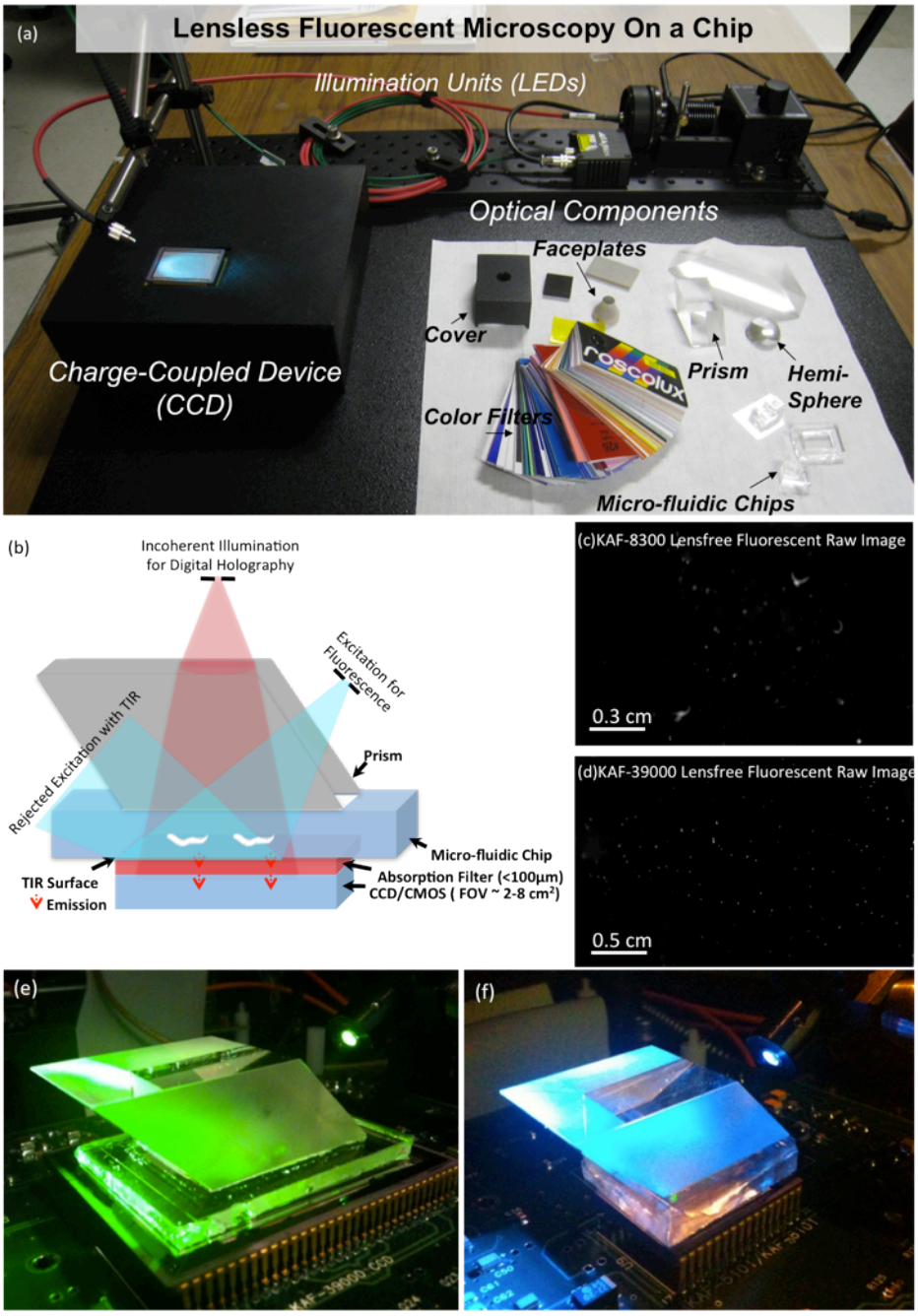

Figure 6-1 | (a) An overview of the lensfree fluorescent microscopy system is demonstrated, combining illumination, optical assembly and detection at the same platform. (b) Schematic diagram of lensfree on-chip fluorescent and holographic imaging platform is shown. Fluorescent excitation is achieved through the side facet of a rhomboid prism using an incoherent source (i.e. spectrally filtered Xenon lamp); and holographic illumination is achieved through the top facet of the same prism using an LED (632 nm peak, and ~20 nm bandwidth). (c) Lensfree fluorescent imaging is demonstrated over >2 cm^2 using KAF-8300 sensor (Full Frame CCD with a pixel size of 5.4 μm). (d) On-chip lensfree fluorescent imaging is illustrated over >8cm^2 using KAF-39000 sensor (Full Frame CCD with a pixel size of 6.8 μm). (e-f) shows the experimental set-ups of lensfree fluorescent imaging platform built on KAF-39000 and KAF-8300 sensors, respectively. Note that the excitation source in both of these set-ups is tunable, and therefore various fluorescent dyes could potentially be used without an issue.

For preparation of these transgenic C. elegans samples toward on-chip imaging, a small chunk of nematode growth medium (NGM) was extracted from the culturing plate with a sterilized tool. This specimen was dissolved in a paralyzing medium (~200 μL) that was prepared with 10mM of Levamisole[33]. To detach the worms from the gel medium, the aliquot is gently vortexed and centrifuged. By using a pipette, transgenic worms are then transferred to the substrates for lensfree on-chip imaging.

I used an immobilization reagent, i.e. Levamisole, to avoid hazy images, which also enabled me to capture comparison images of the same samples using a conventional fluorescent microscope. Note also that to avoid physical damage to adult worms, mechanical spacers such as non-fluorescent particles (~50–100 μm diameter) were also used in my imaging experiments.

Compressive decoding of lensfree fluorescent images: As illustrated in Figs. 6-2 to 6-6, compressive decoding enables accurate reconstruction of the fluorescent distribution at the object plane based on the measured PSF of this lensfree imaging platform, achieving a spatial resolution of e.g., ~10 μm over >2–8cm^2 FOV. This numerical recipe relies on compressive sampling theory[25,26,29] which presents a new method to reconstruct a sparse signal from its under-sampled representation. Wide-field fluorescent imaging of C. elegans samples on a chip by definition brings sparsity to the imaging problem since most of the FOV is already dark (i.e., non-fluorescent). Based on this connection to compressive sampling theory, lensfree raw fluorescent images can be rapidly decoded (using the measured fluorescent PSF) to significantly improve the resolving power of this platform as demonstrated in Figs. 6-2 to 6-6.

This compressive decoding process can be formalized as an l_1-regularized least square problem[28], such that:

$$\hat{\imath} = \mathrm{argmin}\|F_{det} - P_{conv} \cdot \bar{\imath}\|_2 + \alpha \cdot \|\bar{\imath}\|_1 \qquad (7.1)$$

where F_{det} is the detected raw fluorescent image at the sensor-array; P_{conv} represents the 2D convolution matrix based on the fluorescent PSF of the system; is the fluorescent source distribution that creates the lensfree image at the detector plane; α is a non-negative regularization parameter; and $\|\overline{X}\|_p$ represents the l_p norm of vector $\overline{X}$. The optimization algorithm used in this work is based on truncated Newton interior-point method[28] which rapidly converges to a sparse fluorescent solution (î) based on Eq. (7.1).[15]

6.3 Results and discussion

I imaged transgenic C. elegans samples (refer to the Methods Section for details) over a wide FOV using the same lensfree configuration depicted in Fig. 6-1. The results of these imaging experiments are summarized in Figs. 6-3 and 6-4 which also provide conventional fluorescent microscope images of the same samples for comparison purposes. As shown in these figures, raw lensfree fluorescent signatures of the worms are highly blurred due to the broad PSFs. However, using the measured PSF of each platform, these lensfree signatures can be compressively decoded to digitally yield much higher resolution images of the fluorescent regions located within the C. elegans body, which very well agree with the images obtained using a regular lens-based fluorescent microscope (see Figs. 6-3 and 6-4). These experimental results successfully demonstrate the efficacy of the compressive decoding approach to image transgenic C. elegans samples using lensfree fluorescent on-chip imaging over an ultra-wide FOV that covers the entire active area of the CCD chip (e.g., >2–8 cm^2).

I should also note that, the presented on-chip microscopy platform could potentially achieve multi-color imaging of biological samples labeled with multiple distinct targets. In these reported experiments, monochrome CCD chips were used to achieve single color lensfree fluorescent imaging; however, the use of e.g., RGB CCD chips could be utilized to image multiple colors.

Unlike conventional lens-based fluorescent microscopy the use of an RGB sensor chip does not immediately bring color imaging capability since without the use of any lenses, all the colors mix with each other at the sensor plane due to unavoidable diffraction. Therefore, lensfree fluorescent imaging might require a more sophisticated compressive decoder to enable separation of multiple colors using raw format RGB images, which was not at the focus of this work.

In addition to fluorescent imaging, the lensfree on-chip platform also permits holographic transmission imaging[18,19] of the worms using the top interface of the same prism that is used in fluorescent excitation (see Fig. 6-1). In this lensfree holographic imaging approach, a spatially incoherent quasi-monochromatic source such as a light emitting diode (LED) illuminates the samples of interest after being spatially filtered by a large aperture (e.g., 0.05–0.1 mm diameter). This incoherent light source picks up partial spatial coherence that is sufficiently large to record lensfree in-line holograms of the worms on the CCD chip. These acquired in-line holograms can then be rapidly processed using iterative recovery algorithms[18,19] to create lensfree transmission images of the C. elegans samples over the entire active area of the sensor-chip, matching the imaging FOV of the fluorescent channel. Figs. 6-2 and 6-3 illustrate such reconstructed lensfree holographic images of the samples, where the lensfree fluorescent images of the same worms were also digitally super-imposed, creating a hybrid image of the C. elegans (i.e., both fluorescent and transmission). It is evident from these lensfree images that the spatial resolution of this platform is modest compared to a regular lens-based microscope. On the other hand, the main advantages of this platform are its ultra-wide FOV and compact on-chip interface (see Fig. 6-1) which might provide an important match for ultra-high throughput screening of C. elegans samples within automated micro-fluidic systems.

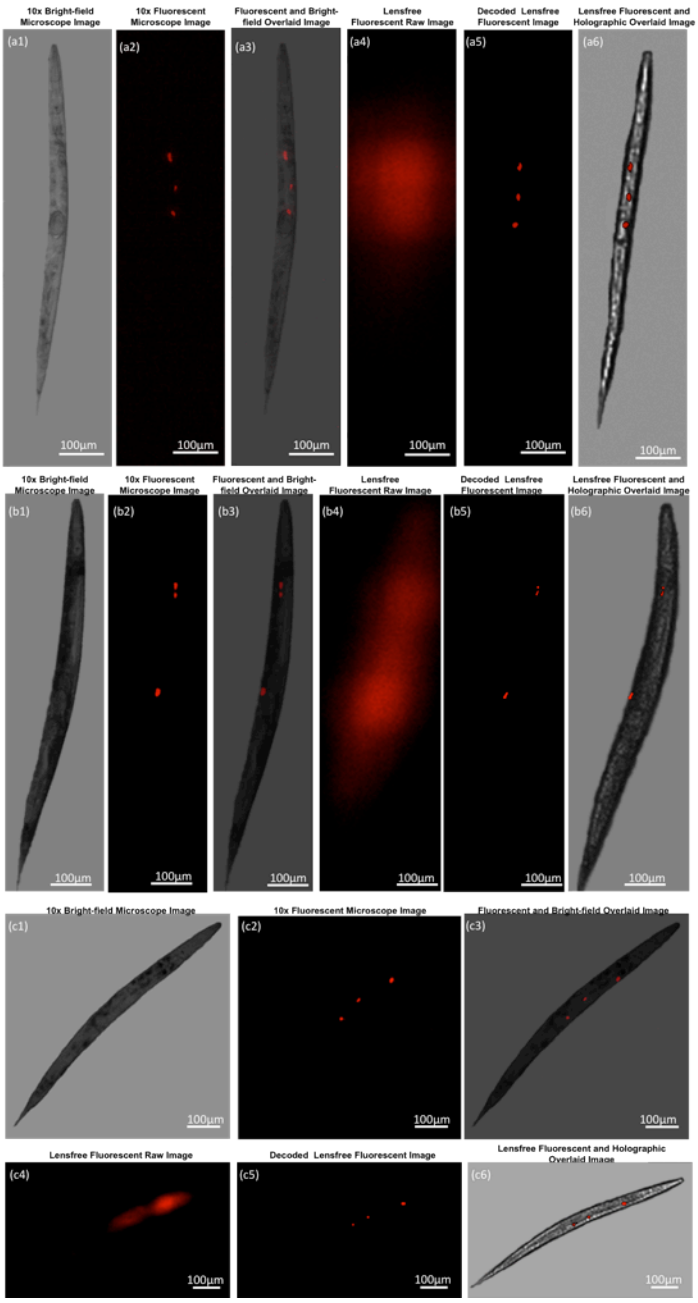

Figure 6-2 | Lensfree on-chip fluorescent imaging of transgenic C. elegans is shown for three individual animals using KAF-8300 sensor. (a4), (b4) and (c4) illustrate the lensfree fluorescent raw images that all look blurry at the detector plane. Compressive decoding of these blurry patterns enabled digital reconstruction of much higher resolution fluorescent images of these C. elegans samples as shown in (a5), (b5) and (c5), respectively. 10× objective-lens fluorescent microscope images of the same worms shown in (a2), (b2) and (c2) agree well with the decoded lensfree fluorescent images. In addition to fluorescent imaging, the same lensfree platform also permits holographic[18] transmission imaging of the same samples such that hybrid images can be created by superimposing the decoded lensfree fluorescent images and the reconstructed holographic images as shown in (a6), (b6) and (c6). Microscope comparisons of the same samples are also provided in (a3), (b3) and (c3), respectively. Slight rotations of the worms are observed between the lensfree decoded images and their microscope comparison images since they are acquired at different experiments.

Furthermore, I would like to also point to an alternative lensfree imaging configuration that can also perform fluorescent imaging of C. elegans samples on a chip. In this modified configuration (refer to Figs. 6-4 to 6-6 for details), I make use of a fiber-optic faceplate (see Chapter 4 and 5 for details) inserted underneath the sample substrate to control and tailor the fluorescent PSF of the imaging platform.

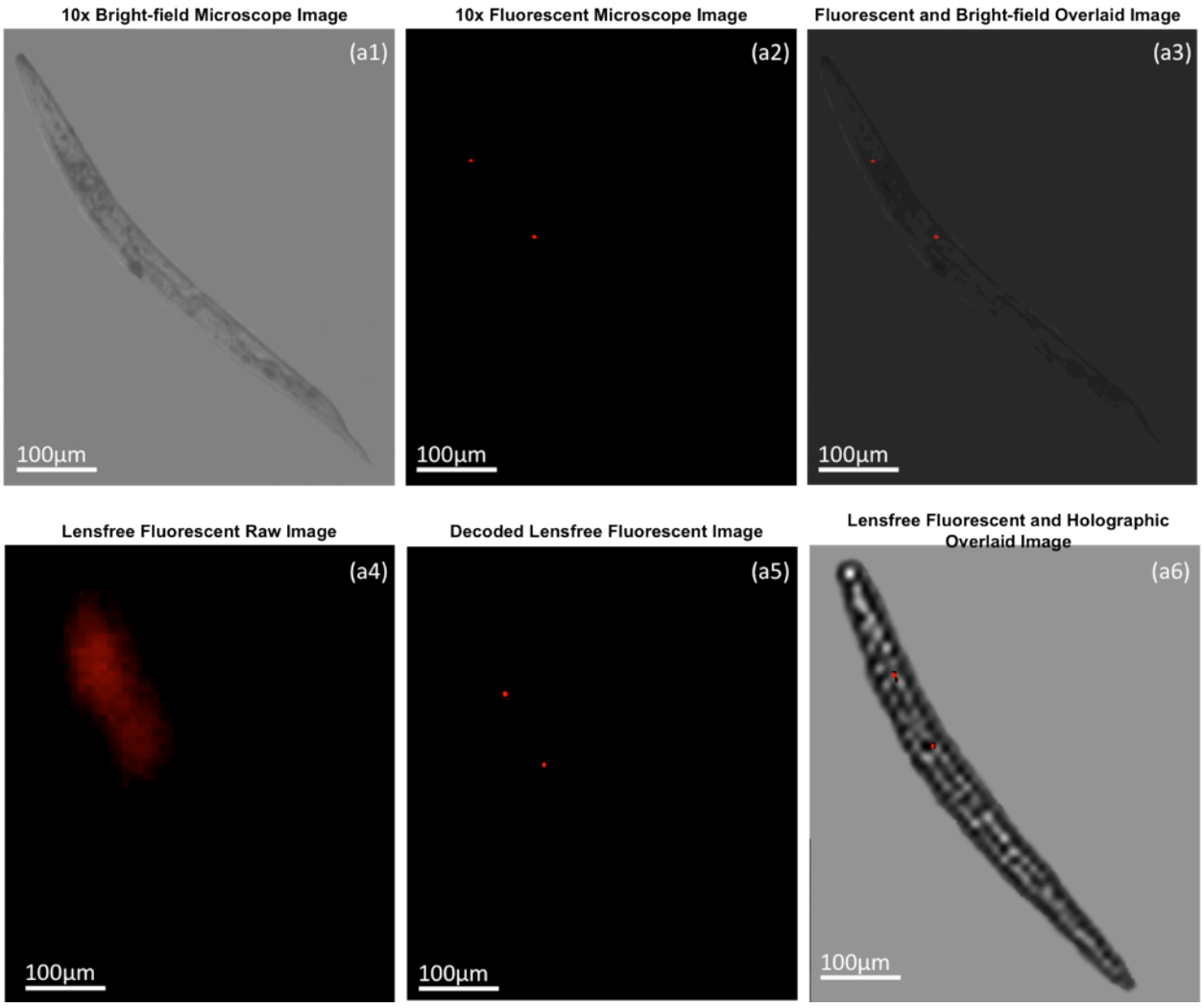

Figure 6-3 | Same as in Fig. 6-2, except this time for a different sensor chip (KAF-11002; 9µm pixel size, 11 MPixel). Similar to Fig. 6-2, the decoded lensfree fluorescent image of the transgenic C. elegans sample provides a decent match to a conventional fluorescent microscope image of the same worm (acquired with a 10× objective-lens, NA = 0.25). Slight rotation of the worm is observed between the lensfree decoded image and its microscope comparison image since the two are acquired at different experiments.

The use of a fiber-optic faceplate in lensfree on-chip imaging (see Fig. 6-4) can be quite valuable for tailoring the fluorescent PSF of the platform which could also provide an SNR advantage for operating at large vertical distances between the sample and sensor planes. This might especially be useful if physical isolation of the samples from the electronics of the sensor board is desired, i.e., the thickness of the faceplate can be increased without significantly affecting the fluorescent PSF. Therefore for certain applications, the use of such a planar optical component in lensfree fluorescent on-chip imaging could be essential.

Motivated by its potential, I tested the fluorescent imaging performance of the lensfree set-up shown in Fig. 6-4 using two different faceplates with numerical apertures (NAs) of 0.3 and 1.0. The thickness of each faceplate was ≥ 3 mm which significantly increased the vertical distance between the sample and the sensor-chip, compared to the earlier configuration given in Fig. 6-1. The comparison of the PSFs of these two faceplate configurations is provided in Fig. 6-4. The light collection efficiency of the larger NA faceplate is significantly better, since more fibers of the faceplate can guide the fluorescent emission from a point source. This, however, also makes its PSF slightly broader when compared to the PSF of the lower NA faceplate. On the other hand, despite their slight differences, both of the faceplates enable good quality lensfree imaging of transgenic C. elegans samples as illustrated in Figs. 6-5 and 6-6, where my lensfree compressive decoding results very well match to conventional fluorescent microscope images of the same samples.

Despite its decent fluorescent imaging performance as shown in these results, one limitation of this faceplate based lensfree on-chip imaging approach (Fig. 6-4) is that unlike the earlier configuration shown in Fig. 6-4, it does not permit lensfree holographic transmission imaging of the samples from the top. The main reason for this limiting behavior is that the optical modes of

the faceplate mess the phase information of the holographic fields that propagate towards the sensor-array.

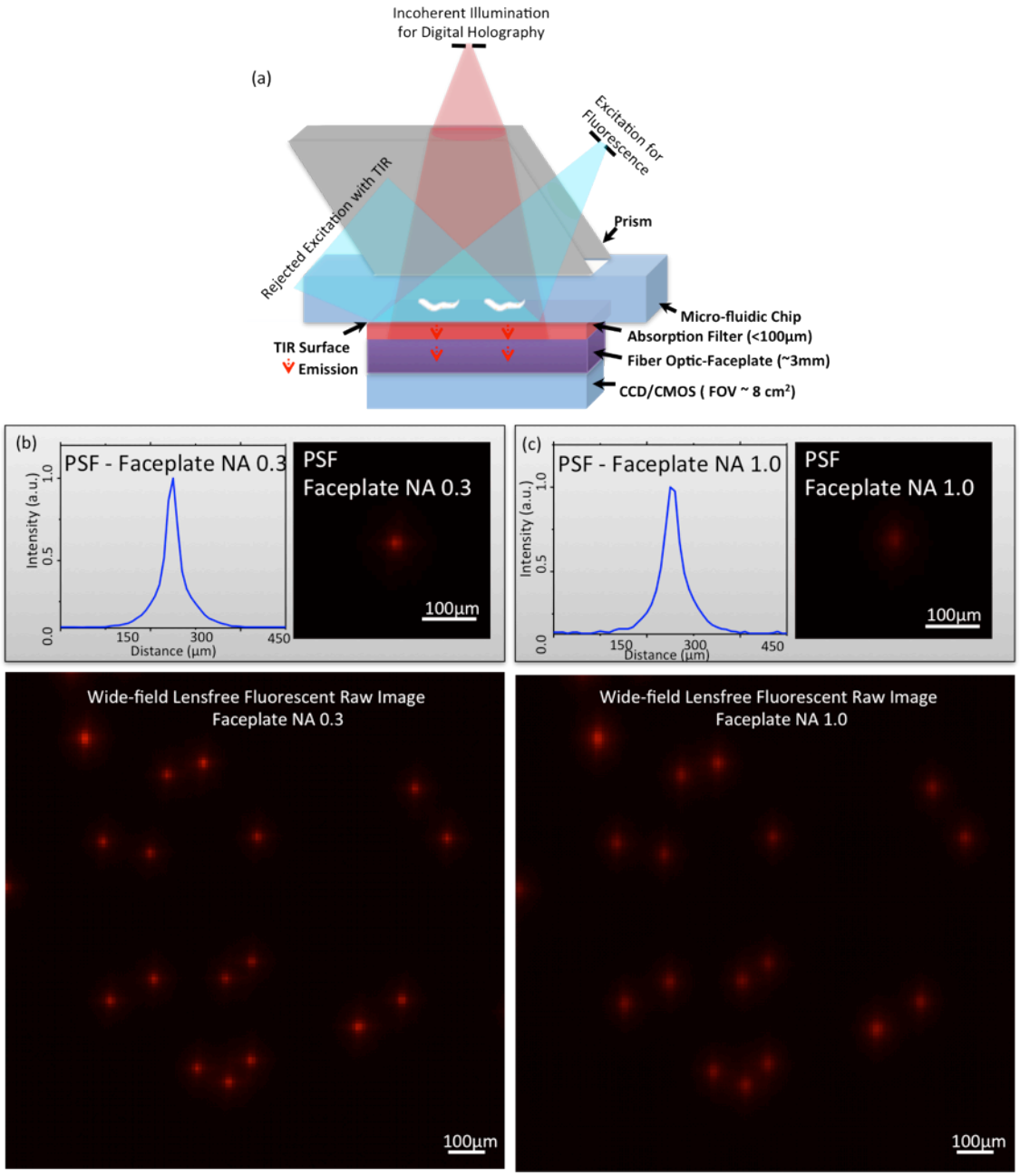

Figure 6-4 | (a) An alternative lensfree fluorescent on-chip imaging geometry is shown. The imaging system is kept the same as in Fig. 6-1, except insertion of the fiber-optic faceplate between the sample and the sensor. This geometry provides SNR advantages especially for operating at large distances between the fluorescent objects and the sensor board. The measured PSF of the faceplate(FP) based lensfree imaging geometry shown in Fig. 6-4 is demonstrated using 10 µm fluorescent particles. The left PSF corresponds to an FP with 0.3 NA, whereas the right one is for an FP with 1.0 NA. In (b) and (c), a comparison of the lensfree images of fluorescent micro-particles using these two different faceplates is presented over the same imaging field-of-view. Sensor-chip: KAF-11002.

While such fiber-optic faceplates are regularly used for focal-plane arrays to relay intensity images created by a lens-based imaging system, their use in lensfree holographic on-chip imaging would introduce aberrations since the phase information of the holographic fields will now be disordered. Regardless of this partial limitation, the use of such faceplates in lensfree fluorescent on-chip imaging would be quite useful for high-throughput imaging applications especially when physical isolation of the samples from the electronics of the sensor board is needed.

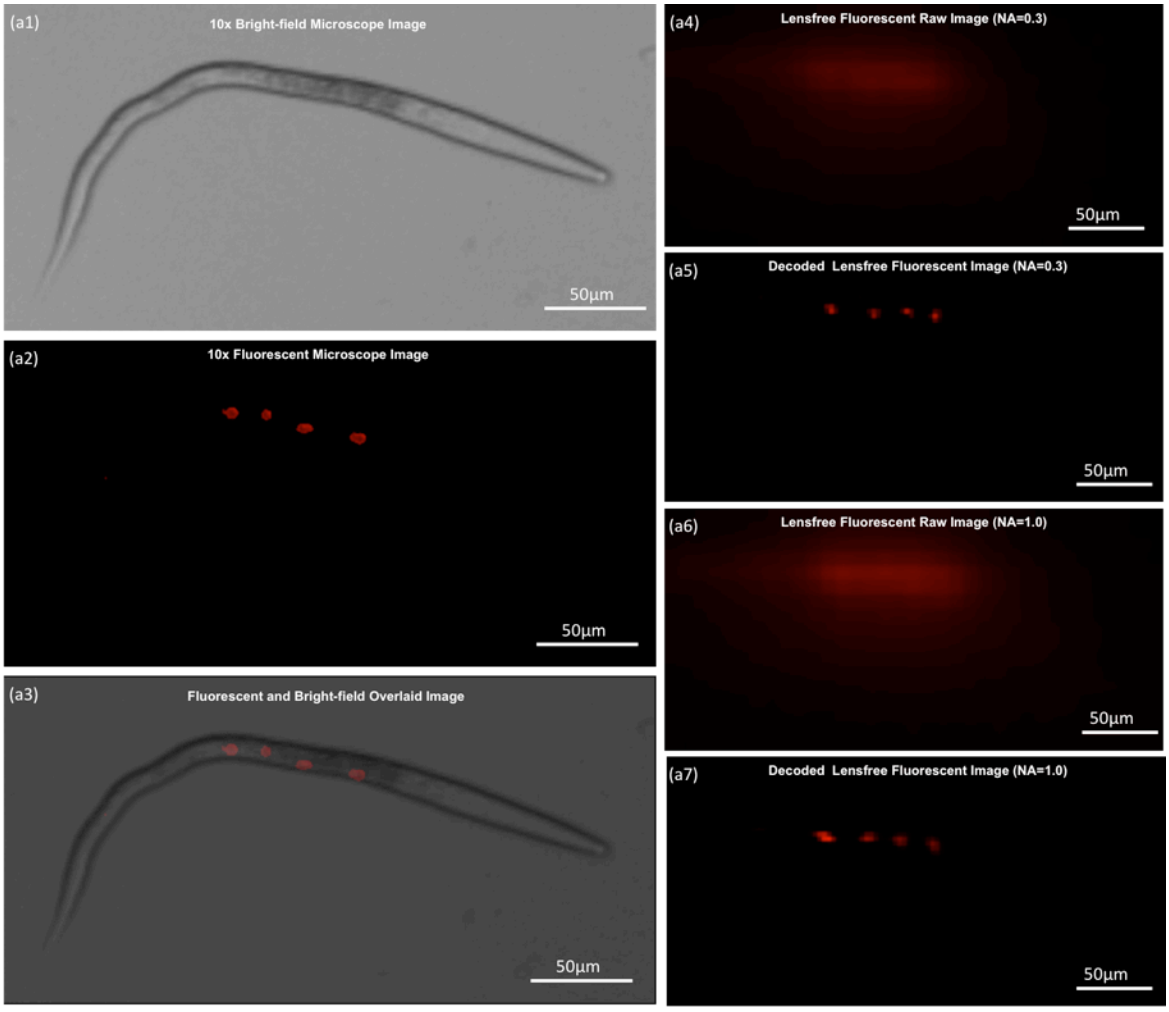

Figure 6-5 | Same as in Figs. 6-2 and 6-3, except that the lensfree imaging set-up now involves the use of a faceplate as illustrated in Fig. 6-4. The decoded lensfree fluorescent images with both of the faceplates (NA = 0.3 and 1.0) agree well with conventional fluorescent microscope image of the same transgenic C. elegans. KAF-11002 sensor-chip was used in these experiments. Slight rotation of the worm is observed between the lensfree decoded image and its corresponding microscope comparison image since the two are acquired at different experiments.

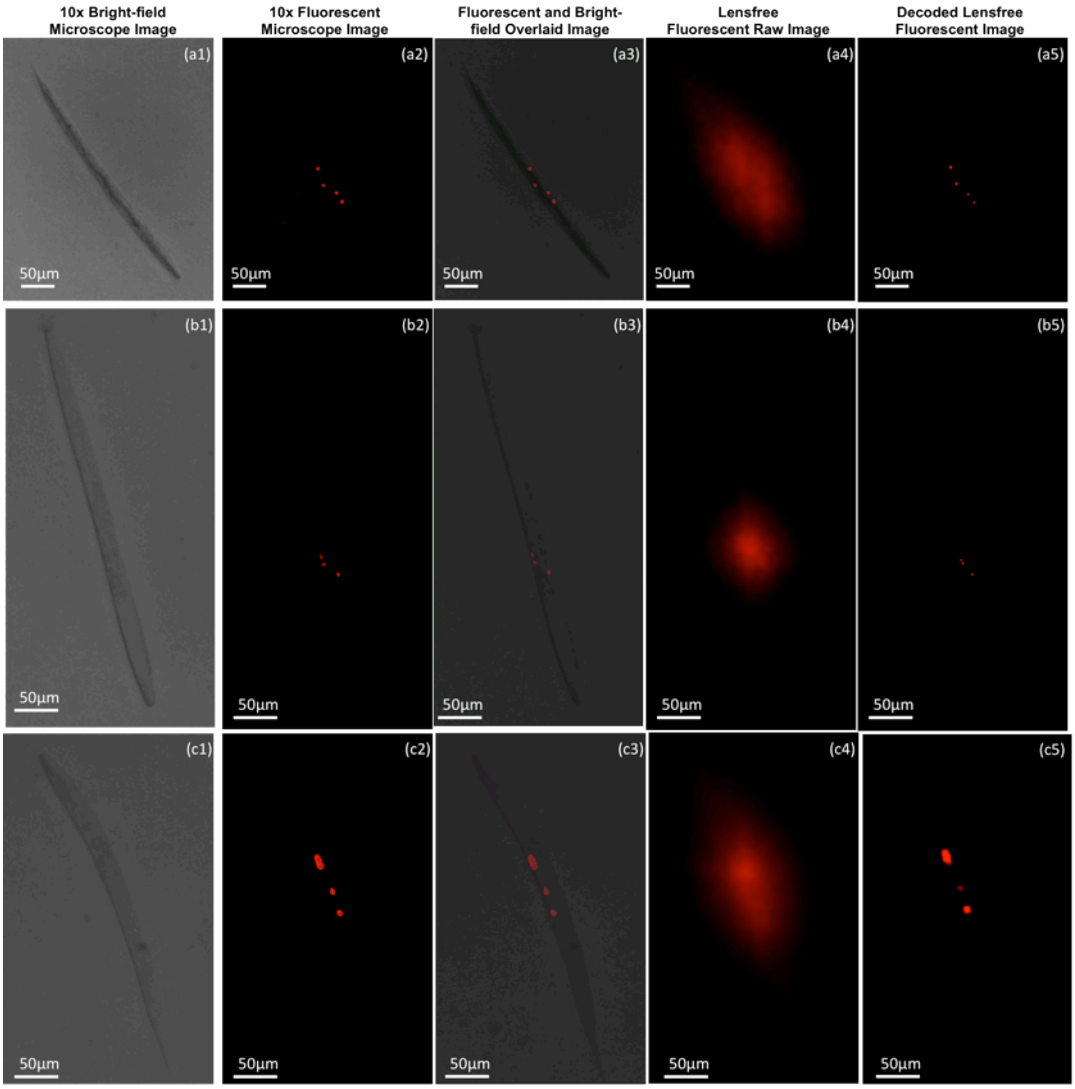

Figure 6-6 | Same as in Fig. 6-5, except that KAF-8300 sensor-chip was used. Once again the decoded lensfree fluorescent images with the use of a faceplate (NA = 1.0) agree well with conventional fluorescent microscope images of the same transgenic samples. Slight rotations of the worms are observed between the lensfree decoded images and their microscope comparison images since they are acquired at different experiments.

In conclusion, I have demonstrated lensfree fluorescent imaging of transgenic C. elegans over an ultra wide field-of-view of >2–8 cm^2 with a spatial resolution of ~10 μm. This is the first time that a lensfree on-chip imaging platform has achieved fluorescent imaging of C. elegans. I tested the efficacy of this on-chip imaging approach with different types of opto-electronic sensors to achieve a similar imaging and decoding performance independent of the imaging chip.

Furthermore, I demonstrated that this wide FOV lensfree fluorescent imaging platform can also perform bright-field imaging of the same samples using partially-coherent lensfree digital in-line holography. This unique combination permits ultra-wide field dual-mode imaging of C. elegans which could provide a useful tool for e.g., high-throughput screening applications.

6.4 References

1. Lehner, B., Crombie, C., Tischler, J., Fortunato, A. & Fraser, A. G. Systematic mapping of genetic interactions in Caenorhabditis elegans identifies common modifiers of diverse signaling pathways. Nat. Genet. **38,** 896–903 (2006).
2. Pinkston-Gosse, J. & Kenyon, C. DAF-16/FOXO targets genes that regulate tumor growth in Caenorhabditis elegans. Nature Genetics **39,** 1403–1409 (2007).
3. Mellem, J. E., Brockie, P. J., Madsen, D. M. & Maricq, A. V. Action potentials contribute to neuronal signaling in C. elegans. Nat. Neurosci. **11,** 865–867 (2008).
4. Yanik, M. F. et al. Neurosurgery: Functional regeneration after laser axotomy. Nature **432,** 822–822 (2004).
5. Rohde, C. B., Zeng, F., Gonzalez-Rubio, R., Angel, M. & Yanik, M. F. Microfluidic system for on-chip high-throughput whole-animal sorting and screening at subcellular resolution. PNAS **104,** 13891–13895 (2007).
6. Crane, M. M., Chung, K. & Lu, H. Computer-enhanced high-throughput genetic screens of C. elegans in a microfluidic system. Lab Chip **9,** 38–40 (2009).
7. Chokshi, T. V., Bazopoulou, D. & Chronis, N. An automated microfluidic platform for calcium imaging of chemosensory neurons in Caenorhabditis elegans. Lab Chip **10,** 2758–2763 (2010).
8. Burns, A. R. et al. High-throughput screening of small molecules for bioactivity and target identification in Caenorhabditis elegans. Nat Protoc **1,** 1906–1914 (2006).
9. Dupuy, D. et al. Genome-scale analysis of in vivo spatiotemporal promoter activity in Caenorhabditis elegans. Nature Biotechnology **25,** 663–668 (2007).

10. Rea, S. L., Wu, D., Cypser, J. R., Vaupel, J. W. & Johnson, T. E. A stress-sensitive reporter predicts longevity in isogenic populations of Caenorhabditis elegans. Nature Genetics **37,** 894–898 (2005).

11. Doitsidou, M., Flames, N., Lee, A. C., Boyanov, A. & Hobert, O. Automated screening for mutants affecting dopaminergic-neuron specification in C. elegans. Nat. Methods **5,** 869–872 (2008).

12. Pulak, R. Techniques for analysis, sorting, and dispensing of C. elegans on the COPAS flow-sorting system. Methods Mol. Biol. **351,** 275–286 (2006).

13. Semple, J. I., Garcia-Verdugo, R. & Lehner, B. Rapid selection of transgenic C. elegans using antibiotic resistance. Nature Methods **7,** 725–727 (2010).

14. Coskun, A. F., Su, T.-W. & Ozcan, A. Wide field-of-view lens-free fluorescent imaging on a chip. Lab Chip **10,** 824–827 (2010).

15. Coskun, A. F., Sencan, I., Su, T.-W. & Ozcan, A. Lensless wide-field fluorescent imaging on a chip using compressive decoding of sparse objects. Optics Express **18,** 10510 (2010).

16. Seo, S., Su, T.-W., Tseng, D. K., Erlinger, A. & Ozcan, A. Lensfree holographic imaging for on-chip cytometry and diagnostics. Lab Chip **9,** 777–787 (2009).

17. Seo, S. et al. High-Throughput Lens-Free Blood Analysis on a Chip. Anal. Chem. **82,** 4621–4627 (2010).

18. Isikman, S. O. et al. Color and monochrome lensless on-chip imaging of Caenorhabditis elegans over a wide field-of-view. Lab Chip **10,** 1109–1112 (2010).

19. Mudanyali, O. et al. Compact, light-weight and cost-effective microscope based on lensless incoherent holography for telemedicine applications. Lab Chip **10,** 1417–1428 (2010).

20. Tseng, D. et al. Lensfree microscopy on a cellphone. Lab Chip **10,** 1787–1792 (2010).

21. Su, T.-W. et al. Multi-angle lensless digital holography for depth resolved imaging on a chip. Opt. Express **18,** 9690–9711 (2010).

22. RICHARDSON, W. H. Bayesian-Based Iterative Method of Image Restoration. J. Opt. Soc. Am. **62,** 55–59 (1972).

23. Lucy, L. B. An iterative technique for the rectification of observed distributions. The Astronomical Journal **79,** 745 (1974).

24. Biggs, D. S. C. & Andrews, M. Acceleration of iterative image restoration algorithms. Appl. Opt. **36,** 1766–1775 (1997).

25. Donoho, D. L. Compressed sensing. IEEE Transactions on Information Theory **52,** 1289 – 1306 (2006).

26. Candes, E. J. & Tao, T. Near-Optimal Signal Recovery From Random Projections: Universal Encoding Strategies? IEEE Transactions on Information Theory **52,** 5406 –5425 (2006).

27. Candès, E. J., Romberg, J. K. & Tao, T. Stable signal recovery from incomplete and inaccurate measurements. Communications on Pure and Applied Mathematics **59,** 1207–1223 (2006).

28. Kim, S.-J., Koh, K., Lustig, M., Boyd, S. & Gorinevsky, D. An Interior-Point Method for Large-Scale l1-Regularized Least Squares. IEEE Journal of Selected Topics in Signal Processing **1,** 606 –617 (2007).

29. Candes, E. J., Romberg, J. & Tao, T. Robust uncertainty principles: exact signal reconstruction from highly incomplete frequency information. IEEE Transactions on Information Theory **52,** 489 – 509 (2006).

30. Bioucas-Dias, J. M. & Figueiredo, M. A. T. A New TwIST: Two-Step Iterative Shrinkage/Thresholding Algorithms for Image Restoration. IEEE Transactions on Image Processing **16,** 2992 –3004 (2007).

31. Richard, C., Renaudin, A., Aimez, V. & Charette, P. G. An integrated hybrid interference and absorption filter for fluorescence detection in lab-on-a-chip devices. Lab Chip **9,** 1371–1376 (2009).

32. Loria, P. M., Hodgkin, J. & Hobert, O. A conserved postsynaptic transmembrane protein affecting neuromuscular signaling in Caenorhabditis elegans. J. Neurosci. **24,** 2191–2201 (2004).

33. Kural, C., Nonet, M. L. & Selvin, P. R. FIONA on Caenorhabditis elegans. Biochemistry **48,** 4663–4665 (2009).

Chapter 7 Summary

On-chip computational fluorescence microscopy is an emerging platform that enables high-throughput screening of micro-systems (e.g., microfluidic chips)[1] over a wide field-of-view without the use of any lenses, thin-film filters or mechanical scanners[2–7]. The presented lensfree fluorescence microscopy modality, achieving < 4 μm spatial resolution, provides at least an order of magnitude larger FOV compared to a conventional 10x objective lens and lends itself to a compact architecture that can easily be integrated with microfluidic chips for massively parallel screening of fluorescently labeled cells or small animals. This high- throughput lensfree fluorescence microscopy platform, combined with the state- of-the-art bio-chips, could pave the way toward rapid on-chip diagnostic systems for biomedical applications, including rare-cell analysis, high-throughput cytometry, as well as small animal research.

7.1 Methods

The on-chip lensfree fluorescent imaging modality utilizes an excitation interface (e.g., a prism, a hemisphere or a planar waveguide) to pump the objects of interest located within a bio-chip, where the excitation light is mostly rejected through total internal reflection (TIR) occurring at the bottom facet of the sample holder (Fig.7-1 a1, b1, c1). In addition to TIR rejection, an inexpensive absorption filter is also used to remove the weakly scattered excitation light that does not obey the TIR process. Upon removal of the excitation, only the fluorescent emission from the objects is collected using e.g., free-space, fiber-optic-faceplate (FOF) or fiber-optic-taper (FOT) based optics, and is then delivered to a large-format sensor- array (e.g., CMOS or CCD) that has an active area of e.g., >9 cm^2, which is also equivalent to the sample FOV. Finally, by using an image reconstruction method (e.g., deconvolution or compressive decoding),

the detected lensfree fluorescent images are rapidly processed to yield higher-resolution microscopic images of the specimen all across this FOV. Typical reconstructed images of this lensfree fluorescence microscopy platform are demonstrated in Fig.7-1 a3, b3, c3, where 4- 10 μm diameter micro-beads are imaged using the lensfree on-chip imager.

Components of the on-chip fluorescence imaging platform: In this sub-section, I will overview the key components of the lensfree on-chip fluorescence microscopy platform.

(1) Excitation/illumination design: Fluorescently labeled specimen located within micro-fluidic devices can be probed with various illumination/excitation configurations: the fluorescence excitation can be achieved through e.g., a prism (e.g., rhomboid, dove prisms - Fig.7-1 a1, a2), or a hemi-sphere (Fig.7-1 b1, b2) or a waveguide (Fig.7-1 c1, c2), where incoherent sources such as simple light emitting diodes can be used to provide uniform illumination over a wide FOV.

(2) Light collection and detection design: In this on-chip imaging platform, once the specimen is excited through one of the illumination methods presented above, the fluorescence emission is collected and then delivered to an optoelectronic sensor-array. As for the collection of the fluorescence signal, three different configurations can be utilized, incorporating free-space collection, FOF-based collection or alternatively FOT-based collection (see Fig. 7-2).

Although free-space collection enables monitoring of bio-chips over a wide FOV, because the fluorescent emission is not directional and rapidly diverges, the detected raw lensfree images become rather broad at the sensor plane. Therefore, to better control the spatial spreading of fluorescent signal in this platform, I employed a planar optical component, i.e. a FOF, which is located between the object and the sensor planes[3,7].

The FOF (Fig.7-2 b1, b2) is composed of a 2D array of fiber-optic cables that carry two-dimensional optical intensity information. Its function is to engineer the point-spread function

(PSF) (Fig.7-2 b3) of the on-chip imager, improving the signal-to-noise ratio (SNR) and the spatial resolution of the microscopy platform. As an alternative to a regular FOF, a FOT (Fig.7-2 c1, c2) can also be used, which has a larger density of fiber-optic cables on its top facet compared to the bottom one[6].

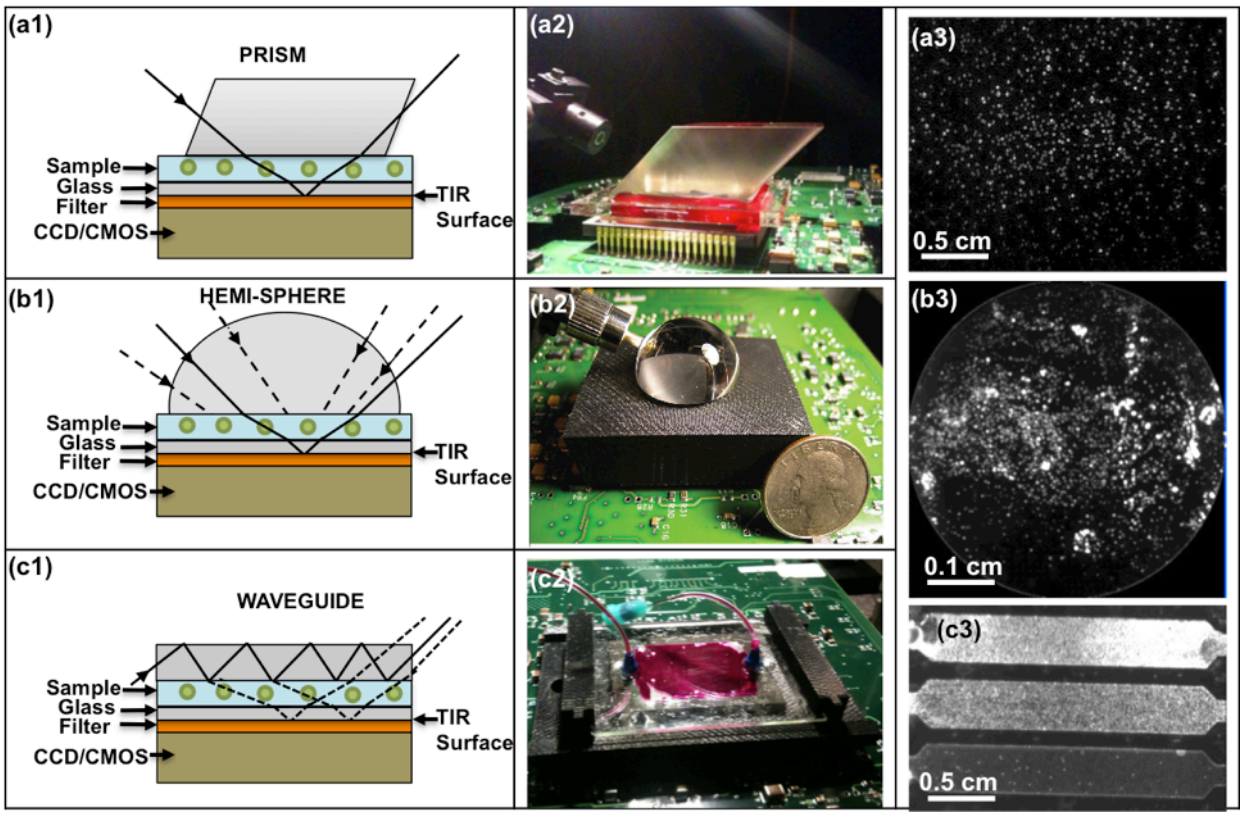

Figure 7-1 | The schematics (a1), (b1), (c1), corresponding experimental set-ups (a2), (b2), (c2) and typical wide-field fluorescence images (a3), (b3), (c3) of the various excitation delivery methods are shown.

FOT not only provides a better PSF (Fig. 7-2. c3), but also achieves magnification in this platform (e.g., 2-3X), which further helps us to increase spatial resolution, despite the reduced FOV due to the taper. Typical bead-pair lensfree images and the PSFs of various configurations are demonstrated in Fig. 7-2 a3, b3, and c3.

As for sampling of the fluorescent signal, once the emitted photons are transmitted through one of the collection methods, a sensor-array is used to digitize the fluorescence emission.

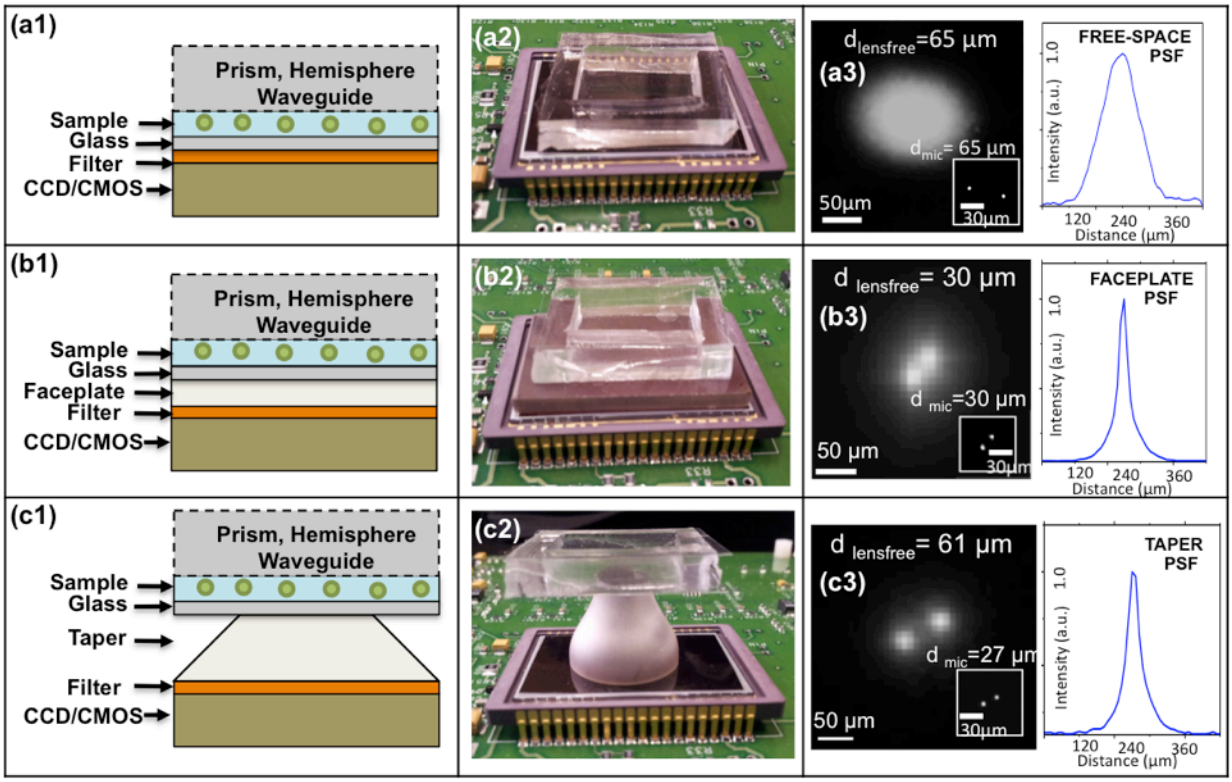

Figure 7-2 | The schematics (a1, b1, c1), corresponding experimental set-ups (a2, b2, c 2), lensfree bead-pair images and PSF analysis (a3, b3, c3) of the various light collection methods are shown.

These sensor-arrays vary based on the working principles active imaging areas, pixel sizes and frame rates. In terms of lensfree imaging, CCD sensors can in general be used to provide better sensitivity and larger FOV, while CMOS sensors can be employed for relatively cheaper and lighter weight designs (e.g. for field use).

(3) Bio-chip design: Together with the selection of an illumination and a collection/detection module, to handle the fluorescently labeled specimen, various bio-chip designs can be used, including glass-tape-glass based devices, PDMS (Polydimethylsiloxane)-channel-glass devices, or wide-area capillary arrays. One can select any of these device designs and then combine it with surface-chemistry protocols to achieve highly specific and sensitive on-chip lensfree

fluorescence microscopy and biosensing that could be very useful for rapid detection of pathogens, sub-population of cells, as well as molecular assays.

Reconstruction methods: Lensfree fluorescence raw images look blurry due to diffraction, and therefore, to partially undo the effect of diffraction and create higher resolution microscopic images, lensfree raw images are processed using image reconstruction methods, employing either a Lucy-Richardson deconvolution method[2,8,9] or a compressive sampling based decoding algorithm[3,10–12]. Starting with an initial measurement of the incoherent PSF of the on-chip system, lensfree images are reconstructed within a few minutes (e.g., 10 min for 9 cm^2 FOV using a standard PC - Fig. 7-3a). To quantify the spatial resolution, closely packed bead pairs are reconstructed, verifying <4 μm spatial resolution based on a FOT-based collection platform (Fig.7-3 d1, d2, d3)[6]. Furthermore, to demonstrate the sensor independent performance of this platform, the PSFs of the two different CCD sensors are measured that show a noticeable variance in their 2D patterns; however the reconstruction of closely packed beads can still be achieved as illustrated in Fig. 7-3 b1-3 and c1-3.

7.2 Results

This on-chip fluorescence imaging platform, combining a compact experimental set-up and rapid image reconstruction algorithms, with also its wide field imaging capability could especially be useful for high-throughput screening applications. To demonstrate its proof-of-concept, I performed experiments with bodily fluids (e.g., blood samples with labeled white blood cells)[7], water-borne parasites (e.g., Giardia Muris)[6], as well as genetically modified small model animals (e.g., transgenic Caenorhabditis Elegans)[5].

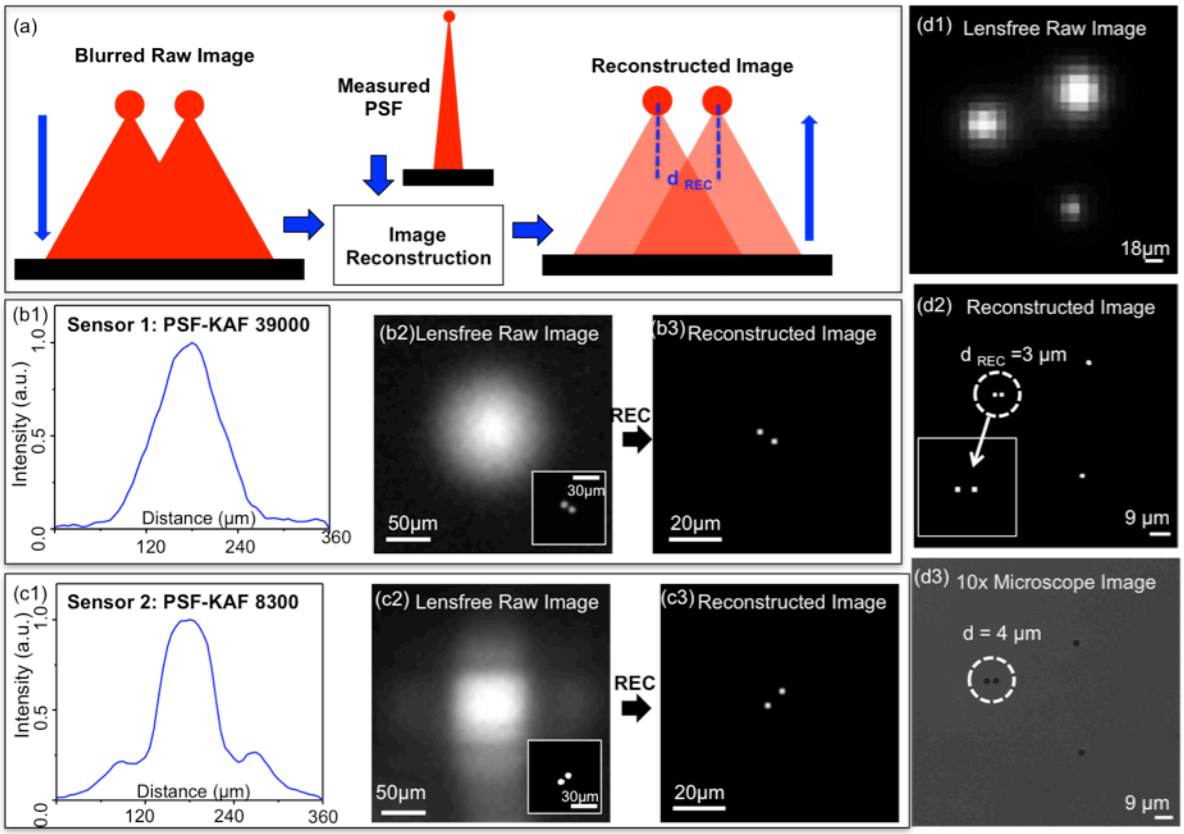

Figure 7-3 | The image reconstruction sketch (a) and PSFs of the different sensors with the sensor independent processing (b1-3, c1-3) are demonstrated. The resolving power of the imaging platform is quantified by reconstructing bead-pairs, verifying < 4 μm spatial resolution (d1-3).

The results of these experiments are presented in Fig. 7-4 that also includes comparisons against lens-based conventional microscope images of the same specimen. In Fig.7-4 (a) wide-field fluorescence image (~9cm^2 FOV) of labeled white blood cells are shown. Fig.7-4 (b2) illustrates the reconstruction results of digitally zoomed images of white blood cells as shown in Fig.7-4 (b1), agreeing well with a conventional 10x fluorescent microscope image shown in Fig.7-4 (b3).

For water quality applications, in Fig.7-4 (c1) lensfree imaging of water-borne parasites is also presented, with the reconstructed results and microscope comparisons as shown in Fig.7-4

(c2) and Fig.7-4 (c3), respectively. Finally, I present lensfree imaging of C. Elegans in Fig.7-4 (d4-6).

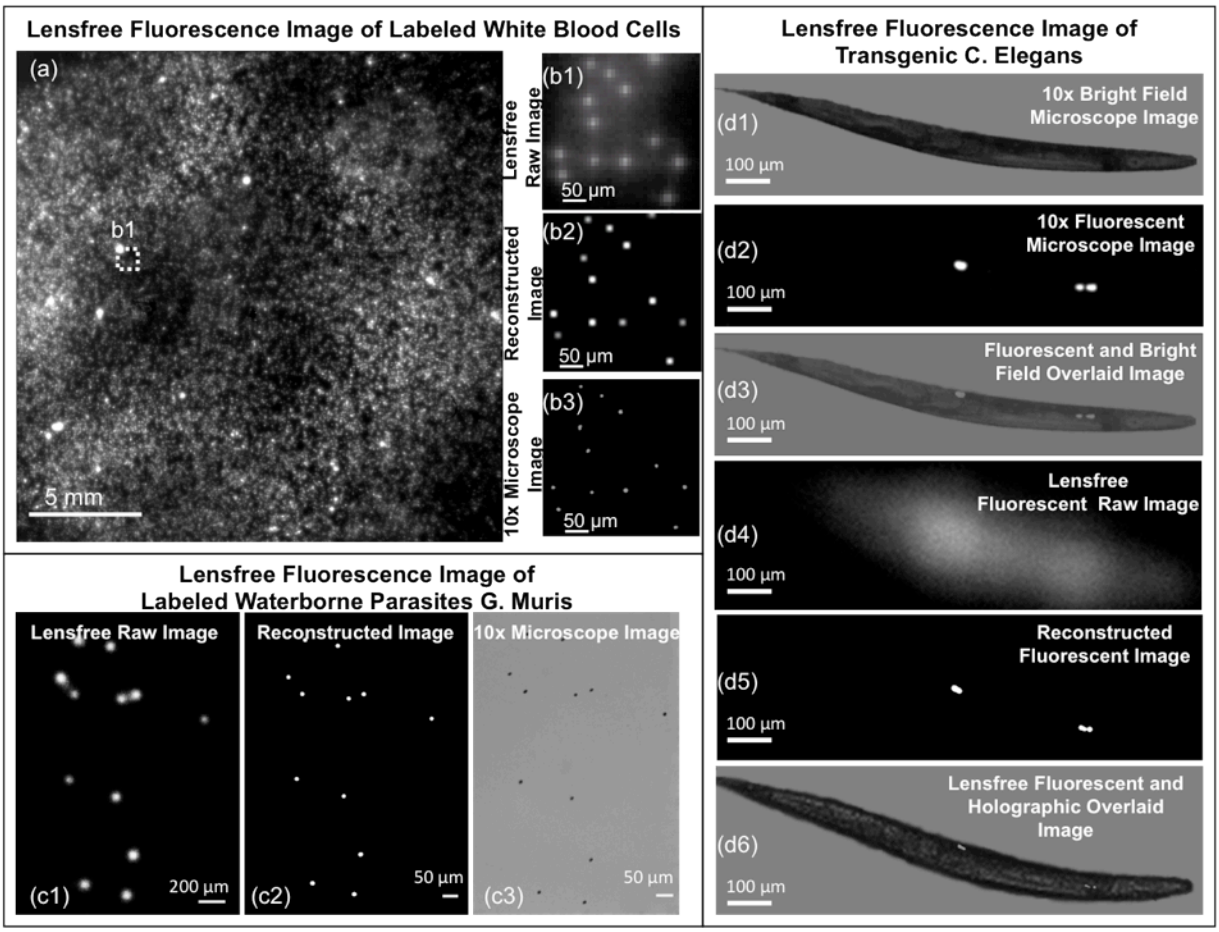

Figure 7-4 | Lensfree fluorescence images of white blood cells (a, b1-2), G. Muris parasites (c1-2) and C. Elegans (d4-6) are demonstrated, which agree well with 10X microscope comparisons.

7.3 Conclusion and future outlook

In this dissertation, I introduced an emerging wide-field lensfree fluorescent imaging modality, achieving < 3-4 µm spatial resolution over a large FOV of e.g., > 9 cm^2, that can rapidly monitor the state-of-art microfluidic chips toward high-throughput screening applications, including on-chip cytometry, rare-cell analysis, as well as small animal research. The presented imaging platform can also leverage other techniques/tools to further increase its spatial resolution,

incorporating e.g., (1) higher- magnification FOTs to increase the resolving power of the imager, (2) pixel super- resolution approaches[13] by shifting the fluorescent specimen to affectively create smaller size pixels, (3) through the use of nano-structured surfaces[14] to spatially modify the PSF of the on-chip imager, (4) fluorescent signal detection based on actively cooled sensor chips to enhance signal-to-noise ratio of this imaging system, (5) improved rejection performance in this on-chip system utilizing better absorption dyes, (6) illumination schemes involving, for example, the use of structured excitation light to selectively deliver the excitation to the fluorescent specimen, (7) better incoherent signal recovery algorithms that exploit sparsity of fluorescence images. Such a lensfree fluorescence imaging platform, combined with better optical components and computational approaches could in general be useful for wide-field imaging of bio-chips.

7.4 References

1. Nagrath, S. et al. Isolation of rare circulating tumour cells in cancer patients by microchip technology. Nature **450,** 1235–1239 (2007).

2. Coskun, A. F., Su, T.-W. & Ozcan, A. Wide field-of-view lens-free fluorescent imaging on a chip. Lab Chip **10,** 824–827 (2010).

3. Coskun, A. F., Sencan, I., Su, T.-W. & Ozcan, A. Lensless wide-field fluorescent imaging on a chip using compressive decoding of sparse objects. Optics Express **18,** 10510 (2010).

4. Coskun, A. F., Su, T., Sencan, I. & Ozcan, A. Lensfree Fluorescent On-Chip ImagingUsing Compressive Sampling. Opt. Photon. News **21,** 27–27 (2010).

5. Coskun, A. F., Sencan, I., Su, T.-W. & Ozcan, A. Lensfree Fluorescent On-Chip Imaging of Transgenic Caenorhabditis elegans Over an Ultra-Wide Field-of-View. PLoS ONE **6,** e15955 (2011).

6. Coskun, A. F., Sencan, I., Su, T.-W. & Ozcan, A. Wide-field lensless fluorescent microscopy using a tapered fiber-optic faceplate on a chip. The Analyst **136,** 3512 (2011).

7. Coskun, A. F., Su, T.-W., Sencan, I. & Ozcan, A. Lensless Fluorescent Microscopy on a Chip. Journal of Visualized Experiments, **54**, e3181 (2011).

8. Lucy, L. B. An iterative technique for the rectification of observed distributions. The Astronomical Journal **79,** 745 (1974).

9. RICHARDSON, W. H. Bayesian-Based Iterative Method of Image Restoration. J. Opt. Soc. Am. **62,** 55–59 (1972).

10. Candes, E. J., Romberg, J. & Tao, T. Robust uncertainty principles: exact signal reconstruction from highly incomplete frequency information. IEEE Transactions on Information Theory **52,** 489 – 509 (2006).

11. Candès, E. J., Romberg, J. K. & Tao, T. Stable signal recovery from incomplete and inaccurate measurements. Communications on Pure and Applied Mathematics **59,** 1207–1223 (2006).

12. Donoho, D. L. Compressed sensing. IEEE Transactions on Information Theory **52,** 1289 – 1306 (2006).

13. Ur, H. & Gross, D. Improved resolution from subpixel shifted pictures. CVGIP: Graph. Models Image Process. **54,** 181–186 (1992).

14. Khademhosseinieh, B., Biener, G., Sencan, I. & Ozcan, A. Lensfree color imaging on a nanostructured chip using compressive decoding. Appl Phys Lett **97,** 211112 (2010).

Appendix Personalized allergen testing on a cellphone

Parts of this chapter have already been published in Lab on a Chip, 13, 636-640 (2013).

A.1 Introduction

Food allergy is an emerging public concern, affecting as many as 8% of young children and 2% of adults, especially in developed countries.[1–3] Allergic reactions might be life-threatening by inducing e.g., respiratory and gastrointestinal symptoms, systemic, cutaneous and fatal reactions, which can even be triggered by small traces of food allergens.[3–6] Although the food consumer protection act[7] ensures the safety of the allergic individuals by labeling pre-packaged food with a list of potential allergen-related ingredients, there still might be hidden amounts of allergens in processed food due to possible cross-contamination occurring in the processing, manufacturing and transportation of food samples.[8–11] Toward detection of such hidden allergens in food products, numerous analytical methods have been developed, including the ones that are based on polymerase chain reaction (PCR),[12] mass spectroscopy,[13] antibody-based immunoassays,[14] surface-plasmon-resonance (SPR) biosensors,[15] array immunoassays,[16] electrochemical immunosensors[17] and others.[18] These existing approaches have achieved very high sensitivities; however, they are relatively complex and require bulky equipment to perform the test, making them less suitable for personal use in public settings.

To provide an alternative solution to this important need, here I demonstrate a personalized allergen testing platform (termed iTube) running on a smart phone, which utilizes a sensitive colorimetric assay processed in test tubes for specific detection and quantification of allergens in food products (see Fig. A-1). This iTube platform, weighing approximately 40 grams, images the test tube along with a control tube using a cost-effective opto-mechanical attachment to the

cellphone camera unit. This attachment is composed of an inexpensive plastic plano-convex lens, two light-emitting diodes (LEDs), two light diffusers, and circular apertures to spatially control the imaging field-of-view. The test and control tubes, once activated with an allergen-specific sample preparation and closed with lids, are then inserted into this attachment from the side where the transmission intensities for each tube are acquired using the cellphone camera (see Fig. A-1). These tube images are then digitally processed within one second through a custom-developed smart application running on the cellphone for quantification of the amount of allergen present in the sample, as illustrated in Fig. A-2.

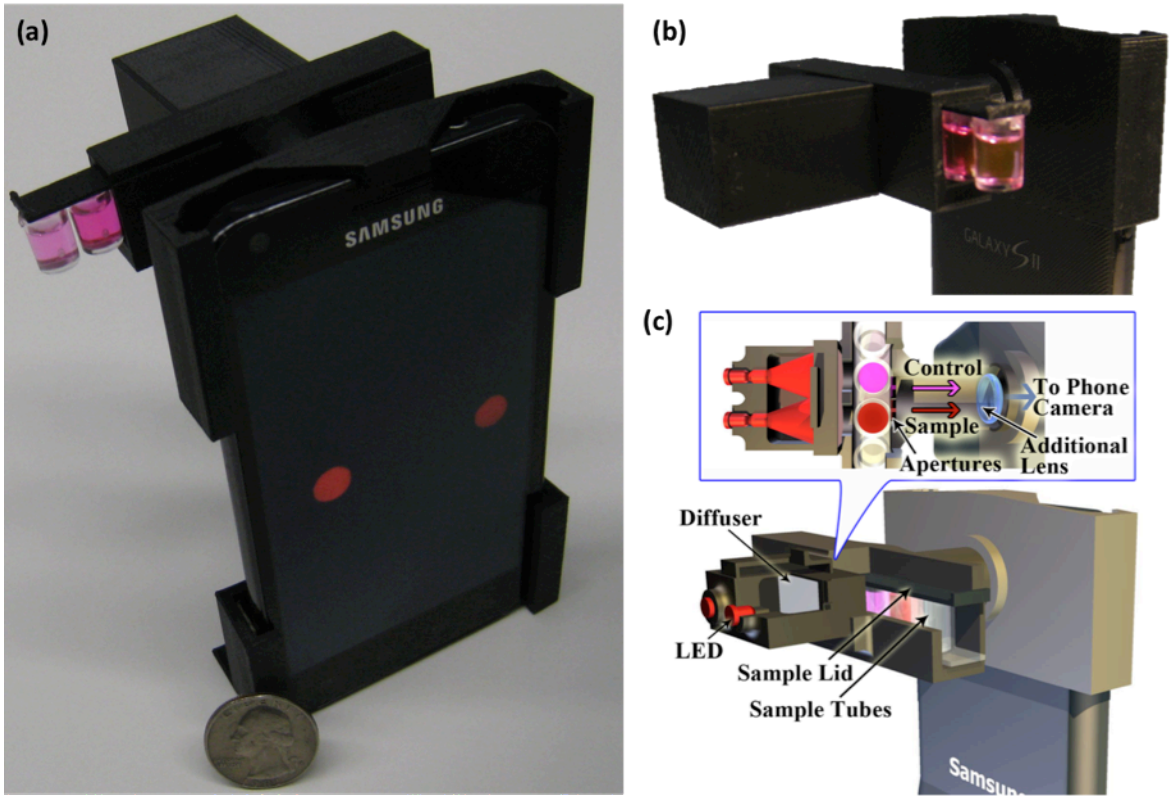

Figure A-1 | (a) A picture of the iTube platform, utilizing colorimetric assays and a smart phone-based digital reader, is shown. (b) The opto-mechanical attachment that is installed at the back of the cellphone is shown. Dimensions: 22 mm × 67 mm × 75 mm. (c) A schematic diagram of the same iTube platform is also illustrated.

Compared to visual inspection of the same tube assay by the human eye, a separate optical readout with its own software and optimized illumination and imaging configuration is

significantly more sensitive, repeatable and immune from manual reading errors. Furthermore, it also permits digital quantification of an allergen concentration beyond a yes/no decision. When compared to digital processing of cellphone camera pictures taken without a separate read-out attachment, i.e., under ambient light, the presented approach is much more robust, since it is independent of the optical spectrum or intensity of external lighting conditions. These might significantly vary based on the setting that the test is used, and therefore could result in sensitivity problems in e.g., airplanes or other poorly illuminated environments. Furthermore, using a separate optical attachment on the cellphone, as presented in this work, eliminates possible image artifacts due to the hand motion of the user, creating a more repeatable, reliable and sensitive platform for personal use in various public health settings including e.g., restaurants, schools, airplanes, etc.

A.2 Experimental methods

In this cellphone-based iTube platform, I designed a cost-effective digital tube reader and a smart application that measures the absorption of colorimetric assays and digitally converts raw transmission images captured by the cellphone into concentration measurements of the allergen traces detected in food samples.

Hardware design: Our digital reader was implemented on an Android phone (Samsung Galaxy S II, 1.2 GHz Dual Core ARM Cortex-A9 Processor, 8MP Camera with F/2.65 aperture and 4 mm focal length lens). The same tube reader can also be built on other smart phones, including an iPhone, as well as other Android devices with slight mechanical modifications. The 3D structure of the cellphone attachment was designed using Inventor software (Autodesk) and built using a 3D printer (Elite, Dimension), providing a lightweight (40 grams) and robust hardware that can be operated in field conditions. In this design, I utilized two interchangeable LEDs

(Digikey, 751-1089-ND, 650 nm peak wavelength with 15 nm bandwidth) to vertically illuminate the test and control tubes (see Fig. A-1). The wavelength of these LEDs was specifically chosen to match the absorption spectrum of the colorimetric assay performed in the test tube. To uniformly illuminate the cross-section of each tube (i.e., 8 mm × 12 mm), two diffusers (Digikey, 67-1845-ND) were also inserted between the LEDs and the tubes. The transmitted light through each tube of interest is then collected via two circular apertures (1.5 mm diameter) to be imaged onto the digital camera of the cellphone using a plano-convex lens (Edmund Optics, NT65-576, focal length 28 mm). This imaging configuration provides an optical demagnification of the tube cross-section by 28/4 = 7 fold, which permits fitting both the test (i.e., sample) and control tubes into the field-of-view of the cellphone camera (see Figs. A-1(a) or A-2(e)).

Android-based smart application: An Android application is custom developed, which functions as follows (see Fig. A-2):

(a) The user clicks on the iTube icon and starts to run the smart application on the mobile phone.

(b–d) The new window provides two options: either New Test or Instructions. Once Instructions tab is selected, the user protocol for allergen testing is displayed (see Fig. A-2(c)). Otherwise, if New Test is selected, the user is asked to identify the allergen type to be tested (Fig. A-2(d)).

(e) When the user decides on the type of allergen to be tested (e.g., peanut), the cellphone application powers on the digital camera of the phone. The user can then touch the screen of the mobile phone to simultaneously capture the transmission images of the tubes (i.e., both the sample and control tubes).

(f) These captured images are processed within one second (see the next subsection on digital processing for details) to determine the concentration of the selected allergen within a range of 1

to 25 parts per million (ppm). The test result is displayed as “positive” for ≥1 ppm or “negative” for <1 ppm.

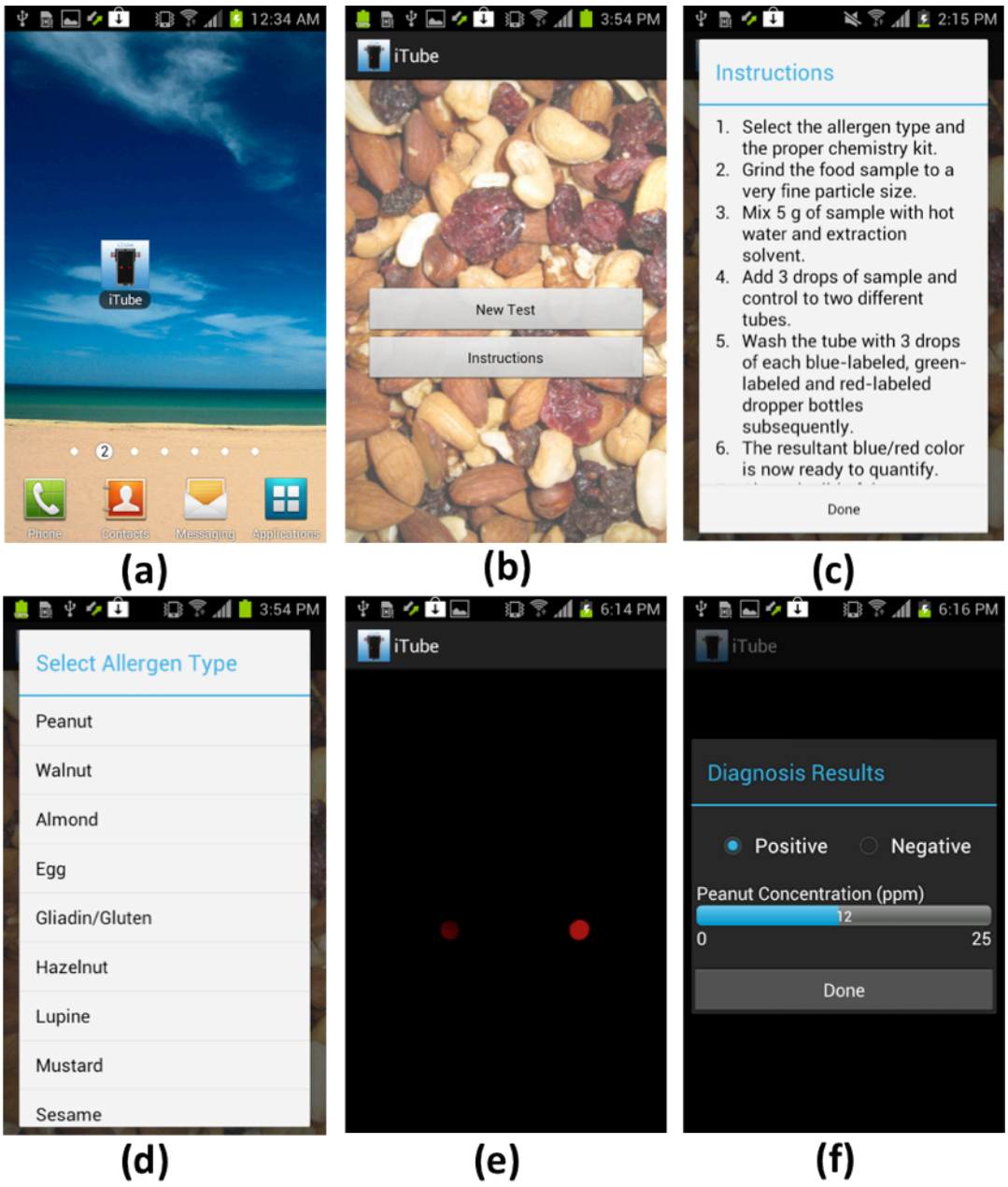

Figure A-2 | Screenshots of the iTube application running on an Android cellphone are shown. (a) Once the application runs, either New Test or Instructions tab can be selected. (c) The user can read the testing protocol explained under Instructions. (d) With the selection of New Test, an allergen type of interest can be designated within the pop-up menu. (e) Following the activation of the cellphone camera, the user can simply touch the screen to capture the transmission images of the test and control tubes. (f) The acquired images are rapidly processed on the cellphone to quantify the allergen amount within the target food sample.

Digital processing of tube images: The acquired transmission images of tubes (sample and control) are first converted into binary mask images by localizing their centroids. A rectangular frame (i.e., 300 × 300 pixels) around each one of these centroids is then used to calculate a transmission signal per tube. The resulting signal of the control tube is divided by a normalization factor (see the system calibration subsection for details), and then is divided by the signal calculated for the sample tube to determine the relative absorbance (A) of the assay, which scales with the allergen concentration within the sample. Finally, this relative absorbance value is divided by a calibration factor (refer to Fig. A-3 and the system calibration subsection for details), yielding the final concentration of the allergen (in ppm) measured within the sample of interest.

Colorimetric assay preparation: In this work, to demonstrate the proof of concept of the iTube platform, colorimetric assays were performed based on a food allergy test kit that is specific to peanuts, i.e., Veratox test kit, Neogen, 8430. The assay preparation starts with grinding the target food sample to a fine particle size and then 5 grams of the ground food sample is mixed with hot water (50–60 °C) and an extraction solvent. Three drops of this sample solution and the control solution that does not contain any food, are added separately to two different tubes. Following 10 min of incubation, the test and control tubes are rinsed sequentially with 3 drops of blue-labeled (conjugate), green-labeled (substrate) and red-labeled (stop solution) dropper bottles, where a wash buffer is also used to thoroughly clean the tubes in between each step, all of which adds another 10 min to the sample preparation in total. The resultant blue and red mixture color activated in the tubes can then be measured by the digital reader implemented on a cellphone, providing a quantified measurement of the peanut concentration within the sample.

System calibration: The iTube platform was calibrated by testing known amounts of peanut concentrations, ranging from 0 ppm, 1 ppm, 2.5 ppm, 5 ppm, 10 ppm and 25 ppm (see Fig. A-3). These calibration samples were then digitally quantified using iTube to find the relative absorbance (A) of each test tube:

$$A = \log 10 \left(\frac{I_{control}}{I_{test}} \right) \quad (1)$$

where I_{test} is the transmitted signal for the test tube and $I_{control}$ is the transmitted signal for the control tube. Assuming that the optical properties (e.g., reflection, absorption) of the tube containers are the same for both the sample and control tubes and that the illumination is uniform, i.e., approximately the same for both tubes, then A would be correlated to the concentration of the allergen in the sample tube. In this iTube platform, however, the LED intensity illuminating the control tube was measured to be slightly higher (i.e., 1.15 fold), and therefore I divided the transmitted control signal ($I_{control}$) by a normalization factor of 1.15 to take this into account. Following 4 different tests for each concentration of peanuts (spanning 0 ppm to 25 ppm), the calibration curve of Fig. A-3 provides a linear fit with R = 0.99, i.e., A = 0.028C, where C is the peanut concentration in ppm. This linear fit/equation is used to quantify the target allergen concentration (C) in a given food product of interest by measuring the relative absorbance of the target sample (A). Based on these calibration experiments, the peanut detection limit is also found as 1 ppm, as illustrated in Fig. A-3.

A.3 Results and discussions

I evaluated the performance of this iTube platform by testing 3 different kinds of Mrs. Fields Cookies (a commercial brand), such that peanut butter chocolate (PBC), oatmeal raisin with walnut (ORW) and milk chocolate chip (MCC) cookies were tested (each repeated 3 times) for quantification of their peanut concentrations.

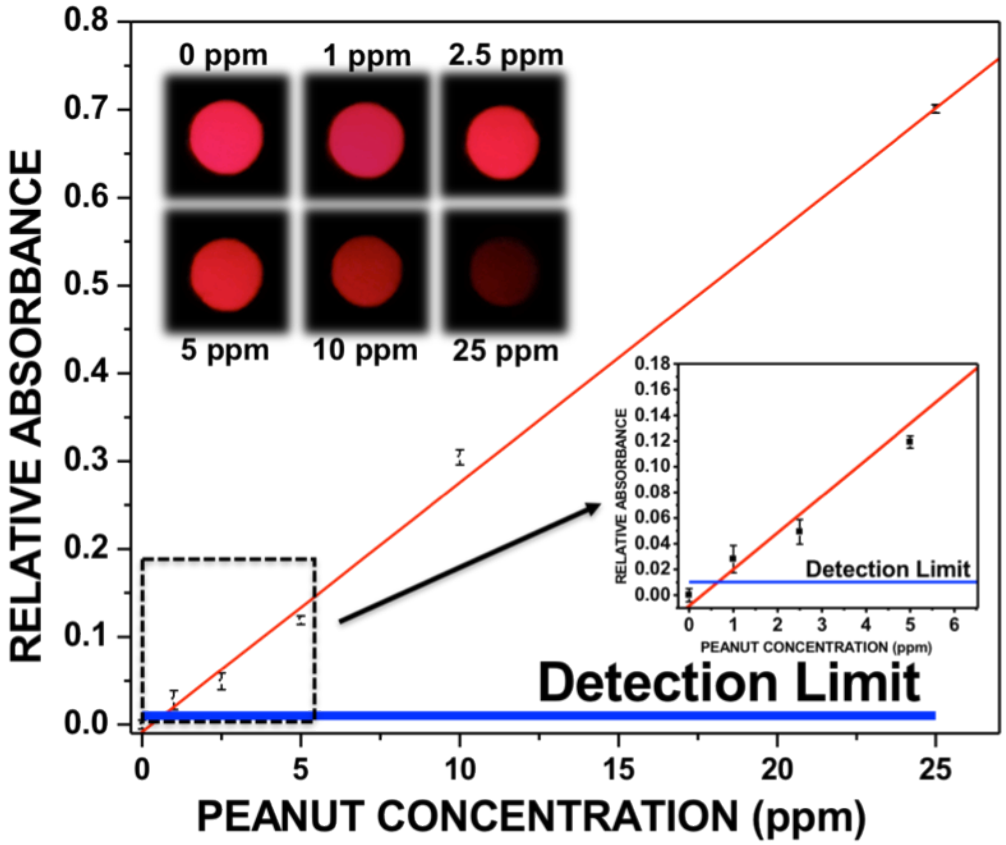

Figure A-3 | A dose–response curve for peanut allergen detection through the iTube platform is illustrated. For this curve, 6 different sets of calibration samples (0, 1, 2.5, 5, 10 and 25 ppm) were measured and converted into relative absorbance values (i.e., A). The inset shows that even very low absorbance values can be quantified, yielding 1 ppm as the minimum detectable peanut concentration, calculated by adding twice the standard deviation to the control tube signal level.

The test results (see Fig. A-4), processed through the iTube application running on the cellphone, revealed the following: (1) PBC was found positive for peanut testing and had a relative absorbance value of 0.33, corresponding to a peanut concentration of 12 ppm. I should emphasize that in these measurements I diluted the PBC extract at least 5,000 times with phosphate buffered saline (PBS) solution so that the relative absorbance value remains within the range of the calibration curve. Therefore, the actual peanut concentration within the PBC sample was in fact >60000 ppm. This large dilution factor is not necessary for practical purposes since such high concentrations of allergens are not as important as “hidden” contamination cases, and

therefore quantification of these high concentration levels is not necessarily useful for this personalized allergen testing platform. If desired, however, a set of successive measurements with varying dilution levels could be used to accurately quantify allergen concentrations that are e.g., larger than 1,000 ppm.

(2) ORW was negative for peanut testing and had negligible relative absorbance, corresponding to a peanut concentration of <1 ppm, i.e., at the level of the control tube signal. In this case, I did not get any positive signal due to walnuts present in this cookie, verifying the specificity of the test results to peanuts.

(3) MCC was also found negative for peanut testing and had negligible absorbance, corresponding to a peanut concentration of <1 ppm.

Although the presented work was performed for peanut allergen testing, the iTube platform can be employed for a variety of other allergens, including e.g., almond, egg, gluten, hazelnut, lupine, mustard, sesame, crustacean, soy, as well as milk.[19–22] The allergic individuals can choose the allergen type from the smart phone application menu (Fig. A-2d), which should be pre-programmed with different calibration factors for each allergen type of interest and its associated test kit.

Finally, as the allergic individuals use the iTube platform to perform allergen testing, the test results of various food products can be uploaded to iTube servers to create a personalized testing archive, which could provide additional resources for allergic individuals globally. Such a statistical allergy database and its spatio-temporal analysis could be especially useful for food related regulations and policies instructed in, for example, restaurants, food production lines, as well as consumer protection organizations.

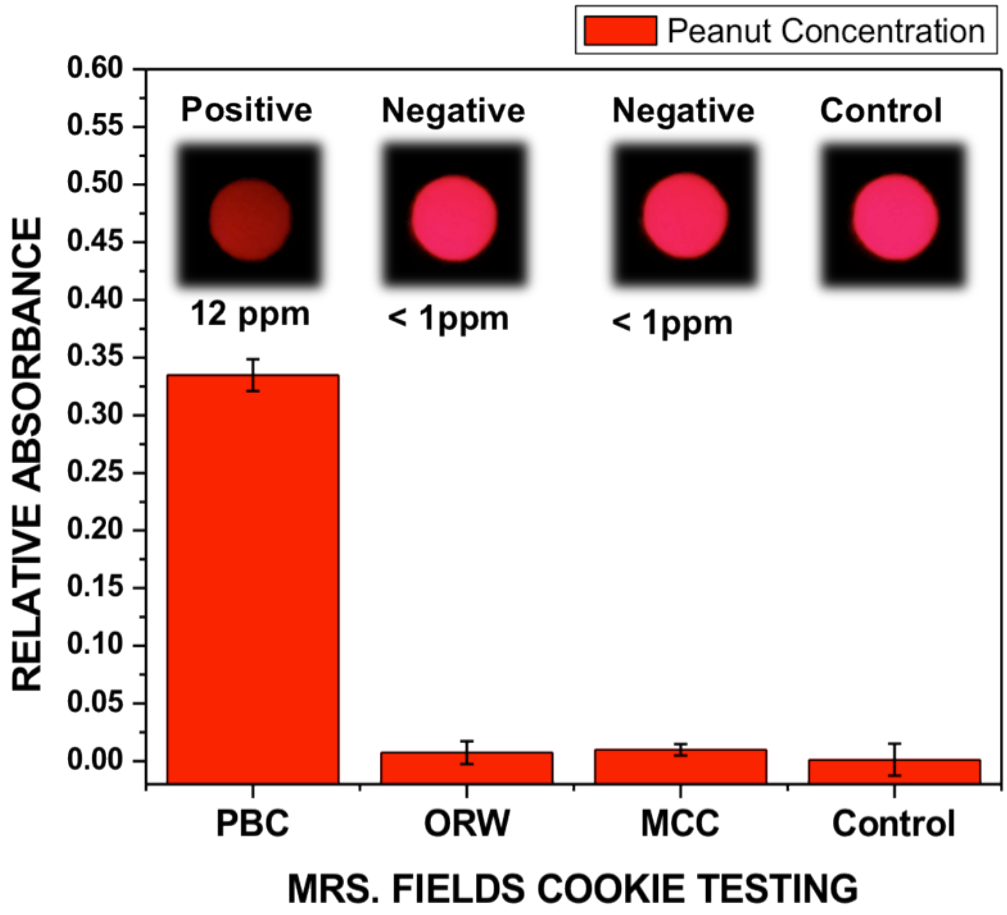

Figure A-4 | Testing of the peanut concentrations of different cookies is demonstrated through the iTube platform, where 3 sets of peanut butter chocolate (PBC), oatmeal raisin with walnut (ORW) and milk chocolate chip (MCC) cookies were measured. Note that I diluted the PBC extract at least 5,000 times with PBS solution so that the relative absorbance value remains within the range of the calibration curve. This large dilution factor is not necessary for practical purposes since such high concentrations of allergens would not be observed in "hidden" contamination cases.

I demonstrated a personalized allergen testing platform (termed iTube), utilizing colorimetric assays performed in test tubes and smart phone-based digital analysis, to specifically and sensitively detect and quantify the allergen concentration in food products. Such a cost-effective and personalized allergen testing tool, combined with an easy-to-use and rapid application running on a cellphone, could be especially useful for public health in various settings, including e.g., schools, restaurants, airplanes, as well as other public venues.

A.5 References

1. Sampson, H. A. Food allergy. Part 1: Immunopathogenesis and clinical disorders. Journal of Allergy and Clinical Immunology **103,** 717–728 (1999).
2. Sampson, H. A. 9. Food allergy. Journal of Allergy and Clinical Immunology **111,** S540–S547 (2003).
3. Besler, M. Determination of allergens in foods. TrAC Trends in Analytical Chemistry **20,** 662–672 (2001).
4. Yunginger JW, S. K. FAtal food-induced anaphylaxis. JAMA **260,** 1450–1452 (1988).
5. Wüthrich, B. Lethal or life-threatening allergic reactions to food. J Investig Allergol Clin Immunol **10,** 59–65 (2000).
6. Poms, R. E., Klein, C. L. & Anklam, E. Methods for allergen analysis in food: a review. Food Additives and Contaminants **21,** 1–31 (2004).
7. Nutrition, C. for F. S. and A. Guidance, Compliance & Regulatory Information - Food Allergen Labeling and Consumer Protection Act of 2004 (Public Law 108-282, Title II). at <http://www.fda.gov/food/labelingnutrition/FoodAllergensLabeling/GuidanceComplianceRegulatoryInformation/ucm106187.htm>
8. Besler, M., Steinhart, H. & Paschke, A. Stability of food allergens and allergenicity of processed foods. Journal of Chromatography B: Biomedical Sciences and Applications **756,** 207–228 (2001).
9. Kirsch, S. et al. Quantitative methods for food allergens: a review. Anal Bioanal Chem **395,** 57–67 (2009).
10. Taylor, S. L. & Hefle, S. L. Food allergen labeling in the USA and Europe. Current Opinion in Allergy and Clinical Immunology **6,** 186–190 (2006).

11. Stephan, O. & Vieths, S. Development of a Real-Time PCR and a Sandwich ELISA for Detection of Potentially Allergenic Trace Amounts of Peanut (Arachis hypogaea) in Processed Foods. J. Agric. Food Chem. **52,** 3754–3760 (2004).

12. Poms, R. E., Anklam, E. & Kuhn, M. Polymerase chain reaction techniques for food allergen detection. J AOAC Int **87,** 1391–1397 (2004).

13. Careri, M. et al. Determination of peanut allergens in cereal-chocolate-based snacks: metal-tag inductively coupled plasma mass spectrometry immunoassay versus liquid chromatography/electrospray ionization tandem mass spectrometry. Rapid Communications in Mass Spectrometry **22,** 807–811 (2008).

14. Yman, I. M., Eriksson, A., Johansson, M. A. & Hellenäs, K.-E. Food allergen detection with biosensor immunoassays. J AOAC Int **89,** 856–861 (2006).

15. Pollet, J. et al. Fast and accurate peanut allergen detection with nanobead enhanced optical fiber SPR biosensor. Talanta **83,** 1436–1441 (2011).

16. Shriver-Lake, L. C., Taitt, C. R. & Ligler, F. S. Applications of array biosensor for detection of food allergens. J AOAC Int **87,** 1498–1502 (2004).

17. Liu, H., Malhotra, R., Peczuh, M. W. & Rusling, J. F. Electrochemical immunosensors for antibodies to peanut allergen ara h2 using gold nanoparticle-peptide films. Anal. Chem. **82,** 5865–5871 (2010).

18. Narsaiah, K., Jha, S. N., Bhardwaj, R., Sharma, R. & Kumar, R. Optical biosensors for food quality and safety assurance—a review. J Food Sci Technol **49,** 383–406 (2012).

19. Lee, P.-W., Niemann, L. M., Lambrecht, D. M., Nordlee, J. A. & Taylor, S. L. Detection of Mustard, Egg, Milk, and Gluten in Salad Dressing Using Enzyme-Linked Immunosorbent Assays (ELISAs). Journal of Food Science **74,** T46–T50 (2009).

20. Cucu, T. et al. ELISA detection of hazelnut proteins: effect of protein glycation in the presence or absence of wheat proteins. Food Additives & Contaminants: Part A **28,** 1–10 (2011).

21. L'Hocine, L., Boye, J. I. & Munyana, C. Detection and Quantification of Soy Allergens in Food: Study of Two Commercial Enzyme-Linked Immunosorbent Assays. Journal of Food Science **72,** C145–C153 (2007).

22. Garber, E. A. E. & Perry, J. Detection of hazelnuts and almonds using commercial ELISA test kits. Anal Bioanal Chem **396,** 1939–1945 (2010).